Design and optimization of aircraft engine nozzles in under-wing configuration

Simon Bagy

THÈSE POUR OBTENIR LE GRADE DE DOCTEUR DE L'UNIVERSITE DE MONTPELLIER

En Mathématiques et Modélisation

École doctorale : Information, Structures, Systèmes

Unité de recherche ACSIOM

Design and optimization of aircraft engine nozzles in under-wing configuration

Présentée par Simon Bagy

Le 4 septembre 2020

Sous la direction de Pr. Bijan MOHAMMADI

Devant le jury composé de

M. Michel COSTES, Directeur de recherche, Office National d'Études et de Recherches Aérospatiales	Président du jury
Mme. Esther ANDRES PEREZ, Maître de conférences (équivalent), Universidad Politécnica de Madrid	Rapporteur
M. Tom VERSTRAETE, Professeur, Von Karman Institute for Fluid Dynamics	Rapporteur
M. Bruno KOOBUS, Professeur des universités, Université de Montpellier	Membre du jury
M. Michaël MEHEUT, Chargé de recherche, Office National d'Études et de Recherches Aérospatiales	Membre du jury
M. Bijan MOHAMMADI, Professeur, Université de Montpellier	Directeur de thèse

UNIVERSITÉ DE MONTPELLIER

Acknowledgements / Remerciements

Les travaux effectués au cours de ces trois ans n'ont pas reposé sur mes seules épaules. Je souhaite tout d'abord remercier Mathieu Lallia, sans qui ce projet de thèse n'aurait pas existé. Ses connaissances de l'aérodynamique des nacelles m'ont aidé à m'y retrouver quand j'ai eu des doutes, et il aura toujours été là pour répondre simplement à mes questions. Un grand merci à mon directeur de thèse Bijan Mohammadi, qui m'a proposé l'idée alternative de la combinaison convexe, afin de répondre au mieux aux attentes d'un sujet ambitieux. Je remercie également Michaël Méheut, qui m'a accueilli à l'ONERA pendant plus de deux ans, et qui m'a accompagné dans mes premières optimisations de formes aérodynamiques. J'adresse un grand merci à Pascal Coat, grâce à qui j'ai mieux compris les aspects thermodynamiques des moteurs aéronautiques, et qui aura relevé avec nous le défi de concilier un modèle de moteur avec nos calculs aérodynamiques. Merci aussi à Frédéric, qui se cache derrière le modèle. Je salue le courage de Jean, qui a développé et assuré le fonctionnement du modèle CAO et du maillage de la nacelle, et qui a su garder patience jusqu'au bout de ce projet malgré mes sollicitations incessantes : merci ! Je remercie Christian et Nicolas, qui m'ont épaulé en tant que responsables et qui ont toujours su m'écouter et m'aiguiller, même dans les moments difficiles.

Je trouve qu'il n'est pas toujours aisé d'arriver dans un nouvel environnement, et c'est pourquoi je tiens à remercier mes collègues de bureau chez Safran et à l'ONERA, pour m'avoir accueilli puis accompagné dans cette aventure. En particulier, merci à Romeo, Sophie, Guillaume, Alexandre, Jackie, Philippe, Jagoda, Lauren ainsi que le reste de l'équipe YSRK / YXAK, qui m'a prise en charge avant le commencement de cette thèse. Je retiendrai de ces quatre années parmi vous la bonne humeur qui règne dans l'équipe ! Un grand merci à Ilias et Edoardo, qui m'ont ouvert la porte de leur bureau lors de mon arrivée en laboratoire, mais également à Fulvio que j'ai harcelé de questions, à Christelle pour la course à pied, à Michel pour son humilité sans faille. Merci infiniment à Antoine, qui m'aura initié à la théorie des calculs adjoints, et qui s'est avéré devenir le plus sympathique des covoitureurs. J'adresse également mes remerciements aux doctorants et stagiaires (Frédéric, Camille, Hadrian, Stelios et les autres...) ainsi qu'à mes collègues de laboratoire (notamment dans les unités ACI et H2T) pour m'avoir supporté quand je râlais à la pause café. C'est en échangeant avec vous que cette expérience a été si enrichissante, scientifiquement et personnellement.

Pour finir, je souhaite remercier mes amis, et en particulier les membres du Club Kiwi, qui m'ont apporté leur soutien et permis de décompresser au cours de ces trois années. Merci à ma famille, à mes parents et à Coraline, qui m'ont toujours encouragé. Enfin, mille mercis à Julie, qui a été à mes côtés tout au long du chemin, et avec qui je partage tant.

Contents

List of frequently used acronyms

Boundary Layer Ingestion	BLI
ByPass Ratio	BPR
Computer-Aided Design	CAD
Computational Fluid Dynamics	CFD
Design Of Experiments	DOE
Integrated Power Plant System	IPPS
Nozzle Pressure Ratio	NPR
Reynolds-Averaged Navier-Stokes	RANS
Specific Fuel Consumption	SFC
Surrogate-Based Optimization	SBO
Ultra High Bypass Ratio	UHBR

I

Introduction

Today more than ever, aircraft and engine manufacturers are making efforts in order to reduce the environmental footprint of air transport. One of the main design objectives is to achieve new aircraft configurations allowing a reduction of the flight mission fuel burn. Concerning aircraft engines, one of the technological solutions to improve turbofan efficiency is to tend towards greater *ByPass Ratio* (BPR). In practice, this is done by increasing the mass flow rate of the secondary flow (or bypass flow) with respect to the primary flow passing through the engine core. As a consequence, the diameter of recent engine nacelles is generally greater than on previous turbofan generations. Due to under-wing integration constraints, the space between the nacelle and the lower surface of the wing becomes narrower. This results in stronger aerodynamic interactions between these components. These installation effects alter the aerodynamics of both the engine and the wing, and may have significant consequences on overall aircraft performance.

In particular, the engine nozzles are located in the immediate vicinity of the wing and are directly impacted by the aforementioned installation effects. Yet, these components have a major role in engine performance and operability. Consequently, it is necessary to assess and take precisely into account aerodynamic wing-engine interactions in early nozzle design phases.

In this situation, shape optimization approaches are expected to provide a good way to assist research and development engineers in the design of such engine components. Such methods have proven their efficiency on cases of growing complexity in the past decades.

In 2017, Stankowski et al. [75] evaluated the influence of the position and the size of separate-flow engines on the aircraft fuel consumption on a full mission. This study, based on *Reynolds-Averaged Navier-Stokes* (RANS) computations coupled with an engine model, determines an optimal engine position with a *Design Of Experiments* (DOE). Finally, it shows that the wing-engine interference effects have a significant im-

pact on aircraft fuel burn estimate for a full mission. Still, this work does not modify the nacelle design, or integrate optimization methods.

Goulos et al. [25] performed optimizations of separate-jet exhaust designs, based on complex axi-symmetrical geometries. This work applies DOE methods, surrogate modeling and genetic algorithms to optimize nozzle performance. It achieves an improvement of the propulsive force for two types of configurations, corresponding to former and future engine designs. However, this work does not take into account the aerodynamic installation effects and the influence of the wing on engine performance.

Then, in 2018, Gray et al. [29] implemented a fully-coupled aeropropulsive design optimization. Their work aims at optimizing the performance of the so-called STARC-ABL aircraft configuration with electric *Boundary-Layer Ingestion* (BLI) propulsion system. Gradient-based optimizations are performed with an adjoint workflow, comprising a thermodynamical model of the engine. This demonstrates the benefit of coupling aerodynamic computations with a thermodynamical engine model for nacelle design purpose. Yet, due to its application on an aft-mounted BLI engine, this study does not address the aerodynamic interactions related to under-wing engines and their installation.

To sum up, these recent studies highlight the significant effects of under-wing installation and engine positioning on aircraft mission fuel burn. Moreover, they present optimizations of complex separate-exhaust nozzle performed with *Computational Fluid Dynamics* (CFD). Finally, they show that coupling a thermodynamical model of the engine with aerodynamic computations is of great interest for design phases and optimization. However, there is no optimization study concerning separate-exhaust nozzle installed under the wing and using aero-propulsive coupling to improve the performance of the engine. In addition, industrial design requires know-how-based parameterizations and commercial software, that are not accounted for in the aforementioned studies.

This justifies the present thesis work, that consists in developing aerodynamic shape optimizations of turbofan engine nozzles in under-wing configuration, including industrial design tools and coupled aeropropulsive computations.

In order to implement this type of optimizations, several major objectives must be addressed sequentially:

- Identifying and developing optimization methods and strategies adapted to industrial aerodynamic design applications, with non-differentiated "black-box" tools, e.g. *Computer-Aided Design* (CAD) software, and a high number of variables
- Assessing the chosen approach on a nozzle case of reduced complexity.
- Developing a detailed geometrical model of turbofan nacelle, that enables large modifications for optimization and respects design constraints
- Coupling aerodynamic simulations with a thermodynamic engine model, to achieve

coupled aeropropulsive simulations, and integrate them to the optimization workflow

- Applying optimization to improve the nozzles of an isolated turbofan.
- Applying optimization to an under-wing engine configuration

Each of these objectives has been considered in the scope of the present thesis work. However, due to their challenging nature and the time required for their implementation, all could not be addressed. In this manuscript, all steps but the last are discussed and the remaining is presented as a perspective of this work.

To begin with, the context of turbofan nozzles design is introduced in Chapter II. The role of the nozzles and their working principles are detailed, as well as the associated industrial design methodology.

Then, it appears that the current study is related to several subjects that have been treated in the literature. Therefore, a state of the art review on these topics is done in Chapter III.

The approach of this work consists first in elaborating an optimization strategy adapted to the challenges (Chapter IV). A review of optimization methods is proposed and their way of exploring the targeted design space is discussed. Their capability of dealing with a high number of design variables as well as an industrial workflow comprising "black box" tools is assessed. Then, an innovating approach called *convex combination* is proposed, in order to introduce CAD-generated geometries in the workflow and reduce the dimension of the optimization problem while considering all CAD parameters. The method is applied on a simple and preliminary analytic case. Next, some design strategies based on this approach are suggested for industrial applications.

The second step of this work is the application of the chosen approach to a nozzle case (Chapter V). A two-dimensional single-flow nozzle test case is developed and an associated optimization problem is defined. In order to enable simple comparison, a theoretical isentropic one-dimensional computation of nozzle flow is presented. Then, the optimization workflow is tested on a first optimization case, using feasible descent on the full design space and considering inviscid flow simulations. Next, the convex combination method is evaluated on the same case, the results are compared and validated against theory. Thanks to the dimensionality reduction offered by the proposed approach, designs of experiments become feasible and are launched on the inviscid optimization problem. Then, flow viscosity is introduced into the optimization problem, and the same steps are repeated to assess the approach on a different case. To conclude, the optimization problem considered is discussed a posteriori, with its limitations and ways of improvement.

Then, the development of a design workflow comprising industrial CAD and meshing tools is presented in Chapter VI. A CAD model of a detailed turbofan engine nacelle is presented, as well as the associated mesh generation for flow computations. The automation of the process for geometry and mesh generation is described and explained.

Next, optimizations are performed on dual-separate flow nozzles for an isolated nacelle configuration in Chapter VII. A workflow comprising the industrial CAD and mesh tools is implemented and an adapted optimization problem is defined. The robustness of the complete workflow is discussed and improved. Then, an optimization is launched using the convex combination approach. The optimal configuration is presented with a detailed breakdown of surface force contributions and a physical interpretation of its performance. Based on the interpretation of the first optimal combination, a second optimization is launched. In parallel, a DOE is performed to have an improved understanding of the design space.

The last step of this study aims at implementing coupled aero-propulsive simulations for nozzle design (Chapter VIII). The dependencies between engine thermodynamics and nacelle aerodynamics are explained. Then, strategies of coupling are discussed and assessed on a first case. Eventually, the coupling process is applied on an optimal nozzle shape, and highlights the interest of aeropropulsive coupling for engine performance prediction and optimization.

Finally, the conclusions of this work are exposed. Several perspectives for future developments and applications are presented.

The research of an adapted optimization strategy led to the assessment of adjoint methods and their feasibility. Thus, the detailed establishment of an adjoint-based optimization problem is presented in Appendix A of this document.

Moreover, a list of publications and communications related to this work is proposed in Appendix B and a short summary of the thesis work can be found in Appendix C.

II

Working principles and design of turbofan nozzles

Contents

II.1 Aircraft engine technologies

Along with the development of air transport, aircraft propulsion systems have evolved over the years. Nowadays, several technical solutions are used to provide thrust for passenger aircraft.

A first type of propulsion systems is *turboprop* engines. These engines are based on a turbine powering a propeller, which accelerates air and creates thrust. Turboprop engines have a very good fuel efficiency, which reduces as the flight speed and altitude of the aircraft increase. Moreover, propellers are only suitable for subsonic flight speeds. Consequently, turboprop engines are used for regional aircraft (see Fig. II.1(a)) or cargo planes with short flight range. Such aircraft are less impacted by the speed limitation and take advantage of the low fuel-burn.

Long flight range airliners tend to use a different propulsion technology, the *turbofan* engine architecture. Due to its interesting fuel-efficiency at high speeds and altitudes, this type of engines has become the most common propulsion system for long-range business jets and passenger aircraft. In this work, only the latter type of aircraft

propulsion system is considered. It is presented in detail and its working principle is explained in the following sections.

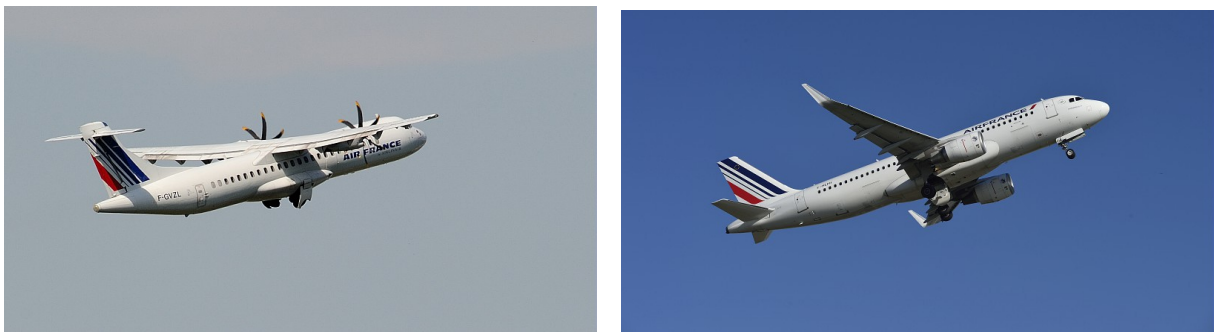

(a) ATR-72 ©Daniel Linares / Safran (b) Airbus A320 ©Alain Ernoult / Safran

Figure II.1 – *View of aircraft with turboprop (a) and turbofan (b) engines*

II.2 Working principle of turbofan engine

The turbofan engine technology is born as an upgrade of a previous propulsion system, the turbojet engine. Consequently, the working principle of this type of engines is presented to introduce turbofan architecture. The turbojet technology, developed during World War II, represents a breakthrough compared to previous pistons engines. Its fundamental principle is to create thrust by accelerating a working fluid (in this case, air). The incoming air flow at ambient pressure is compressed through a first series of rotating stages in the compressor (as represented on Fig. II.2). Then, fuel is injected in the pressurized air flow and the resulting air-fuel mix is ignited in the combustion chamber. The combustion generates a large amount of heat and pressure and the highly energetic flow of exhaust gas is expanded in a turbine. The energy collected in the turbine stages is transmitted via an axial shaft and powers the rotating compressor located upstream. Downstream the turbine, the exhaust gas are expanded and accelerated in the nozzle and released outside of the engine at ambient pressure.

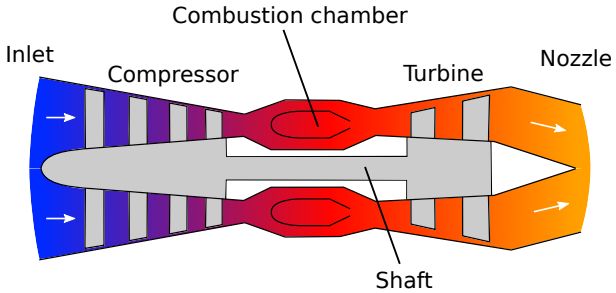

Figure II.2 – *Schematic view of a turbojet engine*

The principle of turbofan engine is to add a ducted fan to the turbojet architecture (see Fig.II.3). This fan, often associated to a second shaft and powered by a new series of turbine rows, is located upstream of the compressor stages of the engine. After the fan, the mass flow is split and distributed in two separate ducts. The first part, called "core" or "primary" flow of the engine, goes into the compressor stages and is used to

power the turbine. The remaining part of the air flowing through the engine is directed in a "secondary" or "bypass" flow and expanded in a nozzle after the fan stage.

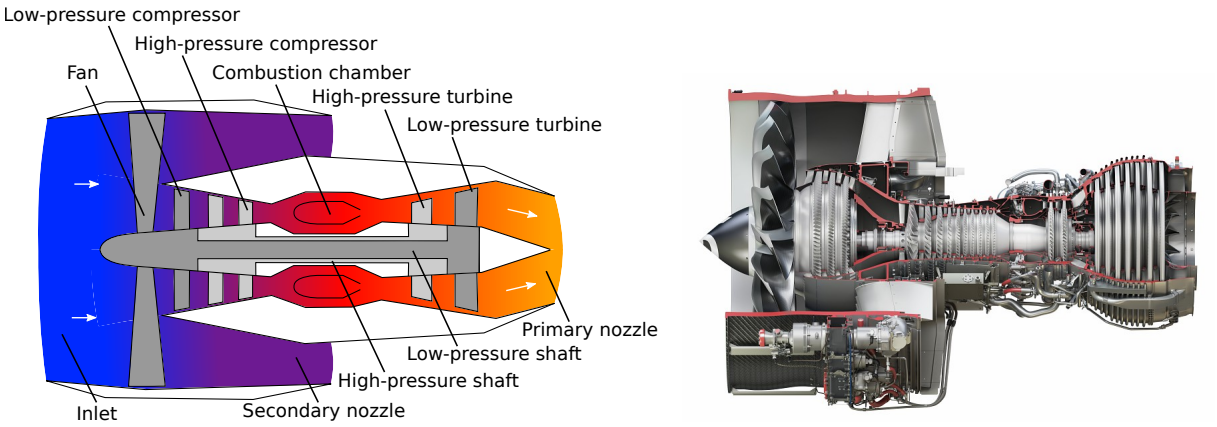

(a)

(b) LEAP-1A turbofan engine ©Antonio Gomez / Safran

Figure II.3 – *Schematic view (a) and industrial configuration (b) of a turbofan engine*

The *bypass ratio* of the turbofan is defined as the ratio of the mass flow rate $\dot{m}$ in the bypass flow with respect to the mass flow rate in the core:

$$BPR = \frac{\dot{m}_{sec}}{\dot{m}_{prim}} \tag{II.1}$$

For passenger aircraft, the value of the BPR can go from around 6 (on CFM56 engines for instance) to 11 for current configurations (e.g. LEAP engines) and up to 16 for future *Ultra-High BPR* (UHBR) turbofans (entry into service 2025 - 2035). Consequently, only a minor part of the incoming air flows into the engine, while the major part is directed in the secondary duct. In this situation, the secondary flow is responsible for the main part of the engine propulsive force (usually around 90% for a BPR of 10). Moreover, increasing the BPR has the advantage of improving the thermal and propulsive efficiencies of the engine. Therefore, high BPR turbofan engines have a reduced *Specific Fuel Consumption* (SFC) and a greater overall fuel efficiency. This tendency is valid up to the point where the increase in mass and friction forces compensate the beneficial effect of higher BPR on engine SFC.

II.3 Nozzles

II.3.1 Position and roles

Turbofan engines have two nozzles, located on the rear-body of the engine and associated to the core and the secondary flows of the engine. The core nozzle is located after the last turbine stage, while the secondary nozzle begins after the guide vanes in the fan flow. Their location on a fully *Integrated Power Plant System* (IPPS) is represented on Fig. II.4. As a consequence, nozzle design considers internal ducts as well as other rear-body elements, such as the external cowls, the pylon and the plug.

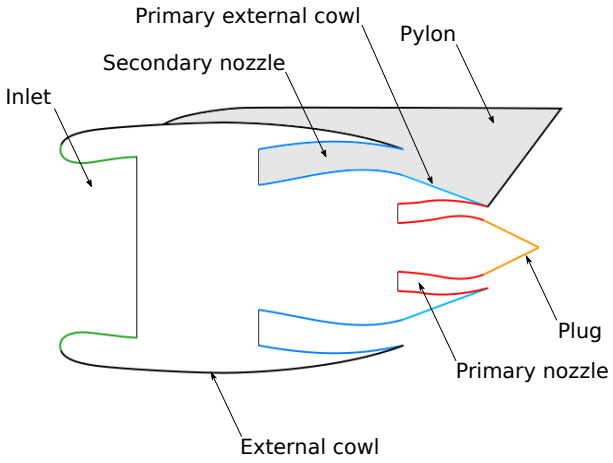

Figure II.4 – *Schematic view of an integrated powerplant system*

The nozzles have two main functions. The first one is related to engine performance. In both core and fan flows of the engine, the pressure of the exhaust gas entering the nozzle is higher than the ambient pressure. Consequently, the gas is expanded and accelerated through the nozzles. The exhaust of the mass flow at high velocity and the pressure force on nozzle cowls generate the thrust force produced by the propulsion system. Consequently, the propulsive force directly depends on rear-body and nozzle design.
The second role of the nozzles is linked to operability, because they set the mass flow rate in the engine, in all flight phases. For instance, on the ground and in take-off conditions, the nozzle flows are subsonic, no shock appears, and the mass flow depends on the exhaust area and the design of the nozzle ducts. In particular, their design has an impact on compressor operating point and thus on compressor stall margin. In conclusion, these two functions indicate that nozzle design has a significant influence on the performance and the behavior of the engine, in all operating conditions.

II.3.2 Types of nozzle geometries

On turbofan engines, two types of nozzle geometries exist. The first type comprises two separate annular exhausts, one for each flow of the engine (as depicted in Fig. II.5(a) and II.5(c)). Separate exhausts are the simplest technological choice. However, from an acoustic point of view, the noise of jet flows is highly related to their temperature. On separate-flow nozzles, the hot jet from the core flow represents consequently a source of noise.

The second possibility is to mix the core flow and the secondary flow of the engine upstream of a common exhaust (see the examples on Fig. II.5(b) and II.5(d)). In this case, an additional element appears in the nozzle, the "mixer". This part is designed to maximize the mixing of the two engine flows before the exhaust. As a consequence, mixed-flow nozzles have lower exhaust gas temperatures. This implies a reduction of the acoustic noise produced by the exhaust jet. In addition, it improves the fuel efficiency of the engine. Both of these reasons motivate their use on many business-jet aircraft and some airliners. However, this technology comes at the cost of an increased

IPPS weight, due to longer nozzle cowls and the addition of the mixer. Moreover, mixed-flow nozzles have complex designs, in particular due to the mixer, and can result in increased friction forces.

The trade-off between these two types of nozzles depends on the aircraft and the choices of engine designers. For turbofan engines with high BPR, the benefits of mixed-flow nozzles are compensated by their greater mass.
The study presented here focuses on turbofan engines with separate-flow nozzles.

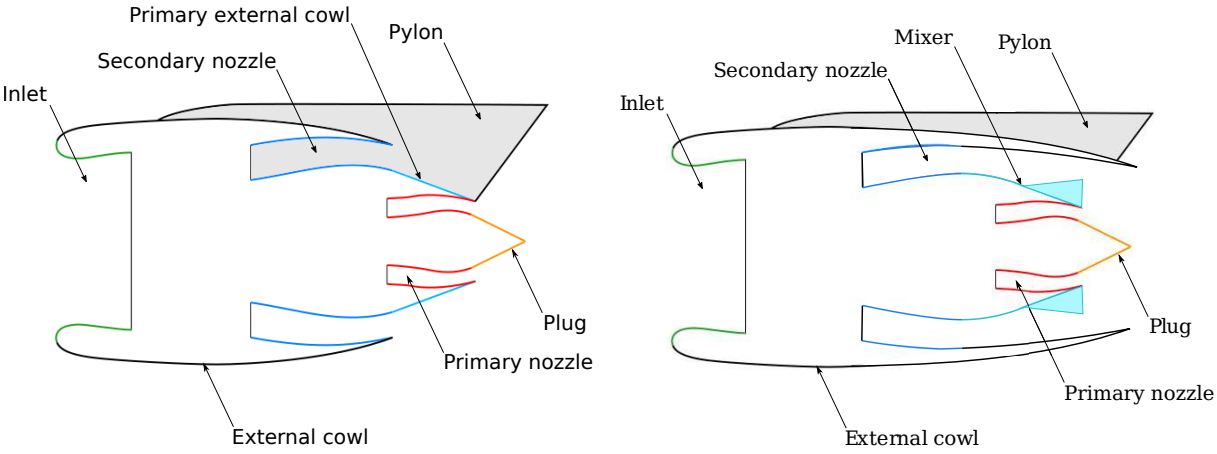

(c) CFM56-5B ©Charles Pertwee / CAPA Pictures / Safran

(d) SaM146 ©Raphael Olivier / CAPA Pictures / Safran

Figure II.5 – *Schematic views and pictures of separate (a,c) and mixed (b,d) -flow nozzles of turbofan engines*

II.3.3 Fundamental physics of nozzle flows

The principles of a nozzle flow can be approximated by simple physics, as explained in Candel [11]. An axisymmetric convergent-divergent nozzle geometry is considered. The flow is supposed adiabatic and friction is neglected. A subsonic gas flow is injected in the nozzle, at a given stagnation pressure $p_{i\,injection}$. In this case, for a fixed nozzle geometry, several flow regimes can be observed depending on $p_{i\,injection}$. Nozzle

designers usually refer to the *Nozzle Pressure Ratio* (NPR) defined as:

$$NPR = \frac{p_{i\,injection}}{p_{amb}} \tag{II.2}$$

with p_{amb} the ambient pressure outside of the nozzle.

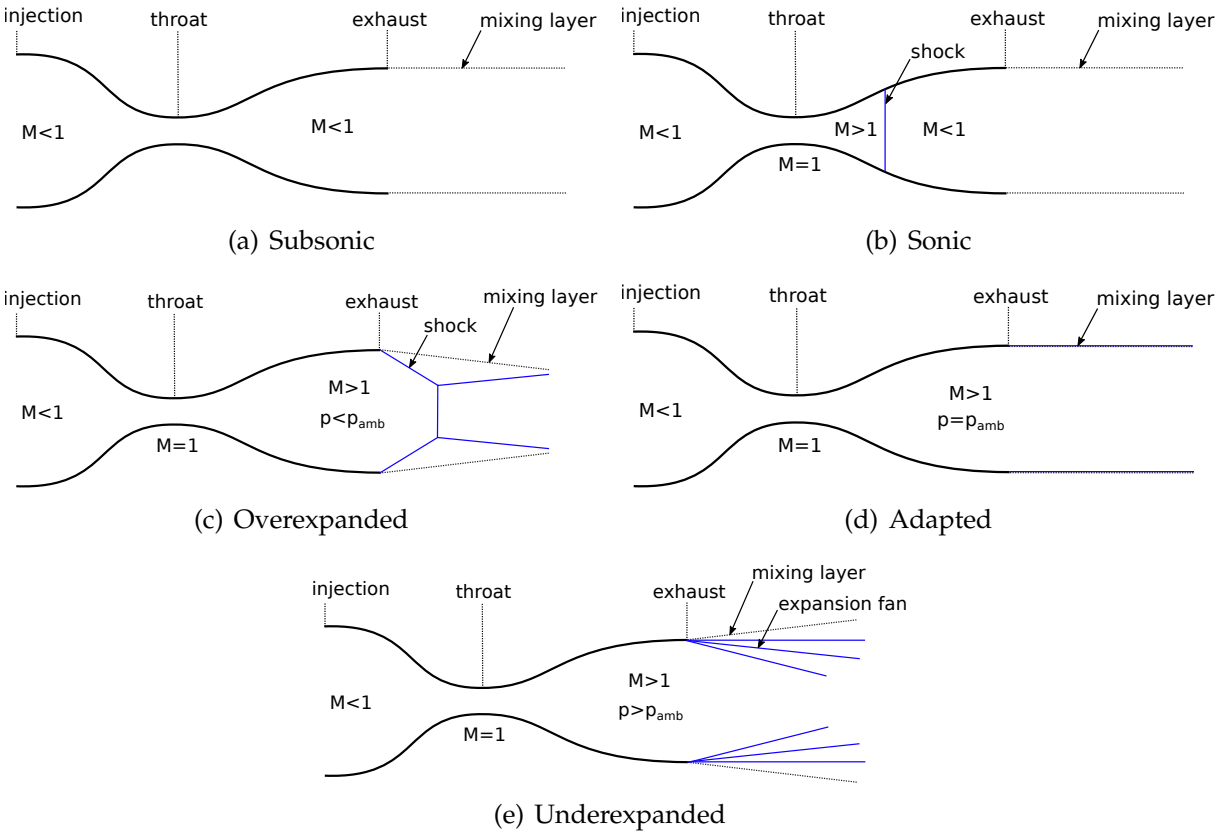

Figure II.6 – *Schematic view of flow regimes in a convergent-divergent nozzle (adapted from [11])*

When the stagnation pressure in the injection plane is low, the flow remains subsonic along the nozzle (see Fig II.6(a)). Consequently, the fluid accelerates up to the throat and decelerates in the divergent.

If the NPR is increased, the flow becomes sonic at the throat, meaning $M_{throat} = 1$. Then, the shock will move downstream in the divergent as the NPR increases, until it reaches the exhaust section. At this point, the flow is supersonic all along the divergent.

For higher NPR values, an "overexpanded" flow regime can be observed. The flow acceleration in the nozzle is such that the exhaust pressure is lower than the ambient pressure. Consequently, oblique shock waves appear and shock cells are generated in the flow downstream the nozzle (as schematized on Fig. II.6(c)).

If the NPR is further increased until a specific value, a particular nozzle flow can be observed. This "adapted" regime corresponds to the case where $p_{exhaust} = p_{amb}$. In this configuration, shock cells disappear and the mixing layer is similar to the subsonic mixing layer (Fig. II.6(d)). For nozzle designers, this operating point corresponds to the best efficiency case except for subsonic regimes.

Finally, when the NPR is set at higher values, an "underexpanded" flow regime appears. In this case, the pressure level in the nozzle is very high and $p_{exhaust} > p_{amb}$. The flow expands to return to ambient pressure, and expansion waves appear at the exhaust (depicted in Fig. II.6(e)).

Although the description of the flow regimes has been made on a convergent-divergent nozzle geometry, it can be extended to convergent nozzles. A convergent geometry can be considered as a particular case of the convergent-divergent geometry, with coincident throat and exhaust planes. In this case, the onset of a sonic flow regime at the throat correspond to the adapted flow regime, and is directly followed by the underexpanded regime when the NPR increases.

II.4 Aerodynamic design workflow and tools

In industrial design office, the development of aerodynamic systems such as engine rear-body shapes and nozzles relies on both experimental and numerical studies. Thanks to increasing computational capacity, numerics are now used as a design tool with an overnight return time. Then, numerical simulations are validated against experimental testing in wind tunnels and test benches, that are more costly.

Concerning aerodynamic design based on CFD, industrial methodologies usually follow a common "backbone" as explained in [36]. Fig. II.7 gives an example of an industrial numerical design process, from geometry generation to post-processing, and presents the associated tools used at Safran Aircraft Engines.

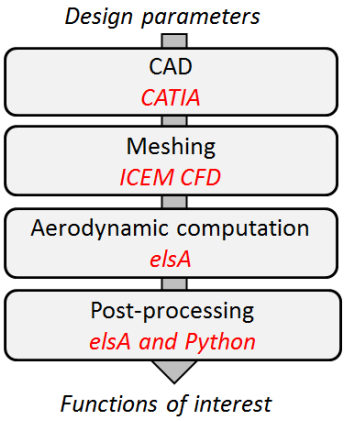

Figure II.7 – *Overview of the main steps of an aerodynamic design process and examples of associated tools*

First, the geometry of the studied aerodynamical elements is generated. This can be achieved with analytical functions and models. However, these methods are limited for the design of industrial components with complex shapes and comprising numerous elements. Thus, *Computer-Aided Design* software is used to draw tridimensional complex components and has become an essential part of industrial design processes. Moreover, these tools enable the creation of parameterized geometrical models. Designers often use CAD models with dedicated sets of design parameters, based on

expert knowledge and industrial know-how. For three-dimensional geometries of industrial complexity, several hundreds of design variables can be required for the full parameterization of the CAD model.

Then, the fluidic domain associated to the geometry is defined, and a grid is generated for CFD. Even though the generation of fluid domain meshes can be done analytically, it is often done with dedicated software. This software and designer know-how enable to generate meshes for most industrial configurations.

The next step of the process is the flow solver and the CFD simulation. These tools enable to solve the equations of motion in the fluid, and simulate the aerodynamic flow in the computational domain. A lot of methods and solvers have been developed and are available for flow computation. They range from potential methods, with low computational cost but based on strong hypothesis that limit their application to industrial cases, to *Direct Numerical Simulation* (DNS), that solve the Navier-Stokes equations without any model but are out of scope for industrial cases due to their gigantic computational cost. For industrial studies, the trade-off between simulation cost and reliability often leads to the choice of *Reynolds-Averaged Navier-Stokes* equations. Solving these equations enables the computation of viscous steady flows with turbulence models.

After convergence of the computation, the flow quantities are obtained on each point of the fluid domain mesh. In order to compute the quantities of interest for the designer, a post-processing method must be defined. Several tools and methods can be used, depending on the computed quantities. In industrial workflows, the post-processing is mostly based on "in-house" developments and methods.

To conclude, it is interesting to consider the precision required for aerodynamic design processes. This quantity drives the grid refinement, the convergence of the CFD simulations, as well as the optimization expectations. Based on technical background, a relative variation on the order of 0.1% on aircraft drag or engine propulsive force can have significant and critical consequences on the overall performance. Consequently, design modifications are likely to improve the functions of interest by 0 to 2%. The same expectation applies for aerodynamic shape optimizations on nozzle shapes, as presented in this study.

III

State of the art

Contents

This chapter proposes a brief literature review, on subjects related to nacelle design and aerodynamic shape optimization. First, installation of the engine under the aircraft wing is discussed, as well as the resulting aerodynamics interactions and their effects on aircraft performance. Then, some aerodynamic shape optimization work applied on nacelle and nozzles design are presented. Finally, the coupling of thermodynamic models with aerodynamic computations to achieve aero-propulsive simulations is considered.

III.1 Review of aerodynamic wing-engine interference effects

In common large passenger aircraft configurations, engines are located under the wings, in the vicinity of the pressure side. This location implies aerodynamic interactions between these two components. Moreover, the trend to increase BPR for engine efficiency improvement leads to greater engine diameter. As a consequence, the space between these components tends to narrow and the interactions are expected to become stronger. This phenomenon can have major effects on the global performance of the aircraft and drives engine integration, that is why this subject has been previously treated in the literature.

Interference effects due to the presence of the nacelle in the vicinity of the wing have been discussed since the 80's [16, 32]. Both numerical [67, 42, 76] and experimental studies [44, 66] have shown that interactions appear with under-wing engine installation. For instance, the nacelle modifies the flow not only on the pressure side but also on the suction side of the wing, as depicted in Fig. III.1. These effects lead to a lift decrease at constant angle of attack and drag increase at constant lift, compared to wing-body configurations.

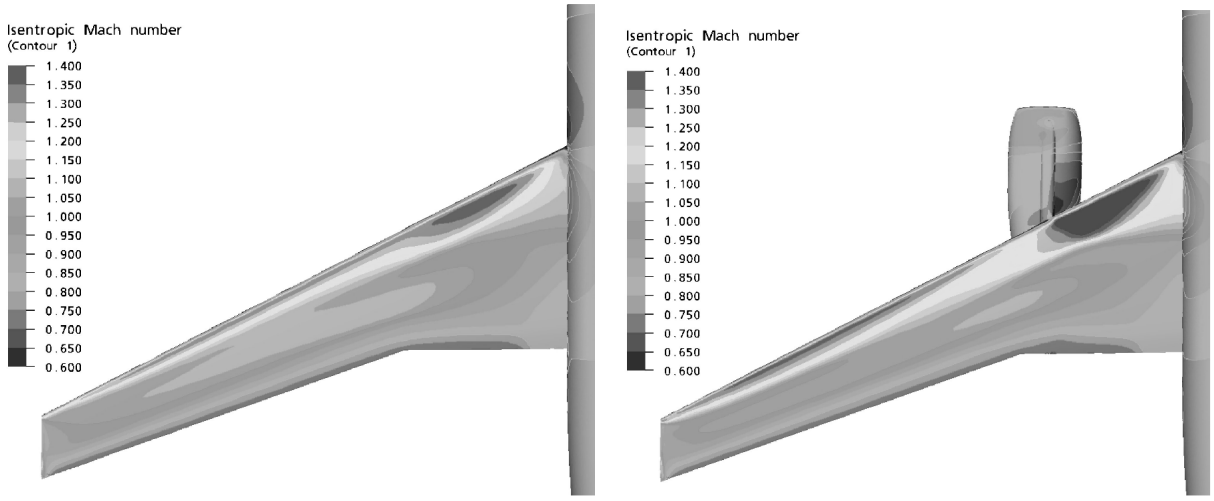

(a) Wing-body (b) Wing-body with nacelle and pylon

Figure III.1 – *Contours of isentropic Mach number predicted by simulations, from Langtry et al. [42]*

Consequently, studies have been carried out to reduce the negative integration effects by several methods. Some only focused on finding the optimal position of the nacelle with respect to the wing, by using design of experiments [75] or optimization approaches [21, 79]. Eventually, research work applied optimization techniques to aircraft configurations with wing-mounted engines [15, 38, 39, 54, 70, 73]. These studies modify the shape of the wing, the nacelle and/or the pylon to find optimal performance, while taking aerodynamic interactions into account.

However, despite identifying wing-engine aerodynamic interference effects and estimating their impact on wing or aircraft drag and efficiency, few studies have considered their effect on engine performance.

III.2 Investigation of aerodynamic shape optimizations applied to engine nacelles

Aerodynamic shape optimizations have been extensively dedicated to airfoil and wing design [43, 56, 57, 58, 48]. Still, other applications of these methods can be found in the literature, and several studies have applied these methods to engine nacelles (including inlet, external cowls and nozzles).

Some of them [45, 6, 90, 91] developed and used inverse techniques. This approach

consists in specifying a target pressure distribution on the nacelle surface, based on expert knowledge. Then, the optimization algorithm aims at finding the geometry and the flow field associated to this distribution. Inverse methods have been applied on tridimensional shapes and on engine nacelles mounted under complex aircraft configurations [90, 91]. For instance, Fig. III.2 shows the capability of the method to retrieve a specific under-wing nacelle design from a generic starting shape. When applied on wing-engine configurations, inverse methods enable a reduction of several drag counts for the overall aircraft configuration, as presented by Wilhelm [91]. However, inverse aerodynamic shape optimizations have the disadvantage of requiring an *a priori* knowledge of the desired pressure distribution.

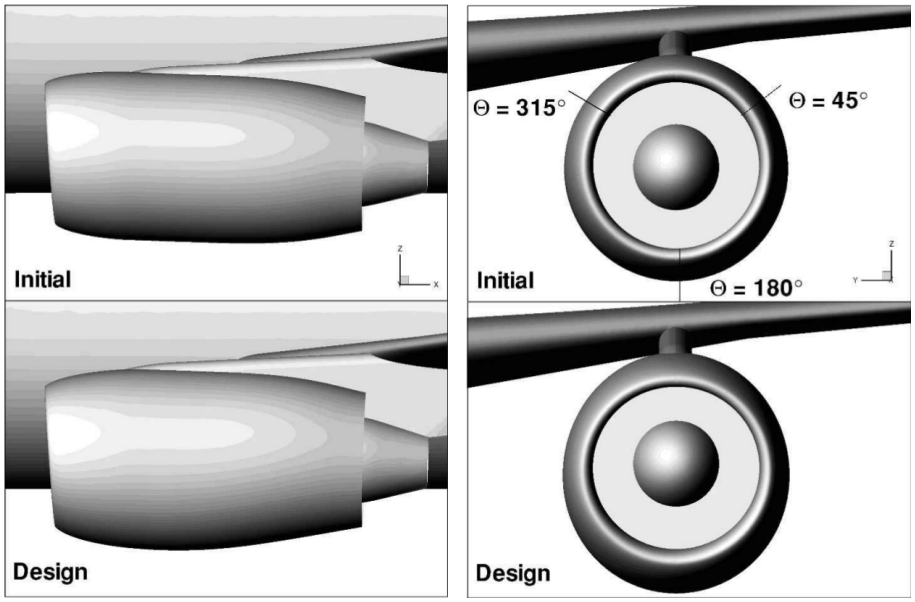

(a) Side view (b) Front view

Figure III.2 – *View of initial and redesigned shapes of an installed nacelle, from Wilhelm [90]*

A review of aerodynamic shape optimization work applied to nacelles shows that the other possible approach to tackle this problem is to perform "direct" optimizations. In this case, the goal of the algorithm is to find a shape that maximizes the performance assessed with post-treated simulations. A part of the studies allows a modification of the whole nacelle shape and define drag as the function to minimize [41, 40, 82, 81]. Then, among research work applied to engine nacelles, some focus on inlet shape design. When considering a two-dimensional geometry, the peak Mach numbers in the inlet are minimized [2]. With three-dimensional shapes, the impact of the droop and scarf angles (driving the orientation of the intake plane and its non-axisymmetrical character) on inlet performance can be assessed and optimized [74, 80].
Concerning engine rear-body, only a few studies have applied aerodynamic shape optimization methods to improve the performance of civil-aircraft turbofan nozzles. Goulos et al. presented an optimization workflow [27] and performed successful optimizations on a complete two-dimensional geometry of high-BPR engine nozzles [24, 25].
In [25], surrogate-based optimizations are applied to improve the net propulsive force of the engine. The design parameters considered enable the modification of the complete rear-body including the nozzles, the cowls and the plug. An overview of the ini-

tial and optimized geometries is depicted in Fig. III.3, which shows that the intensity of the shock outside the secondary nozzle is reduced on the optimal shape. Significant improvements of the engine propulsive performance are achieved in this work, thereby confirming the interest of using optimization methods for nozzle design.
Additional studies have been performed by this author, that focus on specific features of the rear-body engine. In [26], optimizations are performed that only consider the design of the secondary nozzle after-body and beneficial effects of an after-body curvature are observed on the overall engine performance. Then, a recent work [23] introduces total pressure profiles in the flow entering the nozzle, therefore simulating the effect of fan blade loading on nozzle optimizations.

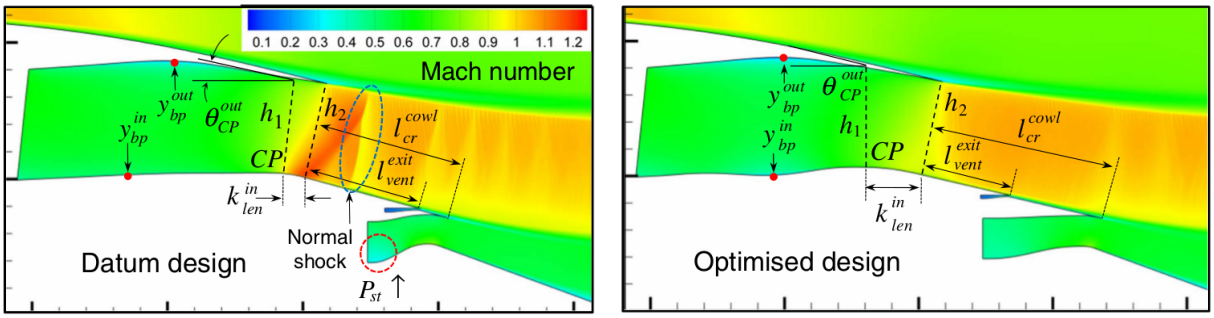

(a) (b)

Figure III.3 – *Mach field comparison between initial (a) and final (b) exhaust system designs, from Goulos et al. [25]*

To sum up, this literature review shows that some work have already applied aerodynamic shape optimizations methods for the design of engine nacelles. In general, it appears that small modifications of the nacelle geometry can have a critical impact on overall engine performance. Still, there are only a few directly applied to nozzles, and none of them takes into account the aerodynamic interactions occurring on under-wing configurations.

III.3 Review of aerodynamic shape optimizations including engine model

Nacelle and nozzle aerodynamics are tightly linked with the thermodynamic propulsive cycle of the engine. In practice, both depend on each other and the operating point can only be determined through an iterative process.

Recent studies have integrated thermodynamical models of the engine in association with aerodynamic simulations. For instance, an engine model is used in [75] to compare the performance of standard and UHBR configurations and evaluate the effect of the engine position on mission fuel burn. Other studies have implemented a coupling of the thermodynamic model and the aerodynamic simulations, i.e. *coupled aero-propulsive simulations*. Such coupling has been used for supersonic [31] and BLI engine configurations [28, 30, 29].

In particular, Gray et al. [29] used adjoint-based optimizations with coupled aero-propulsive simulations to improve the performance of the STARC-ABL aircraft configuration. This *Single-aisle Turboelectric Aircraft with Aft Boundary-Layer Propulsion* (STARC-ABL) configuration is an hybrid aircraft concept with an aft-mounted electric engine, developed by NASA and depicted in Fig. III.4. The aforementioned optimization study considers the aft-mounted BLI propulsion system and aims at improving its aero-propulsive performance. The design variables are propulsor and fuselage shape parameters, as well as a parameter representing the fan propulsive force. A thermodynamic model enables to consider the shaft power as the function to minimize in the optimization process. Three operating points are considered and optimized (e.g. the one depicted in Fig. III.5).

Figure III.4 – *View of the STARC-ABL hybrid aircraft configuration, from Gray et al. [29]*

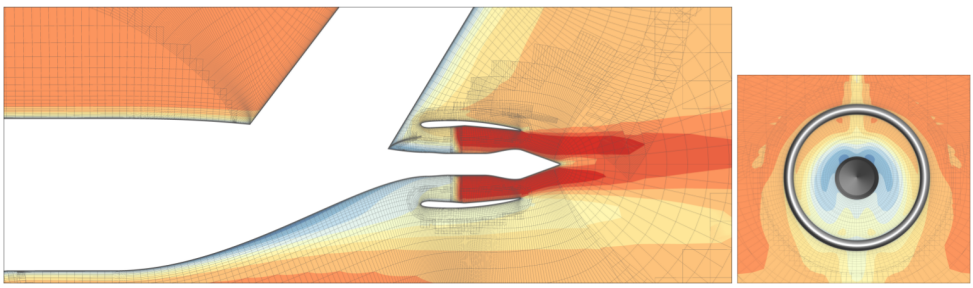

(a) Baseline

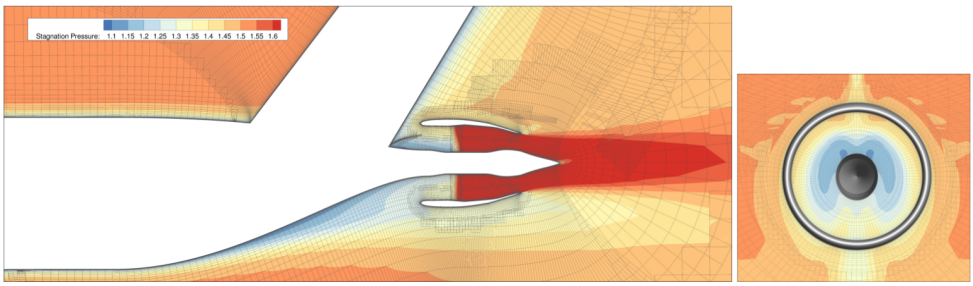

(b) Optimized

Figure III.5 – *Contours of stagnation pressure, adapted from Gray et al. [29]*

These studies show interesting examples of coupled aero-propulsive simulations. For rear-body design, nozzle aerodynamics depend on engine cycle thermodynamics, and the coupling appears essential to assess precisely the effect of shape modifications.

III.4 Summary

On aircraft configurations with under-wing mounted engines, aerodynamic interaction effects appear between the wing and the engine. These interactions, also referred as interference effects, have been studied in the literature. Numerical and experimental work have shown their penalizing effects on the wing and overall aircraft aerodynamic performance. However, negative interference effects actually come from the assembly of wing and nacelle shapes that have been designed to operate in isolated configuration. There is no study where they are optimized in order to improve the performance of the whole aircraft-engine system. This motivates the current work, that aims at modifying nozzle shapes and at accounting aerodynamic wing-engine interactions by considering the overall aircraft-engine performance.
In order to account for engine installation in design phases, an approach based on optimization is considered. Such methods have been applied in previous work to improve the performance of engine nacelles. In particular, some authors have applied aerodynamic shape optimizations for the design of turbofan nozzles. Still, among the few applications to nozzles that can be found, none of them took wing-engine interactions into account. In addition, no shape optimization study on the subject has considered industrial design tools, such as CAD software. This justifies the main objective of this work, that aims at implementing aerodynamic shape optimizations on the nozzles of an installed turbofan, while using an industrial design workflow.
Finally, a new approach has been applied in recent studies, that proposes to perform coupled aero-propulsive simulations for propulsive system design. Such coupling is expected to enable an agreement between nacelle aerodynamics and engine thermodynamics. For rear-body design, the aeropropulsive interdependency is strong, and coupling appears essential to assess precisely the effect of shape modifications for a given engine cycle. Therefore, this innovative approach is expected to be integrated in the aforementioned optimization process, in the scope of the present thesis work.

IV

Development of a strategy for industrial aerodynamic shape optimization with high number of design variables

Contents

This chapter aims at establishing a strategy to perform global and local shape optimization for industrial applications with hundreds of design variables.

At first, optimization methods are investigated, in order to identify the most suitable approaches to deal with high number of design variables while including industrial tools. In particular, the evaluated methods should be appropriate to include CAD software, aerodynamic computations and post-processing tools in the workflow.

Then, knowing that optimization methods usually have a numerical cost that strongly depends on the number of design variables, an approach is developed to reduce dimensionality. This method of *convex combination* proposes to perform optimizations on a sub-space of the design space, which is defined using expert know-how. A first assessment of this approach is performed on a simplified nozzle problem, in order to validate its ability to manage high numbers of variables.

Finally, as the convex combination method represents an innovative way of exploring design spaces, optimization strategies are discussed for its application to industrial

design phases.

IV.1 Investigation of methods for high-dimensional industrial optimization

Function minimization is a field of applied mathematics investigated expansively, due to its various applications. In particular, it is used for aerodynamic shape optimization, that aims at improving the performance of aerodynamic systems by modifying shapes. For instance, a single-objective problem can be written as:

Minimize:

$$J(\vec{\alpha}) \tag{IV.1}$$

Subject to:

$$G_j(\vec{\alpha}) = 0 \qquad j = 1..L \tag{IV.2}$$

$$H_k(\vec{\alpha}) \leq 0 \qquad j = 1..M \tag{IV.3}$$

$$\alpha_i^l \leq \alpha_i \leq \alpha_i^u \qquad j = 1..N \tag{IV.4}$$

where

$$\vec{\alpha} = \begin{bmatrix} \alpha_1 \\ \alpha_2 \\ \vdots \\ \alpha_N \end{bmatrix} \tag{IV.5}$$

J is called the objective function, while $G_{j=1..L}$ and $H_{k=1..M}$ are the equality and inequality constraints of the problem. They represent the functions of interest, and depend on the vector of design variables $\vec{\alpha}$. Each component of this vector has associated lower α_i^l and upper α_i^u bounds.

For instance, a wing drag-minimization problem can be defined with:

- J the aerodynamic drag of the wing, to be minimized,
- G the lift coefficient, that should remain constant,
- H the minimal thickness in different wing cross sections,
- $\vec{\alpha}$ design parameters of the wing, namely the twist, the chord, etc... defined in a certain number of wing sections.

Numerous approaches have been developed to tackle such problems, commonly denoted as *optimization methods*. Reviews of these methods and their developments have been proposed in [53, 52, 86, 72], but this field of research is still active. Usually, these algorithms are sorted by their dependency on the functions of interest sensitivities. Zero-order methods, or *direct* methods, only depend on the values of these

functions in order to perform minimization. This represents a large family of methods, that have the advantage of avoiding sensitivity computations. On the contrary, first and second-order methods rely respectively on the gradient and the Hessian of the functions of interest to find rapidly an optimum on the design space.

From the designer's point of view, it can be more relevant to classify these methods depending on their way of carrying out the design space exploration. In practice, this space is defined by the design variables and their bounds, and the associated response of the functions of interest is often unknown before launching the optimization process. In particular, discontinuities can appear or several local optima can be found. As an illustration, a Rastrigin function [61], comprising numerous local optima and an unique global optimum, is depicted in Fig. IV.1.

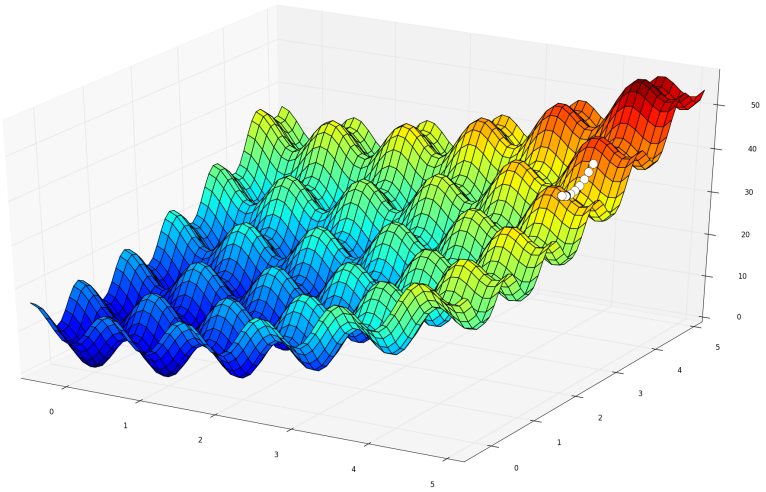

Figure IV.1 – *Descent on a Rastrigin function*

For function minimization, the exploration of the design space performed by the algorithm can be considered *local* or *global*. These ways of exploring are based on different methods, have different limitations, and can be used for different purposes. A non-exhaustive review and classification of the two types is presented in the following sections. In particular, their application to industrial design processes, as the one presented in II.4, is discussed.

IV.1.1 Local design space exploration

The first type of methods uses a step-by-step approach to improve the objective function. These methods start from a chosen design and aim at finding a better shape at each iteration. These methods are considered *local* because they do not ensure that the final optimal point that they find is the best optimum in the defined design space.

First order methods

Although some of them are derivative-free, such as the pattern search methods, most approaches for local research are sensitivity-based. The most frequently used are first-order algorithms, that use the gradient of the functions of interest at the current iteration to determine the next evaluation. *Steepest descent*, but also *conjugate gradient* and *quasi-Newton* methods are the most common first-order approaches. Although gradient computation can seem straightforward for analytical optimization problems, it can become complex with non-linear problems, high number of design variables and when considering industrial cases and complex applications. When the gradient can not be computed analytically, different methods can be used for its evaluation.

The classical method used for gradient estimate is *finite-differences*. A small perturbation, or *step*, is applied on each design variable and the functions of interest are evaluated on the resulting designs. Then, the gradient is estimated with a difference quotient. This approach has the strong advantage of being adapted to any kind of optimization problem and workflow. In particular, it complies with industrial software, without requiring access to their source code. However, the choice of the step size can highly impact the gradient estimate. Moreover, the computational cost associated with the gradient computation is proportional to the number of design variables. With a high number of design variables, this can lead to a prohibitive computational cost. For industrial applications and workflows involving hundreds of parameters, the dependency on step size and the computational cost become a major bottleneck.

An alternate method of sensitivity estimate, the *adjoint* gradient computation, has been introduced in 1988 for aerodynamic shape optimization by Jameson [35]. This method was previously used in optimal control theory [46] and adapted to fluid mechanics by Pironneau [59]. Its principle is based on a Lagrangian formulation of the optimization problem and exploits duality to solve the associated linear system at a cost depending on the number of functions of interest, but independent of the number of variables. In practice, it appears that the adjoint system resolution has approximately the same computational cost as solving the flow equations. Consequently, this approach is particularly interesting for aerodynamic shape optimizations, because they involve high numbers of design parameters, a few functions of interest and expensive flow computations. Since its introduction, it has been applied to optimization problems of growing complexity and for a large variety of applications. For instance, it has been applied to wing design [12, 56], wing-body aircraft configurations [63, 47, 57, 58], aircraft engine nacelles [41, 40, 82], or turbomachinery components [68, 55, 87]. However, there is also a drawback to this approach. The adjoint system and the gradient computation require derivatives of the elements in the optimization workflow. For each tool involved, the sensitivity of its outputs with respect to its inputs has to be provided. These derivatives can be obtained by adapting and differentiating software code, or by using finite differences "locally". When it comes to industrial workflows, based on commercial software and complex design tools such as CAD, sensitivity computations can become a major bottleneck for the use of adjoint-based optimizations.

Second order methods

Second-order approaches are based on Newton's method. They require the Hessian matrix of the functions of interest and aim at finding the zero-values of their gradients. However, the estimate of second-order derivatives is very costly in terms of evaluations. Moreover, their computation is complex and the resulting sensitivities are often altered by numerical noise. For these two reasons, they are often dismissed for industrial applications and will be considered out of the scope of this study. Still, some approaches propose to estimate the Hessian of the objective function based on its gradients, in order to reduce its cost. These methods are designated as *quasi-Newton* and the most famous of them is the *Broyden–Fletcher–Goldfarb–Shanno* (BFGS) algorithm [9, 18, 22, 71].

Summary

To sum up, local methods explore the design space by performing step-by-step improvements of the objective function. Consequently, these algorithms do not guarantee that the optimal solution found at convergence is global. Yet, these methods remain very performant and cost-efficient, and are relevant in many industrial optimization problems. For a high number of design parameters, the cost associated to finite-differences is expected to become prohibitive. In this situation, the adjoint method appears as a good alternative for gradient computation, although it requires the sensitivities of all tools inside the optimization loop.

IV.1.2 Global design space exploration

In contrast with local exploration methods, *global* minimization approaches aim at finding the best value of the objective function on the design space. Consequently, they implement efficient ways of exploring the design space and finding its areas of interest. Most of the methods tackling this ambitious objective consist in zero-order algorithms. They are often nature-inspired or physics-inspired, but can also be purely mathematical. The short survey presented here does not aim at being exhaustive, but rather to give an overview of the numerous methods available for global optimization.

Evolutionary algorithms, developed in the late 1960's [33, 62], belong to the first type of nature-inspired approaches and are based on the Darwinian principle of evolution. Consequently, they consider successive generations of a population and model mechanisms such as mutation, crossover and selection. Among them are the *Genetic Algorithms* (GAs) [49] based on the theory of survival of the fittest and *Evolution Strategies* (ESs) [8]. Recently, the use of such methods has increased for aerodynamic shape optimization [20, 2, 50, 51].
Another type of nature-inspired algorithms mimic biological social systems. A remarkable example is *Particle-Swarm* optimization [37], that models the behavior of a bird flock or a fish school to perform design space exploration.

Then, some methods are inspired from physical phenomenas rather than nature, such as *Simulated Annealing* [83]. This non-deterministic approach reproduces heating and cooling of materials, that enable atoms to reach a configuration with minimal internal energy, to perform minimization.

Finally, some methods are only based upon mathematical processes. The simplest of them are *Random Search* and its variation *Random Walk* [84]. However, the efficicency of such method is limited in comparison with other global research methods. Today, they are often used as part of more complex optimization processes.

To summarize, zero-order methods propose various ways of exploring the design space and search for global optima. They have recently known great developments, thanks to increasing computational capabilities. These approaches are particularly adapted to noisy optimization problems, and do not require any continuity of the design space. Moreover, they enable the use of non-differentiated tools and "black-box" software in the optimization loop. Finally, they can be easily parallelized to increase their response time. However, when applied on aerodynamic design workflows, these methods suffer from the number of evaluations needed for exploration. In particular, the number of iterations until convergence increases rapidly with the number of design parameters. Considering that the evaluation process requires CFD simulations, this can result in a prohibitive overall cost. Therefore, these methods can not be applied on industrial cases with hundreds of parameters.

In order to overcome their limitations, global exploration techniques are often associated with surrogate modeling. This lead to a new field of research, *Surrogate-Based Optimization* (SBO) [60, 19]. The working principle of these methods is to perform an initial DOE on the design space, an to build a surrogate model based on the evaluated samples. Surrogate modeling methods are various, and comprise *Response Surface Models* (RSM), *Kriging* [77], or *Radial Basis Functions* (RBF) among others. Then, a search is carried out to determine new design points to evaluate, which is called *adaptive sampling*. After their evaluation, the process re-builds the surrogate model and repeats the process until a satisfying precision is obtained. Finally, an optimization is performed using the surrogate model, most of the time with evolutionary algorithms. As costly simulations are avoided, these approaches appear as the most competitive to search global optima. SBO has been applied to aerodynamic shape optimization [3, 34] and in particular to nacelle design [74, 24, 25, 26, 23, 81, 79]. Although the surrogate model enables to drastically reduce the cost of the optimization, its construction represents an important expense. In particular, for a high number of design variables, these methods can not be considered.

IV.1.3 Hybrid and enhanced exploration

The limit between local and global exploration is sometimes thin and can be discussed depending on the optimization problem and the design space considered, or personal experience. Moreover, alternative methods have appeared, that do not fit clearly in the previous classification. These methods, often referred as *hybrid* or *enhanced*, are derived from local or global methods and propose to overcome their limitations. Some

approaches have been developed to improve the efficiency of global algorithms, in particular by adding gradient information into the research process [88]. On the other hand, some descent methods can be enhanced to become "more exploratory". Among many possibilities, one is to add a repulsive term in the objective function, based on the proximity to previous evaluations. As an example, a descent with repulsive force has been tested on the Rastrigin function and is depicted in Fig. IV.2.

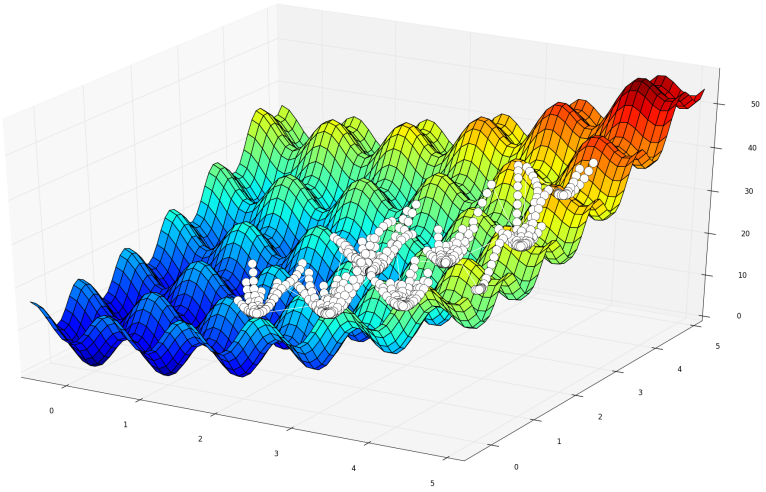

Figure IV.2 – *Descent with a repulsive force term on a Rastrigin function*

IV.1.4 Integration of CAD software in optimization

Computer-Aided Design has become a mandatory tool to manage geometrical models of industrial complexity. Still, the integration of these models in an optimization workflow remains a major challenge. First of all, the great number of design parameters represents a bottleneck for global optimization due to computational cost. On the other hand, local optimizations with adjoint-based gradients are efficient in this situation. Consequently, some research work has been dedicated to compute sensitivities with CAD-based geometries. The most "straightforward" approach to this problem is to compute the sensitivities of the CAD-generated surfaces and shapes by applying finite-differences on the geometric model [64, 65, 13, 78]. However, this process requires topological reconstruction to compute surface sensitivities, and is subject to the limitations of finite-differences. Consequently, a second approach consists in differentiating analytically the geometry-generation process [13] or applying *Algorithmic Differentiation* to the CAD kernel [5]. This enables the exact computation of the surface sensitivities with respect to design parameters. Yet, without access to the CAD source code, these solutions cannot be considered. An alternative method is developed in [93, 92], that uses the control points of *Non-Uniform Rational B-Splines* (NURBS) surface patches as design parameters. This enables to remain in a CAD geometrical representation during and after optimization and can be used with adjoint gradient computations. Still, the link with industrial design parameters and constraints is not respected when using this approach. Finally, some studies choose to perform shape deformation and keep a link with the CAD representation, in order to return an optimal shape that can be interpreted by the model [55, 87].

To conclude, although these methods represent great steps forward in the generalized integrations of CAD software in optimizations, they remain challenging to implement. Consequently, they do not appear to be adapted for the present work case.

IV.1.5 Outcome

This short review of optimization approaches and their implementation shows that both local and global exploration have their advantages and limitations. In this study, the hundreds of design variables and the CFD simulations considered would result in a prohibitive cost with global methods and evolutionary algorithms. Moreover, the surrogate modeling involved in SBO approaches requires a number of evaluations that is not adapted to preliminary design phases.

In this situation, the best alternative appears to be the use of a first-order algorithm with adjoint-based gradient computations, in order to mitigate the cost associated to the dimensionality of the problem. Consequently, a study has been carried out to identify and evaluate the challenges of implementing an adjoint-based approach for under-wing turbofan nozzles. This work is not detailed in the present document, but is presented in Appendix A. The adjoint equations are established step-by-step for the complete optimization problem, while considering coupling processes required for a full aircraft performance assessment. Eventually, this study identifies two bottlenecks for adjoint-based gradient computation:

- Given that access to the source code of the considered CAD software is not available, the surface sensitivities should be computed with finite-differences.
- A dedicated nozzle post-treatment must be implemented and differentiated for adjoint purpose.

In order to overcome these limitations, complex developments and validations are required. In the scope of the present thesis work, the choice is made to propose and validate an alternative approach instead of tackling the development of an adjoint-based workflow. Still, the development, validation and application of adjoint-based optimizations to a CAD-based nozzle design workflow represent an interesting way of following up the present study and can be tackled in future work.

IV.2 Definition of a method based on convex combination of reference shapes

IV.2.1 Method of convex combination based on expert knowledge

A design problem is considered, where geometrical shapes X are defined by a set of parameters $\vec{\alpha} = \{\alpha_1, ..., \alpha_N\}$, with $N \sim 10^2$. This case is representative of an industrial design based on CAD shapes defined by hundreds of parameters.

Then, n geometrical shapes $X_{\{i=1,...,n\}}$ are defined with the geometrical model. Using this shape database, a subspace of the design space can be defined as a simplex $\mathcal{S}$:

$$\mathcal{S} = \left\{ \sum_{i=1}^{n} \lambda_i \vec{\alpha}_i \;\middle|\; \sum_{i=1}^{n} \lambda_i = 1 \text{ and } \lambda_i \geq 0 \;\; \forall i \right\} \tag{IV.6}$$

where $\lambda_i \in [0, 1]$ are barycentric coordinates and $\vec{\alpha}_i$ is the vector of design parameters associated to the shape X_i. Shapes generated with a set of parameters $\vec{\alpha} \in \mathcal{S}$ are *convex combinations* or "morphings" of the shapes of reference $X_{\{i=1,...,n\}}$.

Now, the database of reference shapes is assumed to be composed of designs generated using expert knowledge and industrial know-how. These shapes are generated using for instance the designer's background knowledge, previous shapes database, literature, or by taking physical constraints into account. Therefore, they are referred as *expert configurations*. They can have strong geometrical characteristics, which can even be exaggerated. In particular, these expert shapes are not necessarily industrially feasible, because their purpose is to give "directions of interest". In this case, the designs associated to sets of parameters belonging to the convex set, $X(\vec{\alpha}), \forall \vec{\alpha} \in \mathcal{S}$, inherit of the characteristics of these shapes. The number n of expert shapes is usually comprised between 2 and 10, ensuring that $n << N$.

In this framework, optimizations can be performed on the convex set instead of the full design space. Thus, the dimension of the problem is reduced from N to n and the sets of design variables $\vec{\alpha}$ have been replaced with the barycentric set of coordinates $\Lambda = \{\lambda_1, ..., \lambda_n\} \in [0, 1]^n$.

Finally, this approach results in an alternative way to explore a high-dimensional design space, driven by expert know-how and interest. Only the way to drive the design variables has changed.

IV.2.2 Main advantages and drawbacks

This approach is particularly interesting for preliminary design. Using the expert configurations to define the design space strongly reduces the risk of getting industrially unfeasible designs during optimization. Moreover, contrary to some space reduction methods, no CAD parameter is set apart or ignored *a priori*. Consequently, the complexity of the generated shapes remains the same, and the geometries obtained in the process are still defined from a set of industrial design parameters. Mathematically, this method proposes an original way to explore a high dimensional design space. Because the approach is low-dimensional, functional sensitivities can be evaluated using finite differences for gradient-based optimization. It also reduces the computational cost of gradient-free techniques, so that they become affordable. Finally, thanks to the projection theorem, the solution of this optimization is supposed to be the projection of the global solution on the "expert-based" simplex. This means that, starting from a first solution defined as a convex combination of expert shapes, a second optimization can be run over the entire design space, this time using a method adapted to high dimensionality.

The major drawback of this method is that the generation of new shapes is limited by the set of expert configurations given for the combination. Consequently, in order to introduce new characteristics, not predicted or included in the expert configurations database, some improvements must be made. One of the main ideas is to use successive optimizations and to modify the database depending on previous optimal results. For example, a shape that ends with a null associated barycentric coordinate can be removed from the database. In order to replace this configuration, a new shape, based on random design variables, can be introduced. A second possibility is to use an analogy of the simplex method and to design a shape in the opposite direction, with respect to the other configurations. When no shape can be removed from the database, some of the possibilities evoked can be useful to enrich the database. This enables to reduce the limitation induced by the database, and to make the method "more exploratory".

IV.2.3 Assessment on a simplified nozzle case

In order to demonstrate the abilities and the relevance of the convex combination approach on problem with large numbers of design variables, a test case representing a simple nozzle problem is defined.

Let $r : [0,1] \mapsto \mathbb{R}^+$ be a continuous function defined representing the radius of an x-axisymmetric nozzle wall (see Fig. IV.3(a)). Consequently, $x = 0$ represents the axial position of the nozzle injection and $x = 1$ its exhaust. X is the curve associated to r. An inviscid fluid flows through this nozzle. Only the mean flow values in x sections are considered, so that the problem becomes mono-dimensional and only depends on x. Assuming that the flow is steady, incompressible, irrotational and isentropic, Bernoulli's equation applies [11]. Introducing (ρ, p, V) as the flow density, static pressure and axial velocity at a given x, this yields:

$$\forall x \in [0,1], \frac{V(x)^2}{2} + \frac{p(x)}{\rho} = \frac{V_0^2}{2} + \frac{p_0}{\rho} \tag{IV.7}$$

where the 0-state is a reference upstream state of the nozzle flow. Thanks to the mass flow conservation, V can be related to the nozzle section S, that is expressed with respect to r:

$$\forall x \in [0,1], V(x) = \frac{V_0.S_0}{\pi.r(x)^2} \tag{IV.8}$$

Therefore, when V is replaced in Eq. IV.7, the pressure can be computed on every point of the wall with:

$$\forall x \in [0,1], p(x) = p_0 + \frac{\rho.V_0^2}{2}\left(1 - \left(\frac{S_0}{\pi.r(x)^2}\right)^2\right) \tag{IV.9}$$

This first application is an inverse optimization problem. An arbitrary analytical

function X_{target} is chosen as the optimal wall design and the process aims at retrieving this shape, based on the associated pressure distributions in the nozzle. The coordinate x is discretized on the interval $[0, 1]$ to create a design vector r_i of dimension $N = 300$:

$$\forall i \in [\![1, ..., N]\!], x_i = \frac{i}{N} \text{ and } r_i = r(x_i)$$

Then, the cost function to be minimized is defined as:

$$J = \sum_{i=0}^{N} (p(x_i) - p_{target}(x_i))^2 \tag{IV.10}$$

Four nozzle geometries denoted $\{X_1, X_2, X_3, X_4\}$ are considered as "expert configurations". These shapes are displayed on Fig. IV.3(a). Three of these shapes have a throat, at different locations and with different sections ; one has a constant section.

A simple gradient-based descent algorithm is implemented and used for the descents presented in this section. The gradient is computed at each iteration by forward finite differences and an elementary step size adaptation is used. The descent algorithm starts from the barycenter of the subspace defined with convex combination, at $\{0.25, 0.25, 0.25, 0.25\}$, and is stopped after 500 iterations.

Two test cases are considered, which differ on their target shapes. At first, the target shape X_{target} is defined as a combination of the expert configurations, in order to assess the capability of this method to retrieve a shape inside the convex space. The convergence of the descent algorithm, displayed on Fig. IV.3(b), shows that it converges towards the optimum in approximately 300 gradient iterations. Moreover, the shapes observed on Fig. IV.3(a) confirm that the descent method is capable to find the optimal design. On this figure, the slight discrepancy between the optimal shape and the target is due to the low gradient values at the end of the search process. The descent slows and the limited number of iterations does not permit to have a complete match of the curves.

Then, the target shape is defined by a random analytical function that does not belong to the convex set. The descent on the reduced search space is compared to the descent in the full design space on this case. The optimal shapes and the convergence rates of the algorithm can be observed on Fig IV.4(a) and IV.4(b) respectively. It appears on Fig. IV.4(a) that the optimal shape on the full design space approaches more precisely the target shape than the shape defined as a convex combination of expert configurations. This result confirms that proposed method of search space reduction can limit the optimization search. However, despite the disparity of the expert configurations, a good convergence toward the solution can also be observed with the convex combination method. Moreover, the optimal combination is obtained in approximately 60 gradient iterations, compared to the 100 needed on the full design space. When considering the number of evaluations until convergence, the convex combination method appears to reduce drastically the cost of the process, totalizing 240 evaluations instead of 30,000. This is mainly due to the cost of gradient computations, needing $n = 4$ evaluations on the reduced space instead of $N = 300$ on the complete design space.

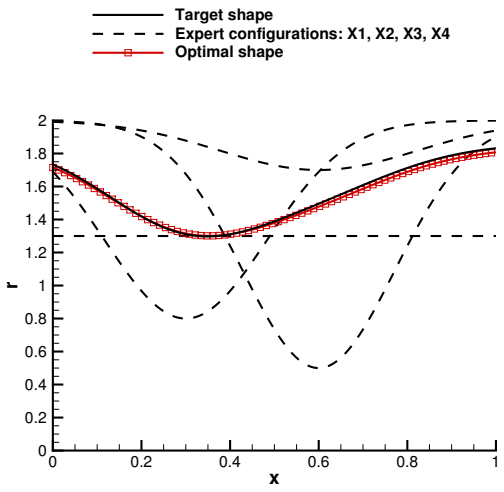

(a) Expert configurations, target and optimal nozzle shapes

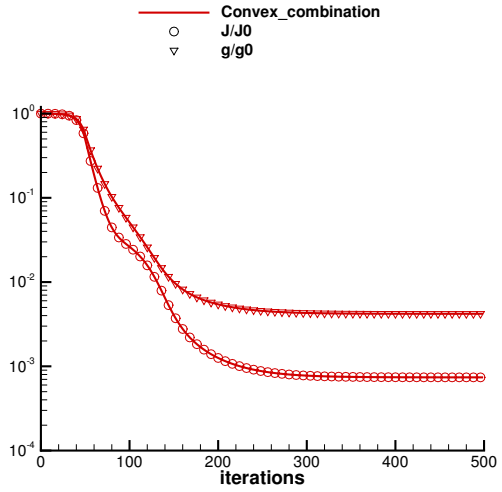

(b) Evolution of the normalized values of the cost function J and its gradient g

Figure IV.3 – *Gradient-based optimization on the space defined with convex combination, for a target shape belonging to the convex set*

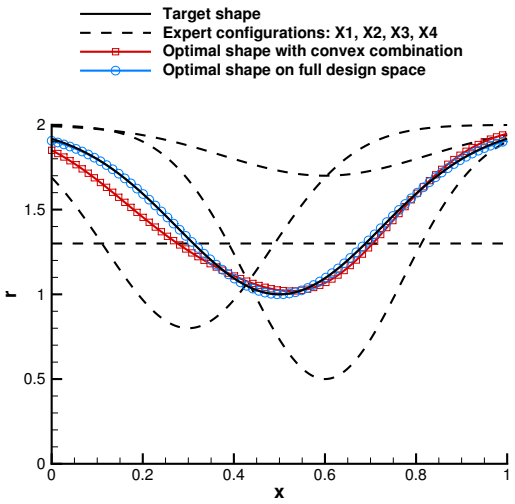

(a) Expert configurations, target and optimal nozzle shapes

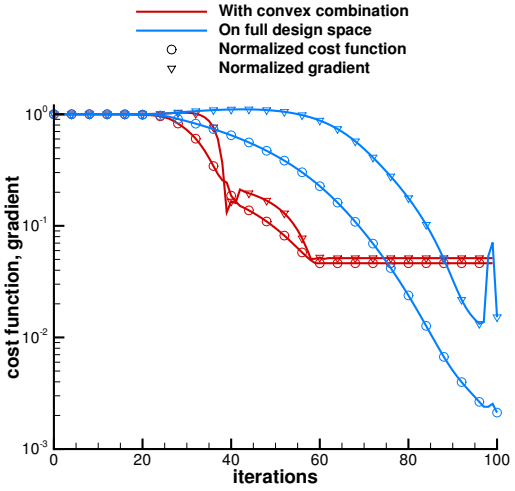

(b) Evolution of the normalized values of the cost function J and its gradient g

Figure IV.4 – *Comparison of gradient-based optimizations on the full design space and on the space defined with convex combination, for a target shape outside the convex set*

In conclusion, the proposed convex combination method has proven its ability of dealing with highly dimensional design spaces on a simple inverse optimization problem. Due to the ratio n/N, the cost of gradient computations is reduced in this case by a factor of 133 for descent algorithms. Moreover, although the optimal shape obtained on the reduced space may not be as optimal as the result of the search on the full design space, this method appears as an efficient way to approach the optimum for industrial CAD-based design problems. In the following, this method is applied to an industrial aerodynamic shape optimization problem.

IV.3 Establishment of industrial optimization strategies based on convex combination

IV.3.1 Development of optimization strategies

Convex combination appears as a promising method to deal with high dimensional optimization problems, in particular when they include non-differentiated software. This method proposes to explore a subspace of the complete design space, and can therefore be considered as a "more global" research than a gradient-based descent on the latter. However, the optimum obtained is constrained to belong to the subspace. Consequently, some ideas of optimization strategies based on this method have emerged.

First, the convex combination method can be used alone, but in an original and innovative design process. It enables designers to propose shapes and returns an optimum based on them. Moreover, the coordinates of the optimal combination can be interpreted and confirm/invalidate their intuitions. Based on this result, they can modify the database by adding, removing or replacing shapes and re-launch the optimization. Thanks to the small dimensionality, the optimization return time is very short. Therefore, an iterative design process appears, at the heart of which stands the designer, interacting with the optimizer (see Fig. IV.5).

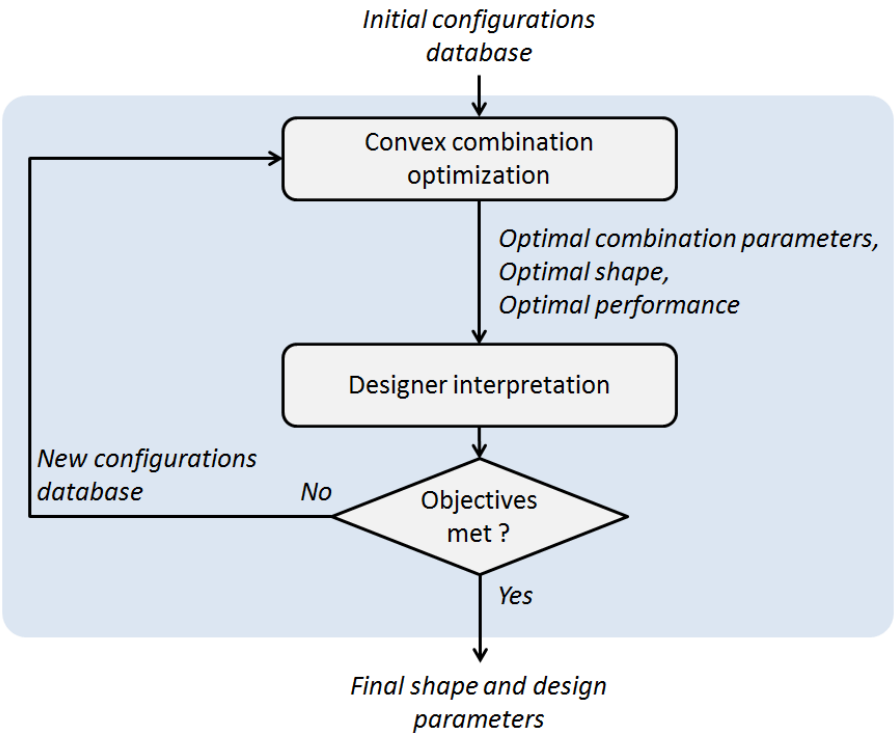

Figure IV.5 – *Principle of the iterative design strategy based on rapid optimizations*

Another possibility is to see convex combination as part of a larger optimization process. In particular, it can be considered as the first step of a two-level optimization strategy. In such framework, convex combination is the first optimization level, and the reduced number of parameters enables to find the optimal combination at a relatively low cost. The goal of this step is to find a region of interest of the design space. Then,

all design variables are considered and a gradient-based descent is launched over the complete design space. This second level of optimization starts from the shape obtained with the optimal combination. The role of this step is to refine the search and find an optimal design in the vicinity of the first solution (as depicted in Fig. IV.6).

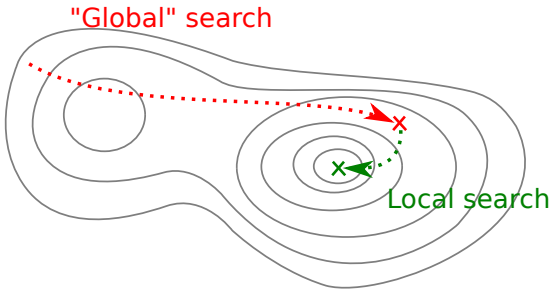

Figure IV.6 – *Illustration of the two-level optimization strategy*

The two strategies presented here are only examples of how the convex combination approach can be applied to industrial problems. They illustrate that this method, although having some well-identified drawbacks, represents an interesting tool to assist industrial engineers in design phases. Finally, the two-level strategy is assessed on a simple case, in order to have a first idea of its feasibility and cost.

IV.3.2 Assessment of a two-level strategy on a basic nozzle case

In order to demonstrate the capabilities of a two-level strategy and evaluate its cost, the methodology has been tested on the 1D nozzle case, presented in IV.2.3.

For this example, it is considered that the first level process is achieved through a gradient-based descent algorithm, on a subspace defined with convex combination. Consequently, the starting point of the second level research is chosen as the result obtained in IV.2.3. The optimal combination is found on the subspace defined with $\{X_1, X_2, X_3, X_4\}$, and considered converged after 100 iterations. From this shape, depicted in red on Fig. IV.7, the descent algorithm based on finite differences method is re-applied. This time, all 300 parameters are considered and the optimal research explores the complete design space, in order to achieve a full convergence toward the optimal shape X_{target}. The program of the second optimization level is stopped after 500 iterations.

The final resulting shape is very close to the target shape, and can be observed in green on Fig. IV.7. This confirms the possibility of refinement when using a second optimization level with a local algorithm. Still, the number of iterations needed to achieve such level of precision is important. Moreover, the gradient computed with finite differences are more expensive in terms of evaluations than for the first phase, due to the number of design variables (300 against 4 previously).

To sum up, it appears that the two-level strategy has interesting features for future applications. The first level with convex combination enables to get closer to the optimal solution at a reduced cost. Then, the second and complementary descent on the full design space enables to reach an improved optimum. After 10,000 iterations, the

2-level strategy achieves a cost function reduction by a factor of 500 against 1.25 for the full-space descent. Consequently, this strategy appears to offer an overall acceleration of the optimum research. However, it should be noted that for industrial applications, a second optimization level using gradient-based methods with high numbers of design variables can only be implemented using the adjoint approach.

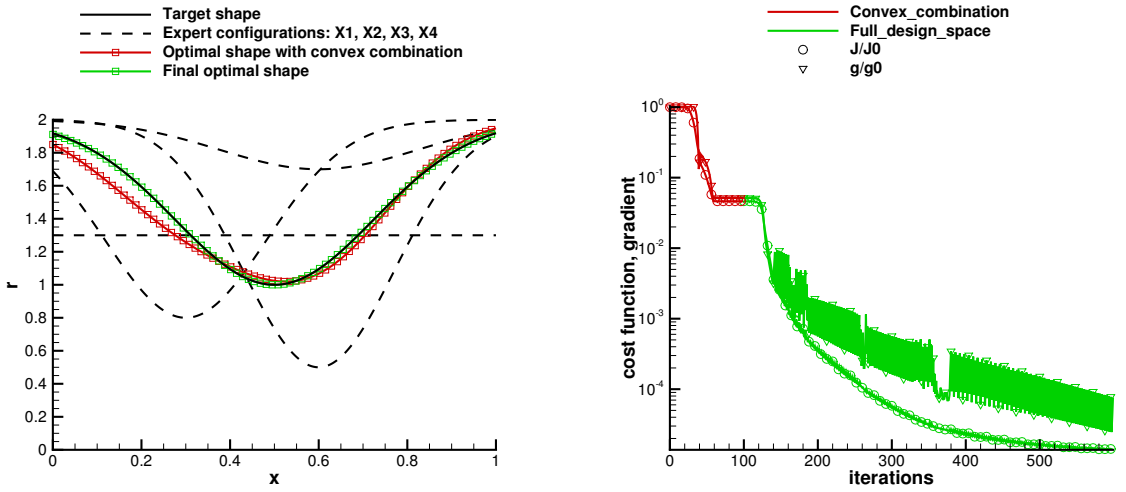

(a) Expert configurations, target and optimal nozzle shapes

(b) Evolution of the normalized values of the cost function J and its gradient g

Figure IV.7 – *Finite-difference optimization launched from the convex combination optimum, for a target shape outside the convex set*

IV.4 Chapter summary

Despite the numerous optimization methods available, the work case presented here appears challenging on several aspects. A short review has showed that both local and global design space exploration algorithms have strong limitations when applied with a high number of parameters and non-differentiated software at the same time. Therefore, a method has been presented to reduce the dimensionality of the optimization problem based on expert knowledge. This approach, called *convex combination*, has been specially developed to introduce CAD geometries in optimization workflows. Moreover, it allows the use of gradient-based and gradient-free methods on a subspace of the design space. A test on a simple analytical nozzle case has validated the interest of this method and shown that it drastically reduces the number of evaluations required for optimization. Finally, some examples of industrial design and optimization strategies based on convex combination have been discussed. In the following, the work will focus on the application of this method to nozzle cases of increasing complexity.

V

Performance optimization for an axisymmetrical single-flow nozzle

Contents

The objective of this chapter is to apply the convex combination approach defined in Chapter IV on a first nozzle case with a CFD workflow.

First, an optimization problem is defined to improve the performance of a single-flow nacelle. This case and its definition are detailed, and the associated workflow comprising mesh deformation and CFD is presented.

Then, an ideal one-dimensional representation of the nozzle is considered. In this case, the isentropic relations give some properties of the shape with best theoretical efficiency.

Next, optimizations are performed on the axisymmetrical nozzle, using feasible descent methods and inviscid flow computations. These first optimizations on the entire design space enable to validate the workflow. Moreover, they establish first optimal nozzle results that are compared with isentropic theory.

The convex combination method is then applied to the single-flow nozzle with inviscid computations. The feasible descent is operated on the reduced search space, defined with three "expert" configurations. This is the first assessment of the convex combination method on a case of medium complexity. It confirms the interest of this method and gives interesting results in comparison to previous optimum results.

In order to check if the optimum obtained with the descent method on the subspace is global, a design of experiments is implemented. A seeding is generated and evaluated, and interpolations are used to generate response maps for the functions of interest. This enables the comparison between the best feasible point on the map and descent optimum.

Then, viscous flow computations are implemented in the optimization workflow. Again, a gradient-based descent method is applied for the optimizations. The full design space is considered first, and then compared to the convex combination domain. A DOE is performed, that gives useful information to the designer and motivates an enrichment of the combination database.

Finally, the formulation of this optimization problem is discussed *a posteriori*. In particular, the influence of a discrepancy on the mass flow constraint is evaluated. This enables to highlight guidelines and good practices for future cases.

V.1 Development of an optimization problem and workflow to improve the performance of an axisymmetric single-flow nozzle

V.1.1 Definition of an axisymmetric nozzle geometry

For the first application of convex combination with a CFD-based optimization workflow, a simple geometry is defined. This nozzle, inspired from the work of Toubin et al. [82], is based on an experimental through-flow nacelle, called DLR-F6 [66].

Initially, these geometries are used for wind tunnel testings in order to evaluate the installation effect of a nacelle on the aircraft aerodynamics (as shown on Fig. V.1). In the present case, a through-flow geometry is modeled into an axisymmetric body, comprising a single-flow nozzle without central body. Two planes are added to the configuration, in the inlet and the nozzle, to enable the definition of engine inflow and nozzle injection boundary conditions for the aerodynamic computation. The resulting configuration is depicted in Fig. V.2.

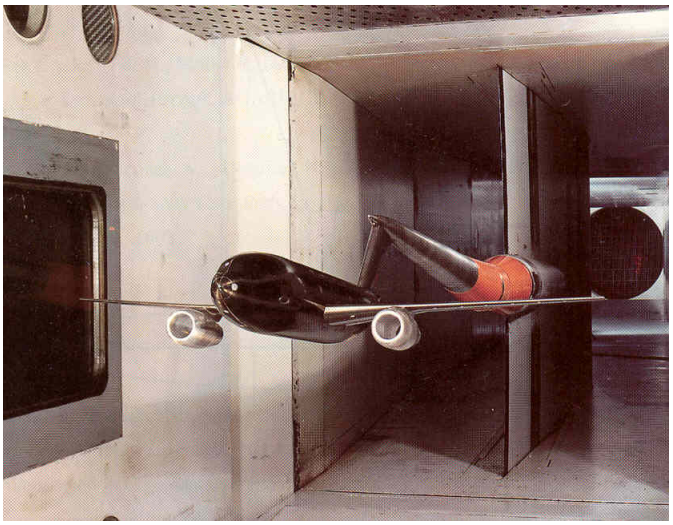

Figure V.1 – *Overview of an experimental setup for windtunnel testing of an aircraft model with a DLR-F6 through-flow nacelle (from Rossow et al. [66])*

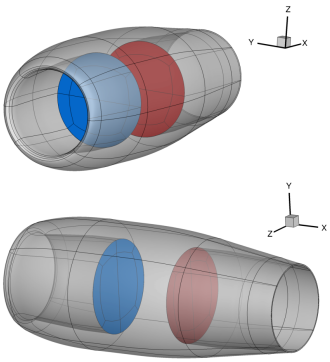

Figure V.2 – *Three dimensional views of the axisymmetric single-flow nacelle*

V.1.2 Meshes generation for inviscid and viscous flow computations

In order to perform flow simulations around the nacelle, two types of meshes are generated. One is dedicated to inviscid flow computations and the other to viscous flows. Both grids take into account the axisymmetry of the geometry and are defined as 2D planar meshes. They are presented on Fig. V.3 and Fig. V.4 respectively.

The first mesh generated for inviscid computations totalizes approximately $264 \cdot 10^3$ cells. Due to computational instabilities, the mesh has to be refined in the nozzle with respect to the axial direction, justifying the high overall number of cells.

The second has a refined point distribution in the vicinity of the walls, in order to compute the viscous boundary layer. However, the instabilities witnessed with Euler computations are not reproduced with RANS equations and the refinement defined for the inviscid case is not necessary. Therefore, the cell-count of this mesh is lower than in the inviscid case with $106 \cdot 10^3$ cells, which can appear counter-intuitive in the first place. As a validation, a similarly refined viscous grid was generated, resulting in $293 \cdot 10^3$ cells. After computation, no significant change of the functions of interest has been observed and the lighter mesh is kept for RANS simulations.

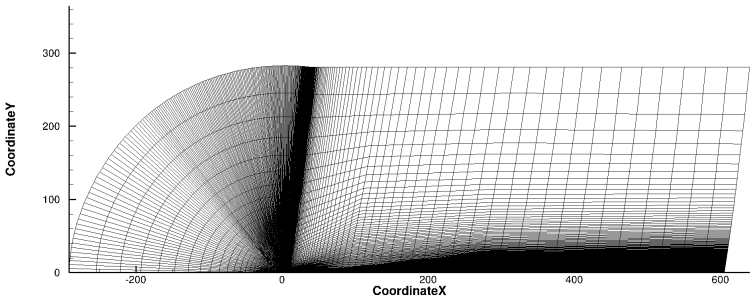

(a) General overview

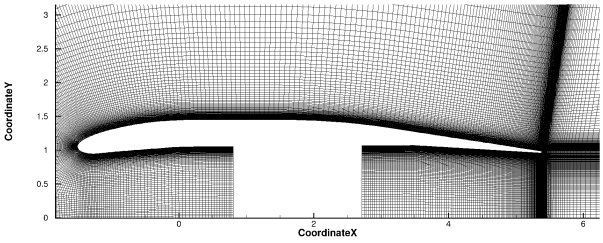

(b) Zoom

Figure V.3 – *Views of the mesh generated for inviscid flow computations*

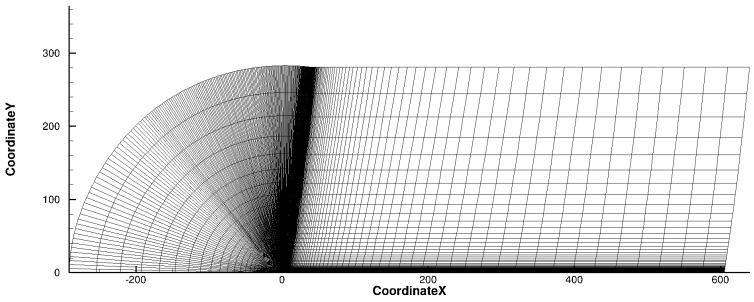

(a) General overview

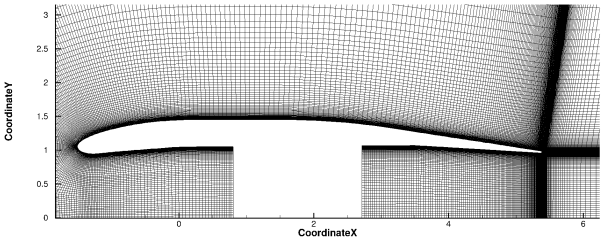

(b) Zoom

Figure V.4 – *Views of the mesh generated for viscous flow computations*

Table V.1 – *Infinite upstream quantities for the axisymmetric nacelle aerodynamic computations*

Quantity	Value
p_∞	$23,849\ Pa$
T_∞	$228.8\ K$
ρ_∞	$0.3632\ kg.m^{-3}$
$p_{i\infty}$	$37,091\ Pa$
$T_{i\infty}$	$259.6\ K$

V.1.3 Computation of boundary conditions for aerodynamic computation

The boundary condition types are inherited from well-known practice for nacelle aerodynamic simulations. The outflow boundary condition located in the inlet is defined with a static pressure, while the inflow boundary condition in the nozzle is specified with total pressure and enthalpy (see Fig. V.5).

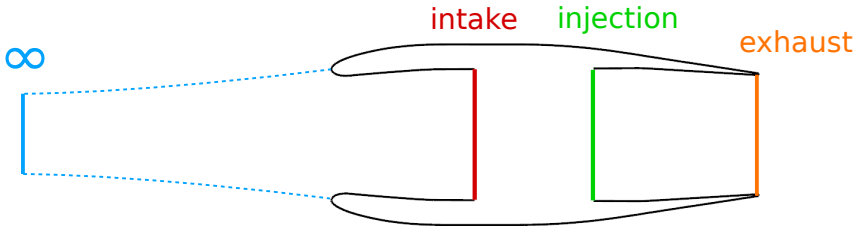

Figure V.5 – *Schematic view of the axisymmetric single-flow nacelle for boundary conditions computation*

Infinite upstream state and inlet

Cruise flow conditions are defined at the far-field borders of the computational domain, for a Mach number of 0.82 and an altitude of 35,000 feet with zero angle of attack. The quantities of the infinite upstream state are computed with an atmospheric model and presented in Table V.1.

Stagnation temperature is conserved from the infinite upstream up to the plane defined in the inlet, yielding : $T_{i\,\infty} = T_{i\,intake}$. The inlet is supposed to have an efficiency of $\eta_{inlet} = 0.995$ (that value has been estimated and then updated with a preliminary computation):

$$p_{i\,intake} = \eta_{inlet}.p_{i\,\infty} \tag{V.1}$$

Supposing a Mach number in the intake plane $M_{intake} = 0.5$, the static pressure and temperature in this plane are obtained with isentropic relations (reminded in Eq. V.2 and V.3) applied at the intake.

$$p = p_i.(1 + \frac{\gamma - 1}{2}.M^2)^{\frac{-\gamma}{\gamma - 1}} \tag{V.2}$$

$$T = T_i.(1 + \frac{\gamma - 1}{2}.M^2)^{-1} \tag{V.3}$$

The mass flow rate can then be computed in the "intake" plane, depending on the density ρ, the flow velocity V and the intake plane area S_{intake}:

$$\dot{m} = (\rho.V.S)_{intake} \tag{V.4}$$

Finally, by using the state equation of perfect gas to replace ρ and expressing the velocity with the Mach number, it yields:

$$\dot{m} = \sqrt{\frac{\gamma}{r}}.\left(\frac{p.M.S}{\sqrt{T}}\right)_{intake} \tag{V.5}$$

Knowing that $\gamma = 1.4$, $r = 287.06\ J.kg^{-1}.K^{-1}$ and $S_{intake} = 3.560\ m^2$:

$$p_{intake} = 31,112\ Pa \text{ and } \dot{m} = 240.67\ kg.s^{-1}$$

Nozzle injection plane

The geometry is a simplified engine nacelle and does not aim at fully representing all characteristics of a realistic engine configuration. However, some conditions should ideally be fulfilled to be as representative as possible of an aircraft engine in cruise conditions:

- Respect of the pressure ratio between the inflow and the flow injected in the nozzle.
- Temperature elevation through the engine.
- Conservation of the mass flow rate between inlet and nozzle injection plane.

Still, it appears that these conditions can not be respected simultaneously for the simple nozzle case studied here.

As the geometry comes from an experimental through-flow nacelle without central body, the inlet and nozzle sections are roughly the same. When trying to apply an adiabatic compression between the entry and the nozzle injection plane, the mass flow rate can not be conserved. Consequently, a compromise has been made in order to generate a set of boundary quantities for aerodynamic computations. The pressure ratio between the two planes is imposed in order to generate an established sonic flow in the nozzle. Then, the mass flow rate conservation is obtained by raising artificially

the isentropic temperature of the flow injected in the nozzle. Therefore, the nozzle flow has a high temperature, in disagreement with actual engine configurations.

The boundary condition in the injection plane is defined with the pressure ratio in the engine $\frac{p_{i\,injection}}{p_{i\,intake}} = 1.7$. This value is considered high for turbofan engines, but it ensures that the flow is sonic and established in the nozzle. It implies a stagnation pressure $p_{i\,injection} = 62,739\ Pa$. Defining the nozzle pressure ratio as $\frac{p_{i\,injection}}{p_\infty}$, this gives $NPR = 2.63$.

The stagnation pressure ratio between the injection plane of the nozzle and the exhaust is defined as $\eta_{nozzle} = \frac{p_{i\,exhaust}}{p_{i\,injection}}$. As for the ratio in the inlet, the value of η_{nozzle} is estimated and then updated with preliminary flow computations, leading to $\eta_{nozzle} = 0.997$. The reference nozzle shape is strictly convergent, meaning that the throat of the nozzle is located at the exhaust. The flow is sonic in this plane and $p_{exhaust}$ can be obtained with the isentropic relation on pressure (see Eq. V.2). Then, the state equation of perfect gas gives the temperature at the exhaust and $T_{i\,exhaust}$ is computed with Eq. V.3. Between the injection of the nozzle and the exhaust, stagnation temperature is conserved such that $T_{i\,exhaust} = T_{i\,injection}$. Finally, total specific enthalpy is established as $h_{i\,injection} = c_p.T_{i\,injection}$

In this case, the mass flow rate in the nozzle is supposed to be identical to the mass flow rate entering the engine $\dot{m}$, and the exhaust area is $S_{exhaust} = 2.880\ m^2$. This yields $h_{i\,injection} = 919.4 \cdot 10^3\ J.kg^{-1}$.

V.1.4 Formulation of the optimization problem

The goal of this work is to increase the efficiency of the nozzle. This problem can be considered in several ways, but the choice has been made to maximize thrust for fixed operating conditions. Let ρ and $\vec{V}$ be the density and the velocity respectively, the momentum conservation in the nozzle (see Fig. V.6) gives:

$$\int_S \rho\vec{V}(\vec{V}.\vec{n})dS = \int_S \overline{\overline{\sigma}}.\vec{n}dS \tag{V.6}$$

with $S = S_{injection} + S_{wall} + S_{exhaust}$ and $\overline{\overline{\sigma}}$ defined as the sum of the pressure and viscous stresses $\overline{\overline{\sigma}} = -p\overline{\overline{I}} + \overline{\overline{\tau}}$.

The surface integrals are developed and the equation becomes:

$$\begin{aligned}\int_{S_{injection}} \left[\rho\vec{V}(\vec{V}.\vec{n}) - \overline{\overline{\sigma}}\vec{n}\right] dS + \int_{S_{exhaust}} \left[\rho\vec{V}(\vec{V}.\vec{n}) - \overline{\overline{\sigma}}\vec{n}\right] dS \\ = \int_{S_{wall}} \overline{\overline{\sigma}}.\vec{n}dS\end{aligned} \tag{V.7}$$

The left-hand side terms of Eq. V.7 can be associated to the "impulsion" $\mathcal{F}$ defined by Candel [11] (p.218) expressed in the viscous case. Fixing the operating conditions,

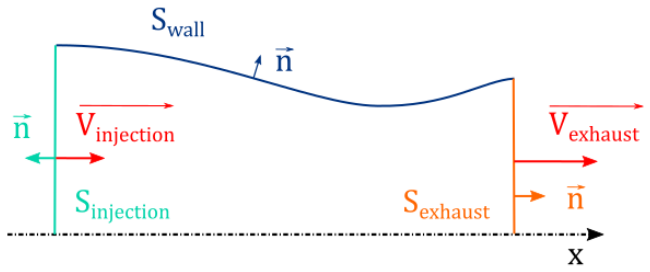

Figure V.6 – *Schema of the nozzle for momentum conservation*

implies that the first term, $\mathcal{F}_{injection}$, remains constant. The second term, $\mathcal{F}_{exhaust}$, participates significantly to the thrust of the engine. To maximize $\mathcal{F}_{exhaust}$, it is necessary to maximize the right-hand side of the equation.

Finally, the optimization problem is defined as the minimization of a function J:

$$J = \left[\int_{S_{wall}} -\overline{\overline{\sigma}}.\vec{n}dS\right].\vec{x} \tag{V.8}$$

In the inviscid case, this term reduces to the integral of pressure at the walls of the nozzle.

Considering Eq. V.7, it also appears that increasing the mass flow rate $\dot{m} = \int_{S_{exhaust}} \rho\vec{V}.\vec{n}dS$ is favorable to thrust. In this study, the target is to maximize thrust at a given value of $\dot{m}$. Therefore, an upper constraint $\dot{m} < \dot{m}_{target}$ is defined for the optimizer.

V.1.5 Workflow and associated tools

The optimizations are performed with Dakota [1], using DOT's modified method of feasible descent [85] to explore the constrained design space. A workflow dedicated to aerodynamic design has been used to perform the optimizations (see Fig. V.7).

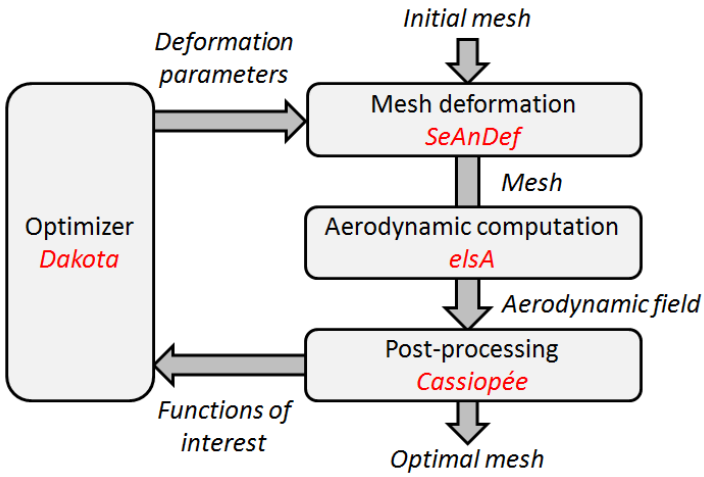

Figure V.7 – *Optimization workflow steps and associated software*

Mesh deformation and design variables

For this first case, which aims at validating the convex combination method and the optimization strategy, the use of a CAD modeler is not mandatory. It can be replaced with a relevant parameterization method, as long as it is adapted to generate shapes that are consistent with nozzle theory. Consequently, the choice is made to keep a similar workflow as Toubin et al. [82] and to use the same nozzle design tool. The parameterization is based on an analytical deformation of a reference mesh, using *SeAnDef* (Sequential Analytical Deformation). This in-house code developed at ONERA applies spline deformations based on control points and has been used in previous optimization workflows [47].

The study focuses on the shape optimization of the nozzle, located downstream of the injection plane. Consequently, seven control points are defined on the internal wall, as shown on Fig. V.8. The point distribution is refined in the vicinity of the exhaust, because this region is expected to have a critical influence on the nozzle aerodynamics. The inlet is considered fixed and the external wall of the nacelle is only influenced by the radial position of the trailing edge.

At each point, the parameter driving the deformation in the radial direction becomes a design variable, resulting in 7 degrees of freedom for the optimization.

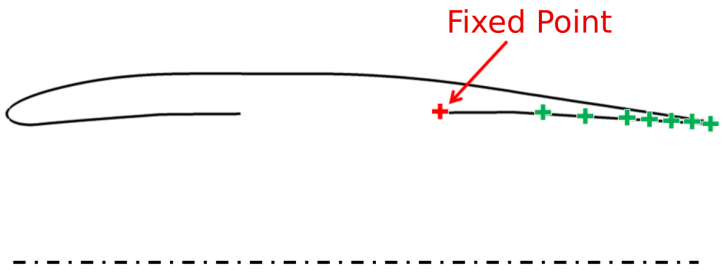

Figure V.8 – *Setup of control points (in green) defined for the mesh deformation*

Numerical setup

The elsA solver [10] (ONERA-Airbus-SAFRAN property) is used for the CFD simulations of the airflow around the nacelle. As the meshes are planar, the computations are operated with an axial symmetry condition, around the x-axis.

The main numerical parameters can be found in Table V.2 for each modeling approach.

Post-processing

After the convergence of aerodynamic computations, integrated values are provided by the solver at the planes where boundary conditions are applied. They are used to

Table V.2 – *Numerical parameters for inviscid and viscous flow computations*

Flow equations	Euler	RANS
Turbulence model	/	Spalart-Allmaras
Spatial scheme	Roe	Jameson
Pseudo-time stepping scheme	Backward Euler and LUSSOR implicit phase scalar	

compute the quantities of interest (mass flow rate, pressure and friction stresses at the wall for instance).

V.2 Monodimensional isentropic computation of the best efficiency nozzle

In order to get a first and simple understanding on nozzle flows, an isentropic flow hypothesis can be considered. This method enables a first understanding of the nozzle aerodynamics, and gives information about the shape associated to maximal performance.

The operating conditions in the nozzle are chosen such that it is sonic at the throat. For a given NPR, i.e. a given level of stagnation pressure at the entry of the nozzle, the shape has an effect on the static pressure level in the exhaust plane. In this case, three flow regimes can appear in the nozzle: overexpanded, adapted or underexpanded (see II.3.3). In order to obtain an adapted regime and maximize nozzle efficiency, it can be necessary to have a convergent-divergent geometry. On such shapes, the sonic throat is followed by a diverging shape, in which the flow is accelerated at supersonic speed before the exhaust.

Knowing the stagnation pressure injected at the entry of the nozzle, the section ratio $\frac{S_{exhaust}}{S_{throat}}$ necessary to reach the ideal case can be computed. By considering an adapted nozzle, $p_{exhaust} = p_\infty$. The isentropic flow induces that the stagnation pressure is conserved in the absence of shocks and $p_{i\,injection} = p_{i\,exhaust}$. Then, using the isentropic relations:

$$M_{exhaust} = \left(\frac{2}{\gamma - 1} \left[\left(\frac{p_{exhaust}}{p_{i\,exhaust}} \right)^{\frac{1-\gamma}{\gamma}} - 1 \right] \right)^{\frac{1}{2}} \tag{V.9}$$

With the Mach number at the exhaust, the section ratio between the exhaust and

the sonic throat can be obtained:

$$\frac{S_{exhaust}}{S_{throat}} = \left(\frac{\gamma+1}{2}\right)^{-\frac{\gamma+1}{2(\gamma-1)}} \frac{\left(1+\frac{\gamma-1}{2}{M_{exhaust}}^2\right)^{\frac{\gamma+1}{2(\gamma-1)}}}{M_{exhaust}} \tag{V.10}$$

In the case of the DLR-F6 computations, a NPR of 2.63 has been chosen to ensure that the nozzle is sonic. For this pressure ratio, a Mach number $(M_{exhaust})_{ideal} = 1.262$ is necessary to reach the adaptation. Only a convergent-divergent nozzle is capable of accelerating the flow to supersonic speed. Therefore, it is expected to generate such shapes to reach the best nozzle efficiency. Moreover, the associated section ratio is expected to be $\left(\frac{S_{exhaust}}{S_{throat}}\right)_{ideal} = 1.051$.

To conclude, this first and simple computation is based on strong hypotheses, but gives an idea of the nozzle flow physics. It explains the interest of considering convergent-divergent nozzle shapes, and gives some characteristics of the "ideal" nozzle.

V.3 Inviscid performance optimization of the nozzle, using feasible descent on the entire design space

V.3.1 First optimization result

The first optimization performed with this axisymmetric nozzle is launched over the full design space of dimension 7. The objective of this case is to validate the workflow and to provide a first optimization result.

The starting point of the optimization is the reference design of the nozzle, which is a simply convergent nozzle (see Fig. V.9). After 5 gradient iterations and 89 evaluations, the optimizer leads to a convergent-divergent optimal shape.

This shape depicted in Fig. V.9 has an area ratio $\frac{S_{exhaust}}{S_{throat}} = 1.012$, which appears to be smaller than the ratio calculated *a priori* with 1D isentropic computations. Moreover, the throat is located at 95% of the nozzle length. The performance and the characteristics of this nozzle are compared with the reference shape in Table V.3.

This first result validates the workflow and the ability of the optimizer to manage the constrained minimization problem. It also demonstrates that the process can create convergent-divergent nozzle, starting from a simple convergent shape. Mostly, it shows that the problem defined with 2D Euler computations leads to convergent-divergent shapes in order to improve nozzle efficiency. Although the area ratio is different than predicted with isentropic nozzle theory, certainly due to 2D effects of the flow, this validates the consistency of the developed approach.

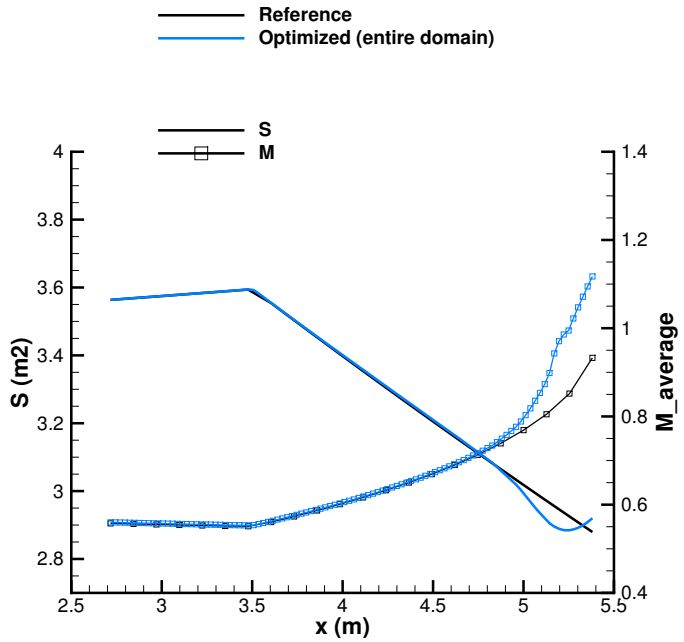

Figure V.9 – *Evolution of the area and the Mach number through reference and optimal nozzle shapes (inviscid computations)*

Table V.3 – *Geometrical characteristics and performance of the nozzle configurations, evaluated with inviscid computations*

Configuration	Section ratio	Throat location (% of nozzle length)	Objective function J/J_{ref}	Constraint $\dot{m}/\dot{m}_{target}$
Isentropic theory	1.051	/	/	/
Reference	1.000	100	1.0000	0.9995
Full domain research optimum	1.012	95	0.9932	1.000

V.3.2 Local character of the optimal solutions

By nature, steepest-descent optimization algorithms converge following gradients and can get stuck in local optima. In order to know if the optimum found by exploring the full design space is local or global, the starting point of the optimization is modified.

The algorithm is launched again from a convergent-divergent nozzle shape instead of the reference. This nozzle has a throat located upstream of the exhaust, a section ratio of $\frac{S_{exhaust}}{S_{throat}} = 1.051$ and does not satisfy the mass flow contraint. Its characteristics and performance are indicated in Table V.4. The feasible descent operated on the full domain and launched from this shape converges towards a convergent-divergent shape. The starting and optimal nozzles are depicted in Fig. V.10 and compared with the previous optimization result from V.3.1.

Again, the optimum confirms the tendency of choosing convergent-divergent shapes to improve nozzle efficiency, in agreement with one-dimensional isentropic nozzle theory. Moreover, it appears that despite different starting points, both optimal nozzles

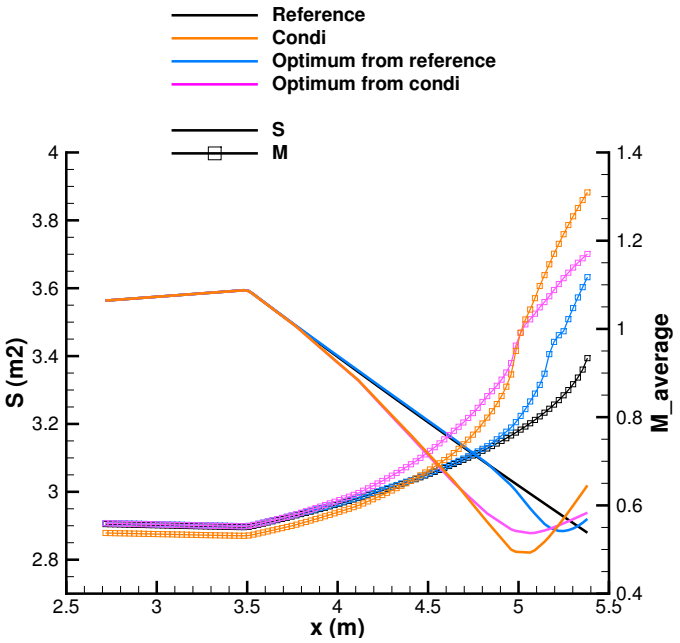

Figure V.10 – *Evolution of the area and the Mach number through nozzle shapes computed with an inviscid flow model*

have a similar throat area, as a result of the satisfied mass flow rate constraint. However, the resulting optimal configuration has different characteristics than the previous optimum obtained by starting from the reference (see Table V.4). The throat location at 88% of the nozzle length and the section ratio of 1.042 are similar to the starting convergent-divergent shape. Consequently, this indicates that the design space exploration performed by the algorithm remains local. Finally, the performance achieved by this shape is better than previous optimal performance.

Table V.4 – *Geometrical characteristics and performance of the nozzle configurations, evaluated with inviscid computations*

Configuration	Section ratio	Throat location (% of nozzle length)	Objective function J/J_{ref}	Constraint $\dot{m}/\dot{m}_{target}$
Isentropic theory	1.051	/	/	/
Reference	1.000	100	1.0000	0.9995
Convergent-divergent	1.051	86	1.1852	0.9738
Full domain research optimum (from reference)	1.012	95	0.9932	1.000
Full domain research optimum (from convergent-divergent)	1.042	88	0.9878	1.000

With the same optimization problem, it appears that a modification of the starting point leads the descent algorithm to a different optimum. This suggests the existence of multiple local optima in the design space, although the dimension of this space is relatively low compared to industrial problems with hundreds of degrees of freedom. At

this point, one can wonder if the proposed approach, based on a convex combination parameterization, is capable of reducing the number of local optima in the exploration space.

V.4 Assessment of the convex combination method on the axisymmetric nozzle with inviscid computations

V.4.1 Integration of convex combination into the optimization chain

In order to implement the convex combination method in the optimization workflow, an additional step is integrated between the optimizer and the analysis chain (see Fig. V.11). This step applies a Python code, that executes the convex combination of expert configurations parameters and generates the set of mesh deformation parameters.

The combination parameters λ are managed by the optimizer. They are defined such that they belong to the interval $[0, 1]$. Concerning the "convex" constraint, $\sum_i \lambda_i = 1$, two possible implementations are considered. First, the optimizer can be replaced by an in-house Python code, which would only generate sets of parameters satisfying this condition. At first sight, this may appear as the simplest solution, but it implies the development, implementation and validation of a dedicated feasible descent algorithm. The second possibility is to keep the Dakota software [1] as optimizer. In this case, the convex constraint has to be imposed as an optimization constraint. The advantage of this approach is that the minimization and the constraint management are done with efficient and validated optimizer and algorithms. However, the main drawback is that the additional "convex" constraint only guarantees the feasibility of the optimal shape, after convergence is reached. Due to the complexity of developing an efficient optimizer and personal know-how on the Dakota software, the latter solution is chosen for this study.

Consequently, two constraints are managed by the optimizer, concerning the mass flow rate and the combination coefficients. This implies that the configurations generated during the iterations of the feasible descent algorithm will not necessarily satisfy both constraints. This can initially be considered as a drawback of this optimization formulation. Nevertheless, the possibility to go beyond these constraints can also be beneficial for the exploration of the space defined with the convex combination approach. It gives some freedom to the algorithm, because a constraint can be temporarily ignored e. g. in order to further improve performance.

V.4.2 Choice of expert configurations

Convex combination can be applied with 3 to 10 expert configurations approximately. Their choice depends on:

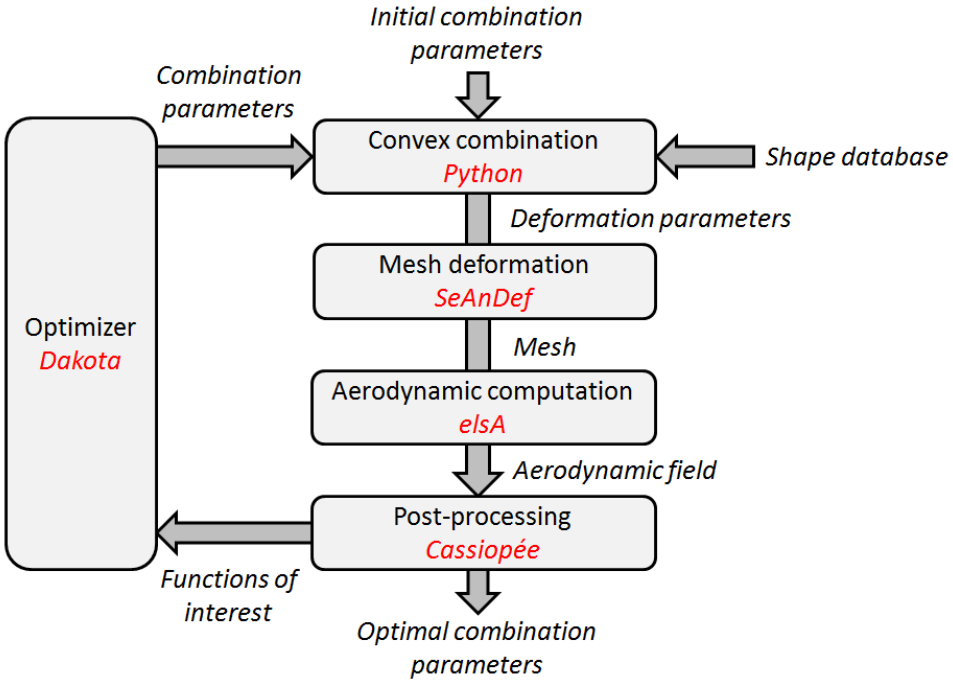

Figure V.11 – *Optimization workflow architecture, when comprising the convex combination*

- The directions of interest that the designer wants to explore with the optimization
- Previous optimization results
- A compromise between complexity and computational cost

When the sensitivities are computed using finite-differences, the cost of the gradient computation is proportional to the number of expert configurations.

For this first assessment of the method, only three shapes are considered in the database for combination. Due to the expectations of the isentropic one-dimensional computation (V.2) and the first optimization results (V.3), these three "expert configurations" are defined as convergent-divergent. Their geometrical characteristics are detailed in Table V.5, and the area evolution in these nozzles can be observed on Fig. V.12. Two have a section ratio of 1.051 as given by the isentropic nozzle theory. The third is inspired from the optimal shape obtained on the entire design space and has larger throat, i.e. a smaller section ratio. The axial position of the throat is also expected to have a significant effect on the performance. Hence, two throat positions are defined: upstream at 73% of the nozzle length and downstream at 86%.

It must be noted that these expert configurations have different throat areas. For sonic flows, the throat area drives the value of the mass flow rate. Thus, the three configurations do not have a mass flow value of $\dot{m}_{target}$; they do not verify the mass flow constraint.

Finally, although these nozzle shapes have only been designed for their interesting geometrical characteristics, their performance is evaluated. It appears that all of them have a lower performance than the reference nozzle.

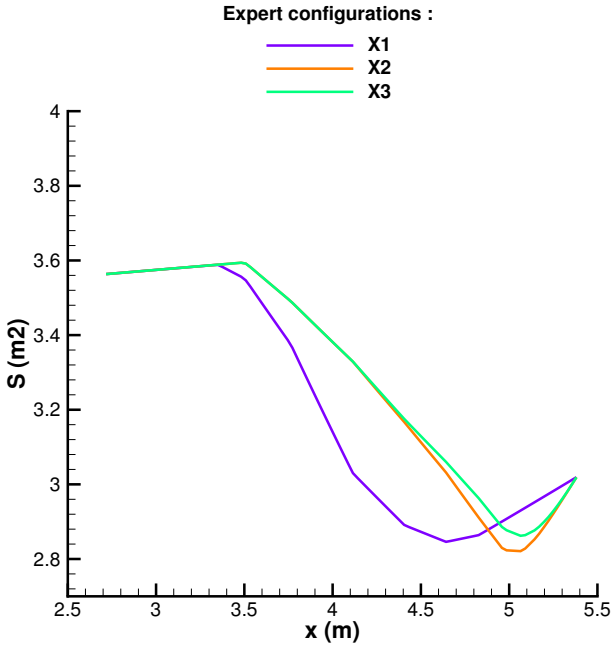

Figure V.12 – *Evolution of the area through nozzle shapes defined as "expert" configurations*

Table V.5 – *Geometrical characteristics and performance of the nozzle configurations, evaluated with inviscid computations*

Configuration	Section ratio	Throat location (% of nozzle length)	Objective function J/J_{ref}	Constraint $\dot{m}/\dot{m}_{target}$
Isentropic theory	1.051	/	/	/
Reference	1.000	100	1.0000	0.9995
Full domain research optimum	1.012	95	0.9932	1.0005
Expert shape X_1	1.051	73	1.0441	0.9887
Expert shape X_2	1.051	86	1.1852	0.9738
Expert shape X_3	1.044	86	1.0517	0.9940

V.4.3 Optimizations with Euler computations

The optimizer performs a feasible descent algorithm on the convex space generated with the expert configurations. Starting from the barycenter at $\Lambda = \{0.333, 0.333, 0.333\}$, it converges after 10 gradient iterations and 66 evaluations.

The resulting optimal shape is obtained for the set of combination coefficients $\Lambda = \{0.814, 0.008, 0.178\}$ and can be observed on Fig. V.13. It is a convergent-divergent shape, with a sonic throat located at 76% of the nozzle length, close to the most upstream throat position defined on the expert shapes. The Mach number evolution shows that this nozzle allows a progressive acceleration up to the exhaust. The area ratio is 1.048, which is larger than on the optimal nozzles found in V.3 by exploring the full design space. However, this effect is mainly due to the expert configurations, chosen with a wide exhaust area. Moreover, the optimal shape verifies the mass flow

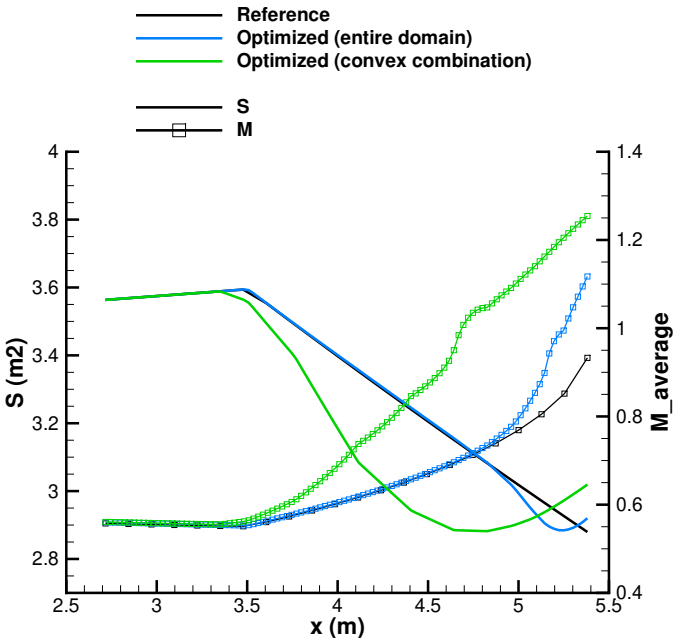

Figure V.13 – *Evolution of the area and the Mach number through reference and optimal nozzle shapes (inviscid case). All shapes verify the mass flow constraint.*

constraint with $\dot{m} \approx \dot{m}_{target}$ to within 10^{-3}, in contrast with the expert configurations. This demonstrates the capability of the proposed method to reach shapes that validate the constraint, even by combining configurations that do not.

Finally, this configuration shows better performance in comparison with the previous optima (see Table V.6). As the three optimal shapes belong to the design space of dimension 7, this suggests again the presence of local minima. In this case, the research of a global optimum on the full design space could be considered, due to the small number of design variables (7) and the two-dimensional flow computations. However, for targeted high-dimensional applications with costly CFD simulations, the use of global methods is irrelevant. In this context, it appears that the convex combination method can enable to find a better optimal solution than local exploration of the full design space. Thereby, it confirms the interest of using a method that includes "expert" knowledge.

V.5 Implementation of a DOE on the reduced design space

V.5.1 DOE and seeding methods

In order to have a full understanding of the exploration performed on the domain defined with convex combination, numerical designs of experiments are carried on. The cost of such methods is prohibitive in large dimensions. Thus, it is made possible by the reduction of the search space dimension associated to convex combination.

When the convex space is generated with three expert configurations, it can be

Table V.6 – *Geometrical characteristics and performance of the nozzle configurations, evaluated with inviscid computations*

Configuration	Section ratio	Throat location (% of nozzle length)	Objective function J/J_{ref}	Constraint $\dot{m}/\dot{m}_{target}$
Isentropic theory	1.051	/	/	/
Reference	1.000	100	1.0000	0.9995
Full domain research optimum (from reference)	1.012	95	0.9932	1.000
Full domain research optimum (from convergent-divergent)	1.042	88	0.9878	1.000
Expert shape X_1	1.051	73	1.0441	0.9887
Expert shape X_2	1.051	86	1.1852	0.9738
Expert shape X_3	1.044	86	1.0517	0.9940
Convex combination starting point	1.051	85	1.0314	0.9953
Convex combination optimum	1.048	76	0.9775	1.0015

represented as a triangular surface, with the vertices of the triangle being the reference shapes. An uniform seeding of this space is generated with Wootton, Sergent Phan-Tan-Luu's (WSP) algorithm [69], and leads to the sampling depicted in Fig. V.14.

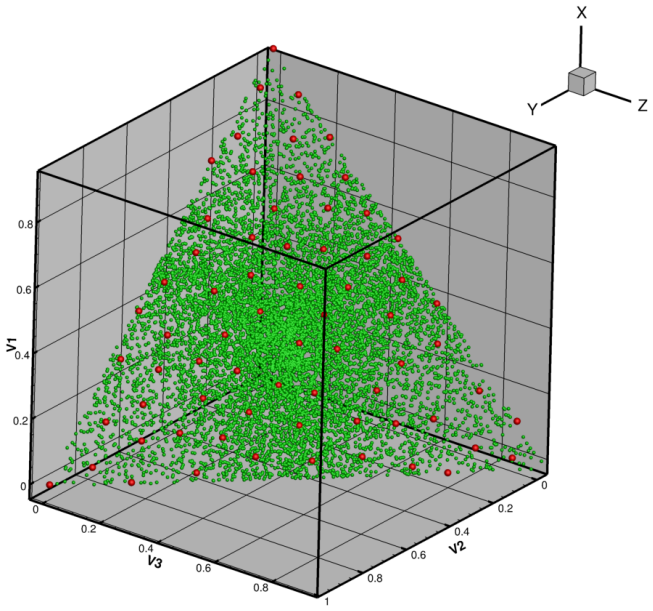

Figure V.14 – *Initial samples (in green) and distribution sorted by WSP algorithm (in red)*

V.5.2 Application to nozzle performance and response surface interpolation

Several parameters have been tested for the WSP algorithm, but finally a set of 68 samples has been selected. These designs are evaluated through the workflow and give a discrete representation of the functions of interest.

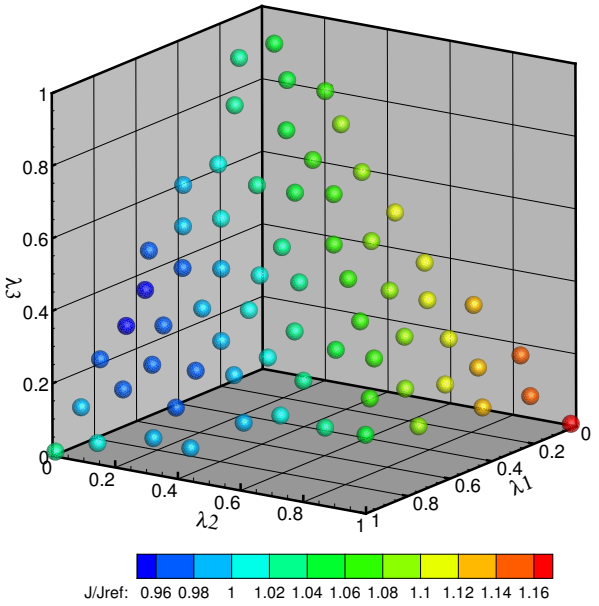

(a)

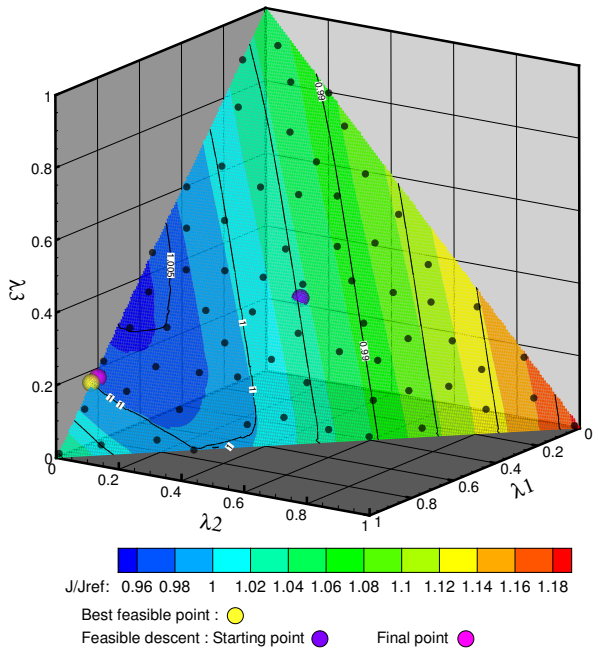

(b)

Figure V.15 – *Set of points (a) and interpolated response surface (b) obtained with a numerical DOE on inviscid computations*

The post-processed values are then interpolated on a response surface with a Krig-

ing method [77] and plotted as a continuous response surface. The objective function map and the constraint isocontours on the reduced search space are depicted in Fig. V.15(b). This interpolated response surface shows the correlation between the mass flow constraint and the objective function: the constraint isolines are strongly related to the objective function levels. This also enables to check *a posteriori* if the solution found with feasible descent algorithm is in agreement with the response map. According to the map, the best feasible solution is obtained with $\Lambda = \{0.833, 0.000, 0.167\}$. These coordinates appear to be close to the coordinates of the optimal solution reached with gradient-based methods. Moreover, the second combination coefficient is null, as observed on the resulting optimal combination of the algorithm. Therefore, this validates the capability of the gradient-based algorithm to explore the reduced search space under constraint.

V.6 Optimization of the performance of the nozzle in viscous flow, using feasible descent on the entire design space

Fluid viscosity affects the flow in the near-wall region and mixing layers, both of which are important parts of nozzle aerodynamics. As a consequence, viscosity can have a significant influence on nozzle performance and should not be neglected for design. To take this phenomenon into account, the inviscid flow model is replaced by RANS flow computations. The objective function comprises viscous stresses accordingly and all the terms of Eq. V.8 are considered non-zero.

As with inviscid computations, the first optimization is launched on the full design space of dimension 7. Starting from the reference shape, the feasible descent algorithm converges after 5 gradient iterations, totalizing 64 evaluations.

The area and Mach number evolution through the resulting optimal shape are depicted in Fig. V.16 (blue). It appears that the nozzle cross-sectional area is widely opened along the nozzle and reduced at the exhaust, presumably in order to respect the mass flow criterion. This shape enables a reduction of the wall friction and a good conservation of total pressure along the nozzle, which explains the gain in performance predicted by the optimizer (see Table V.7). However, it also appears counter-intuitive regarding expert knowledge for several reasons. First of all, the nozzle is not convergent-divergent, on the contrary of nozzle theory prediction and inviscid optimization results. Then, a closer look to the design parameters shows that they mostly converge towards the lower boundary of their definition interval. This explains the strong deformation of the shape, and denotes an unexpected behavior of the optimizer. In addition, the obtained nozzle geometry has irregularities between $x = 3.5\ m$ and $x = 4.5\ m$, that can lead to poor quality flows (and flow separation in the worst case), which are highly unlikely to be favorable to nozzle performance.

This situation could be due to several reasons, including without being exhaustive:

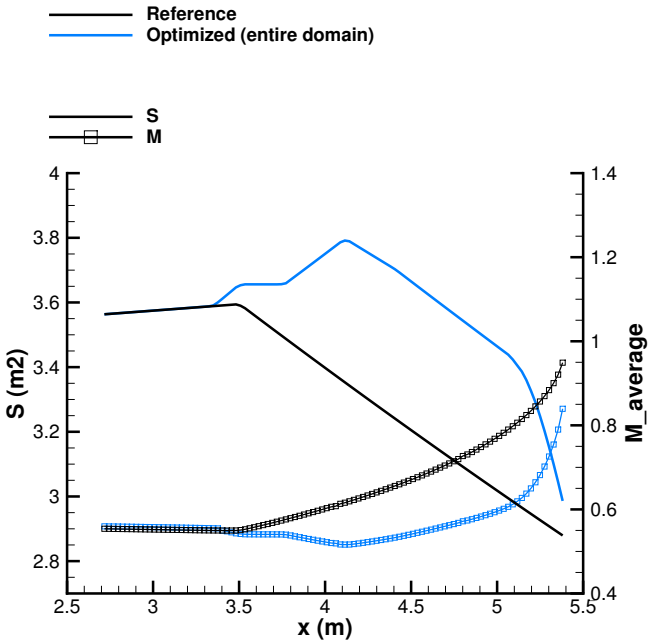

Figure V.16 – *Evolution of the area and the Mach number through nozzle shapes computed with a viscous flow model*

- an optimization problem that is not well defined to reflect the improvement expected by the designer
- an inappropriate (too narrow or too large) variation range for the design variables
- an inaccuracy in nozzle performance prediction with RANS simulations

At this point, it remains unclear to the authors which of these aspects may be responsible for this behavior. As this case is mainly dedicated to method assessment, it has been chosen to follow expert intuition and to dismiss this optimal shape. In this situation, convex combination enables to perform optimization although the optimum found on the full design space is "unfeasible" from the designer's point of view. Moreover, it helps to correct his possible shortcomings in the optimization problem definition. By considering a well-chosen set of "expert" configurations, it excludes the direction of undesirable shapes and defines an "industrially" feasible design space.

Table V.7 – *Geometrical characteristics and performance of the nozzle configurations, evaluated with viscous computations*

Configuration	Section ratio	Throat location (% of nozzle length)	Objective function J/J_{ref}	Constraint $\dot{m}/\dot{m}_{target}$
Isentropic theory	1.051	/	/	/
Reference	1.000	100	1.0000	0.9997
Full domain research optimum	1.000	100	0.9598	1.0000

V.7 Application of the convex combination method to improve viscous performance of the axisymmetric nozzle

V.7.1 Convex combination with three "expert shapes"

In order to "remove" undesirable shapes from the nozzle design space, the shapes considered in V.4.2 are re-used for convex combination. The feasible descent algorithm starts again from the barycenter and converges after 11 gradient computations and 59 evaluations.

The optimal shape is obtained with $\Lambda = \{0.731, 0.000, 0.269\}$ and the nozzle area and Mach evolution can be observed on Fig. V.17 (green). This nozzle has a throat located at 79% of its length, with an area ratio of 1.044.

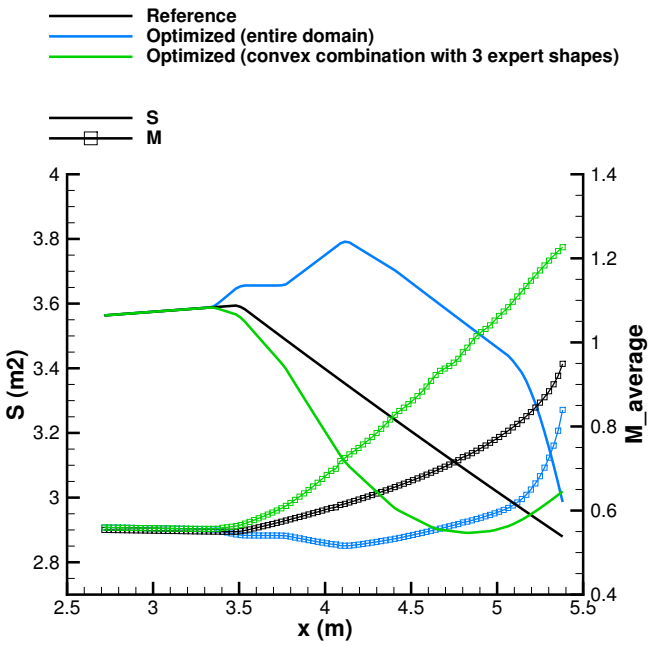

Figure V.17 – *Evolution of the area and the Mach number through nozzle shapes computed with a viscous flow model*

Compared to the optimum obtained with inviscid computations and convex combination in V.4.3, the throat appears to be located downstream (see characteristics in Table V.8). This position minimizes the losses due to wall friction, because it enables to keep a subsonic flow as long as possible. Therefore, it limits the higher wall friction induced by the supersonic flow in the divergent. Moreover, the throat area is larger than in the inviscid case. Since all "expert" configurations have the same exhaust area (as depicted in Fig. V.12), the section ratio is smaller on this case. This is an effect of the viscous boundary layer ; the reduced flow speed in the wall region implies that a greater throat area is needed to pass the mass flow rate $\dot{m}_{target}$.

Table V.8 indicates that the optimized shape on the reduced space achieves a significant gain on the objective function compared to the "expert" configurations. However,

this improvement is insufficient to reach a better performance than the reference nozzle. At this point, the DOE is expected to give information about how to continue the optimization process.

Table V.8 – *Geometrical characteristics and performance of the nozzle configurations, evaluated with viscous computations*

Configuration	Section ratio	Throat location (% of nozzle length)	Objective function J/J_{ref}	Constraint $\dot{m}/\dot{m}_{target}$
Isentropic theory	1.051	/	/	/
Reference	1.000	100	1.0000	0.9997
Full domain research optimum	1.000	100	0.9598	1.0000
Expert shape X_1	1.051	73	1.0900	0.9881
Expert shape X_2	1.051	86	1.1981	0.9716
Expert shape X_3	1.044	86	1.0830	0.9848
Convex combination starting point	1.051	85	1.0797	0.9914
Convex combination optimum	1.044	79	1.0047	1.0000

V.7.2 Numerical DOE

The DOE methods are applied to the viscous case. Since the three configurations used for combination remain the same, comparisons with inviscid flow are possible.

At first sight, the response map displayed on Fig.V.18 is similar to the inviscid case of Fig.V.15(b). However, the plotted objective function J is different, because of the additional viscous term in Eq.V.8. This term appears to have a "smoothing" effect on nozzle performance, but does not change the global trend of the response surface. In particular, the area of interest is located in the same zone of the map for both inviscid and viscous flows. Although viscosity modifies the objective function implicitly, it also affects the mass flow constraint. The location of the feasible-mass flow isoline ($\dot{m}/\dot{m}_{target} = 1$) has changed. Again, a strong correlation is observed between the constraint and the objective function.

According to the response map, the feasible design that minimizes J is found for $\Lambda = \{0.722, 0.003, 0.274\}$. These coordinates are similar to the coordinates obtained at convergence of the feasible descent algorithm, and confirm that the optimizer is able to converge in the vicinity of the global optimum of the subspace. This also indicates to the designer that the set of "expert" configurations is not sufficient to improve significantly the objective function. Consequently, an enrichment of the "expert database" is suggested to continue the optimization process.

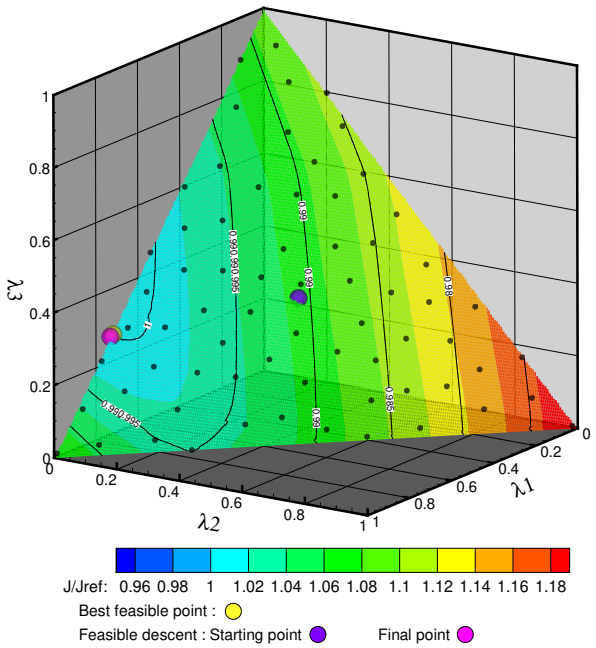

Figure V.18 – *Interpolated response surface obtained with a numerical DOE on RANS computations*

V.7.3 Convex combination with four "expert shapes"

A new configuration is added to the existing set of 3 configurations. In order to introduce a convergent nozzle, the reference shape is chosen as X_4.

Then, the feasible descent algorithm is launched on the space generated by the convex combination of these 4 configurations. The optimal shape found in V.7.1 is defined as starting point for the feasible descent.

After 2 gradient computations and a total of 39 evaluations, the algorithm returns an optimal set of coordinates $\Lambda = \{0.855, 0.000, 0.000, 0.145\}$. First of all, these coordinates indicate that the optimizer takes advantage of the newly introduced expert configuration. The resulting shape is a convergent-divergent nozzle, with a throat located at 73% of the nozzle length and an area ratio of 1.038 (see Table V.9).

The area and Mach number evolution in this nozzle are depicted in Fig.V.19 (red). The higher velocity along the nozzle implies that wall friction stresses are more important in this case than in the previous optimal nozzle. However, this effect is balanced by a favorable pressure resulting force in the divergent, that is extended. Thanks to this, the performance of the nozzle is improved in comparison with the reference and the optimum obtained with 3 configurations. In comparison with the optimum obtained in V.3 with full design space exploration, the improvement appears smaller. This is a possible consequence of the search on a subspace of the design space. However, in a context where the search of a global optimum is not affordable, the convex combination method has the advantage of generating an understood and well-defined optimal shape.

Table V.9 – *Geometrical characteristics and performance of the nozzle configurations, evaluated with viscous computations*

Configuration	Section ratio	Throat location (% of nozzle length)	Objective function J/J_{ref}	Constraint $\dot{m}/\dot{m}_{target}$
Isentropic theory	1.051	/	/	/
Reference (X_4)	1.000	100	1.0000	0.9997
Full domain research optimum	1.000	100	0.9598	1.0000
Expert shape X_1	1.051	73	1.0900	0.9881
Expert shape X_2	1.051	86	1.1981	0.9716
Expert shape X_3	1.044	86	1.0830	0.9848
Convex combination optimum (3 expert shapes)	1.044	79	1.0047	1.0000
Convex combination optimum (4 expert shapes)	1.038	73	0.9977	1.0000

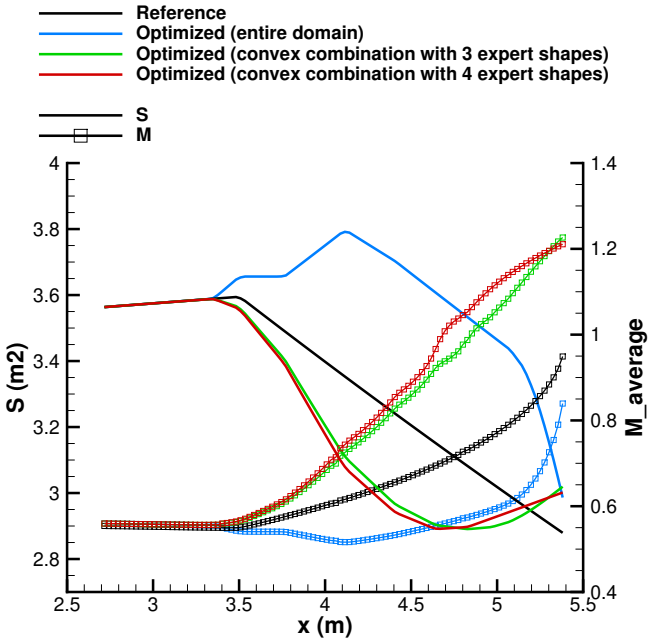

Figure V.19 – *Evolution of the area and the Mach number through nozzle shapes computed with a viscous flow model*

V.8 Physical analysis of the nozzle optimization problem

The work performed on the axisymmetric nozzle has focused on optimization processes and in order to perform numerical analyses, tolerances have been defined on the mass flow constraint. However, from a physical point of view, nozzles should only be compared at same mass flow rate. Consequently, discrepancies in the mass flow

rate values can alter the predicted performance level.

To compensate the mass flow differences and quantify the associated performance variations, a corrective term can be defined. This term is based on the sensitivity of the objective function with respect to the design constraint, that is computed from the gradients of the functions of interest. Consequently, an estimate of the corrected performance at same mass flow, called $J/Jref@m_{target}$, is computed for the optimized shapes and presented in Table. V.10. This table shows that a relative discrepancy of a magnitude 10^{-4} on the mass flow constraint has a considerable impact on the functions of interest. Therefore, it appears that small mass flow perturbations can significantly alter the predicted performance, in comparison with the improvements achieved with optimization. Again, this reveals the tight link between mass flow and thrust, which are the two values driving nozzle performance. Yet, this effect is even stronger than expected.

In order to consider this link and enable efficient optimizations, the *a posteriori* analysis of this work advocates for the use of objective functions integrating the mass flow constraint and penalizing the configurations that do not respect it.

Table V.10 – *Performances of the optimized nozzle shapes, including mass flow correction estimate*

	Configuration	Objective function J/J_{ref}	Constraint $\dot{m}/\dot{m}_{target}$	J/J_{ref} @ $\dot{m}_{target}$
Euler	Reference	1.0000	0.9995	1.0000
	Full domain research optimum	0.9932	1.0005	0.9995
	Convex combination optimum (3 expert shapes)	0.9775	1.0015	0.9880
RANS	Reference	1.0000	0.9997	1.0000
	Full domain research optimum	0.9598	1.000	0.9615
	Convex combination optimum (4 expert shapes)	0.9977	1.000	0.9994

V.9 Chapter summary

In this chapter, a first nozzle case has been developed for optimization. An optimization problem and workflow are proposed to improve the performance of a single-flow bi-dimensional nozzle. At first, some characteristics of the ideal nozzle have been predicted from a preliminary monodimensional and isentropic computation. Then, a first optimization has been performed on the complete design space of dimension 7 with a feasible descent method and inviscid flow computations. This validated the defined

workflow, and has returned convergent-divergent optimal shape in agreement with the isentropic theory. Moreover, changing the starting point of the descent has demonstrated that the optimal shape depends on it, which suggests the presence of local optima on the design space. At this point, the convex combination has been assessed on the nozzle case with inviscid computations. This approach has shown that a significant improvement is possible by taking into account expert knowledge. In addition, reducing the complexity of the search by a reduction of the dimension of the search space has permitted to find a more efficient shape than by exploring the full domain. Hence, the convex combination method can help reducing the risk of being captured by local minima, whose number increases with the dimension of the space, especially when involving a CAD environment and trigonometric manipulations. With three expert configurations, it also gives the opportunity to perform DOE and draw response surfaces for the quantities of interest. Introducing flow viscosity for flow simulations has lead the optimization on the full design space to a non-acceptable shape for industrial designers. In this case, convex combination with an adapted choice of expert configurations has enabled to perform optimization while remaining in an acceptable design space. After an optimization and a DOE, the first set of 3 expert configurations appeared insufficient to reach an optimum with significant performance improvements. Consequently, the expert database has been enriched with a new configuration, and thanks to this the optimizer has succeeded in finding a new optimal shape with improved efficiency.

After this first evaluation on a nozzle case of intermediate complexity, the convex combination seems ready to be applied on a case of industrial complexity, with a high number of design variables and a CAD software.

VI

Development of a CAD-based geometrical model of nacelle

Contents

The objective of this chapter is to develop a geometrical model of IPPS, based on a CAD-model driven by industrial design parameters.

First, a CAD model is described that enables to generate IPPS shapes comprising complex elements. This model generates geometrical shapes based on industrial design parameters and has been developed for the scope of this optimization work.

Then, the associated mesh generation process is presented. The meshing actions have been recorded and can be replayed for every new CAD geometry.

Next, the complete CAD and grid generation steps are automated for their integration in future optimization workflows.

Finally, the geometry and mesh generation process is tested with sets of parameters generated with convex combination. A DOE is operated to generate a first significant set of shapes.

VI.1 Development of a detailed CAD model of nacelle based on industrial design parameters

Prior to the thesis work, a CAD model has been developed for this project at Safran Aircraft Engines. This geometrical model, defined using the CATIA V5 software (property of Dassault Systèmes [14]), has been enriched and modified in the scope of this work. This model, depicted in Fig. VI.1(a), is a three-dimensional geometric representation of an IPPS with a turbofan engine and dual-separate-flow nozzles. It comprises the inlet, the outer nacelle, the core (primary) and fan (secondary) ducts and nozzles, as well as the pylon and the lower bifurcation located in the secondary flow. This model only considers non-rotating parts of the engine and three planes are defined at the interfaces with inner engine components. They are located upstream of the fan, downstream of the turbine in the core-flow, and downstream of the outlet guide-vane in the secondary flow. These planes will be later used to define boundary conditions for the flow solver.

The geometry of this model is generated from a table of parameters. These design variables enable a full parameterization of the IPPS shapes. Moreover, they correspond to geometrical parameters based on expert-knowledge and engineering know-how. These design parameters are defined to enable the generation of tridimensional nozzles and cowl shapes, with highly non-axisymmetrical characteristics. For instance, Fig. VI.1(b) illustrates the ability of the model to create highly deformed geometries of the rear-body. Consequently, a significant number of parameters is necessary and the model involves approximately 300 variables in total.

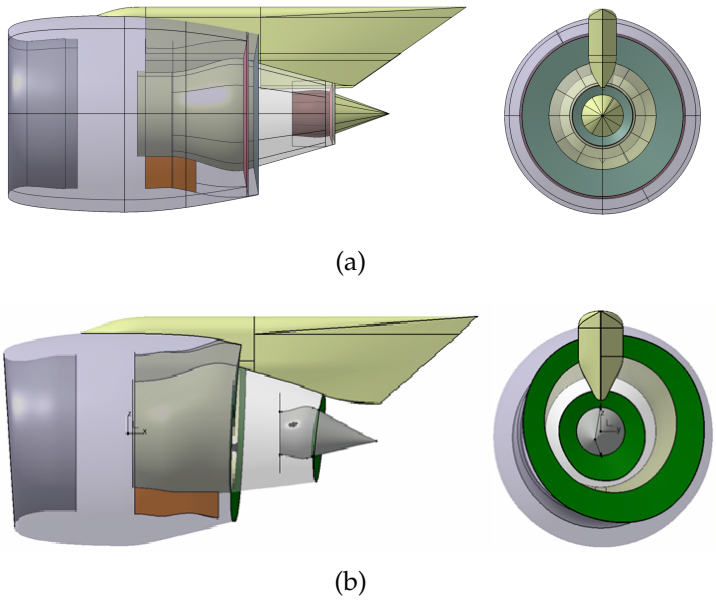

(a)

(b)

Figure VI.1 – *High-fidelity CAD model of the IPPS in standard (a) and highly deformed (b) cases*

Besides, this model integrates industrial design contraints. In particular, during the design phases of the rear-body shapes, the nozzles throat areas are fixed by the engine thermodynamic cycle. Consequently, they are defined as a design parameter of the CAD model and the generated geometries have to respect their value. The throat parameters are defined accordingly and can be adjusted in order to fit the area constraint.

Then, an internal loop based on a quick optimization process available in CATIA operates the adaptation and ensures that the area constraints are satisfied (with a precision under $10^{-7}\ m^2$). This enables to respect the geometrical throat areas given by thermodynamics for both primary and secondary nozzles, despite the non-axisymmetrical character of the generated shapes. The robustness of this process has been tested and validated on several highly-deformed geometries, such as the rear-body depicted in Fig. VI.1(b).

VI.2 Definition of a meshing strategy based on CAD geometries

The CAD model presented in VI.1 generates a set of surfaces, curves and points, that is loaded in the meshing software ICEM CFD (property of ANSYS [4]). Prior to the current thesis work, a meshing process has been defined at Safran Aircraft Engines following usual industrial procedures and recorded as a macro. After a change in the design parameters, the CAD model is updated and the macro is replayed to re-create the 3D mesh.

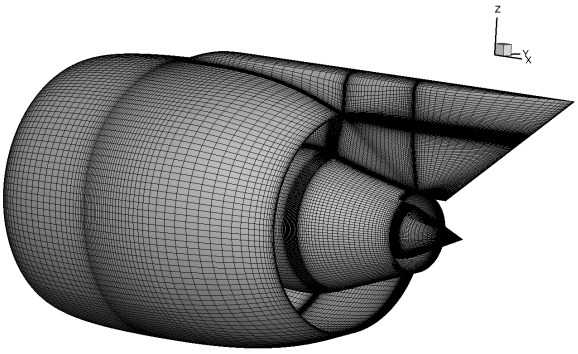

(a)

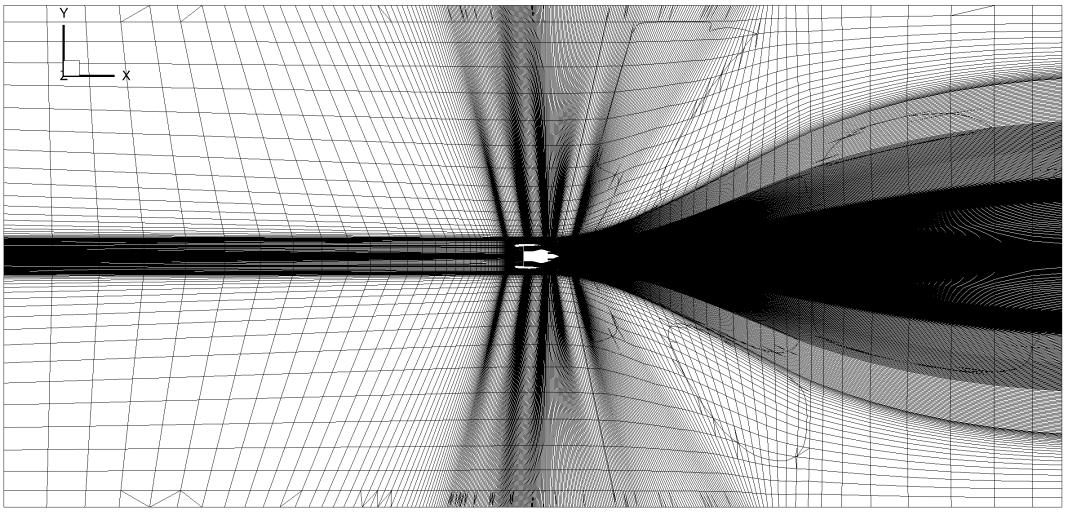

(b)

Figure VI.2 – *Overview of the surface grid (a) and of a slice of the volume mesh (b)*

The resulting mesh is a structured grid made of $15 \cdot 10^6$ cells. The near-wall region is refined for viscous computations, as well as the jet wake. Due to its number of cells, this grid is considered as coarse for final industrial applications. However, preliminary computations have shown that it enables relatively fast grid generation (around 15 minutes) and flow computation (approximately 30 minutes on 280 CPU cores), while being sufficiently accurate to evaluate nacelle aerodynamics with the precision needed for optimization.

The mesh is depicted in the surface of the IPPS (Fig. VI.2(a)) and a slice of the volume mesh can be seen on Fig. VI.2(b).

VI.3 Automation of CAD and mesh generation steps

The complete process, from the table of parameters up to the generated mesh file, is represented on Fig. VI.3. Dedicated scripts are written in order to automate the geometry and mesh generation.

First, a script file is developed to manage the steps operated with the CATIA software. This script reads the table of parameters and updates the geometrical model accordingly. Then, it launches the internal optimization loop, to adapt the parameters of the nozzle ducts and satisfy area constraints. Finally, it exports the geometrical files from the CAD model.

Then, another script is developed to launch ICEM in batch mode and execute the mesh replay macro. This macro loads the geometrical files from CAD, operates the grid generation steps, and exports the mesh file. Finally, an additional script is implemented to evaluate the mesh quality.

All of these scripts enable to have a fully-automated generation process of the CAD and mesh. However, this type of processes based on industrial design tools usually suffers from robustness issues, in particular when large variations of the design variables are allowed. Consequently, the robustness of the generation process in association with the convex combination approach is assessed in the following.

VI.4 Assessment of convex combination method on a CAD-based design process

The capability of the design process to create acceptable designs and associated meshes is now tested with convex combination. First, a set of shapes is generated to compose the database for combination. Then, a DOE is performed on a convex combination space, in order to assess the capability of the approach to handle industrial geometries and meshes.

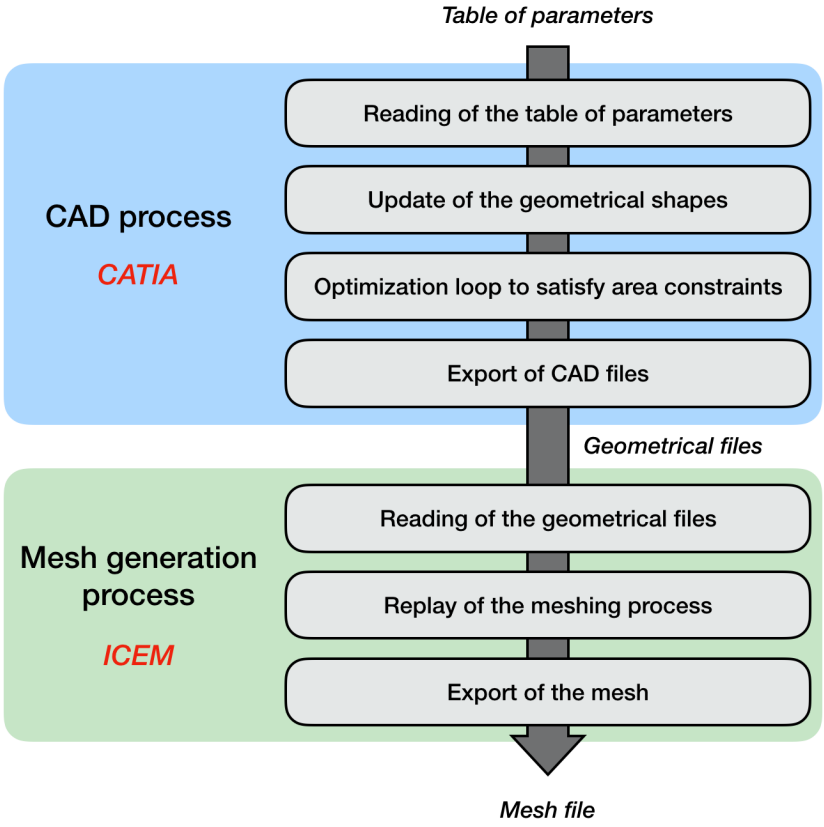

Figure VI.3 – *Schematic view of the geometric and mesh generation process*

VI.4.1 Definition of "expert" configurations and database

Prior to the definition of "expert" shapes, a first nacelle is generated with the CAD model and defined as reference. It comprises an axisymmetric inlet, with a generic lip shape. The nozzle and cowls of the primary and secondary flows are defined as axisymmetric. Only the internal bifurcations and the pylon alter the axial symmetry of the IPPS. This nacelle, depicted in Fig. VI.4(a) is an industrially acceptable UHBR baseline configuration. Still, it has not been optimized and is not representative of efficient shapes obtained at the end of an industrial design process. Thus, it has some potential for improvement and is a good reference point for optimization.

Then, a first database of CAD shapes is generated for convex combination. The purpose of this database is to assess the approach and illustrate the possibilities of the combination. From the baseline configuration, three nacelle shapes are defined for the "expert" database. These shapes have been generated with particular rear-body characteristics. For this first assessment, the chosen shapes focus on the geometry of the secondary nozzle. Consequently, only the shape parameters of the fan nozzle are altered and the ones defining the primary nozzle are common to all shapes. The first shape in the database, X_1 (Fig. VI.4(b)), comprises a vertically ovalized nozzle. This shape introduces a non-axisymmetrical shape, that could benefit to the three-dimensional geometry. The second one, X_2, has an extended secondary flow nozzle compared to the reference (Fig. VI.4(c)). On the contrary, the nozzle is shortened on the third geometry, X_3 (Fig. VI.4(d)). The two latter are based on axisymmetrical cowl geometries, in contrast to the first one. Although they may appear exaggerated at first sight, these

nozzles are expected to define a subspace enabling a great variety of designs.

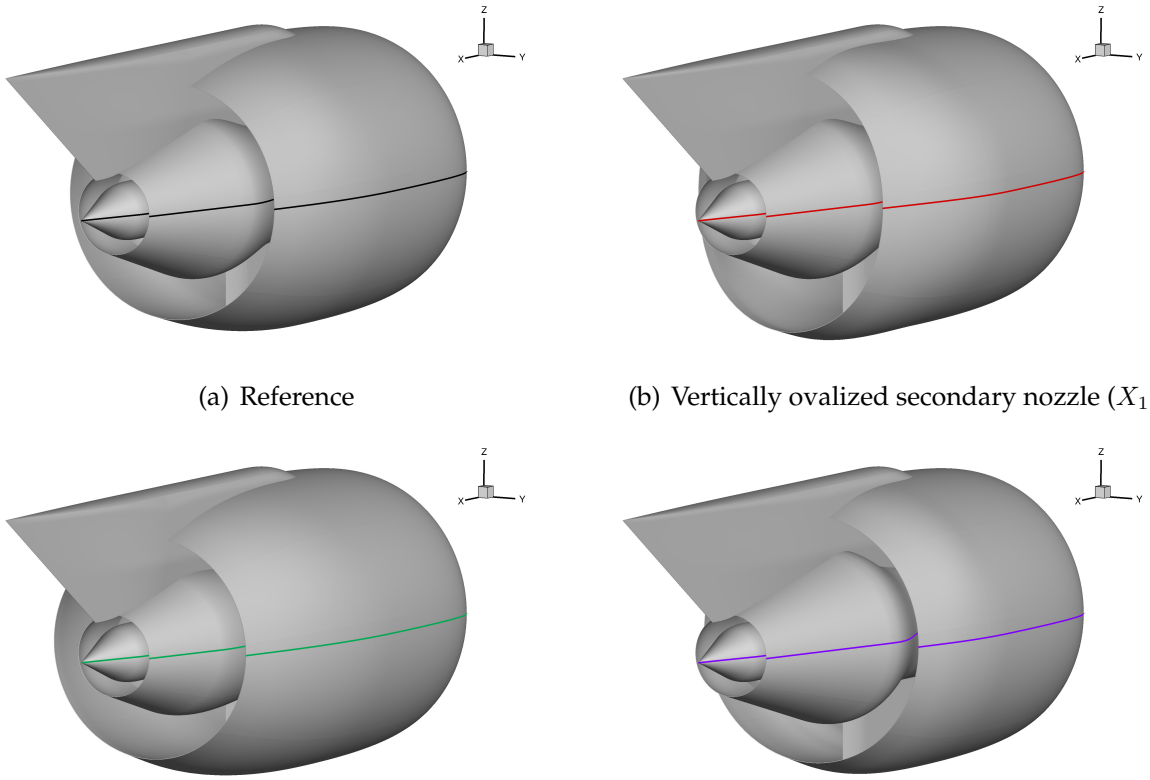

(a) Reference (b) Vertically ovalized secondary nozzle (X_1)

(c) Extended secondary nozzle (X_2) (d) Shortened secondary nozzle (X_3)

Figure VI.4 – *Reference rear-body shape and "expert" configurations in the database for combination*

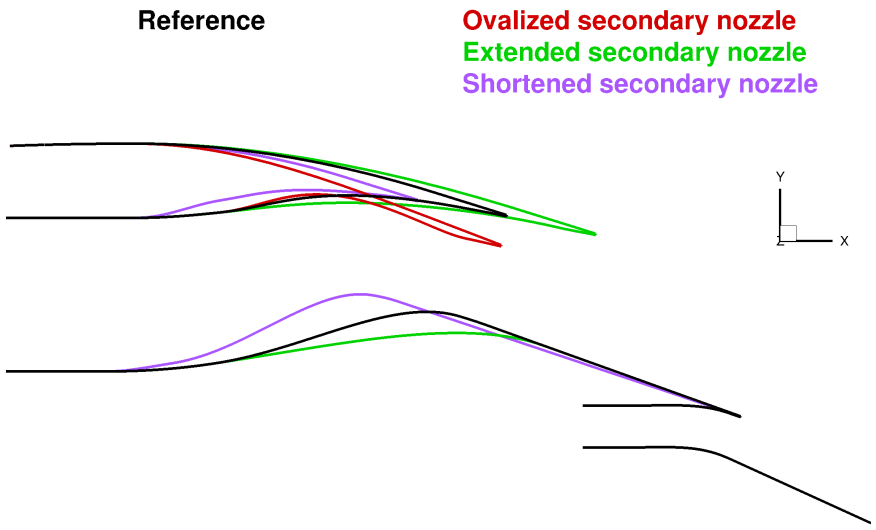

Figure VI.5 – *Comparison of the nozzle geometries in a slice*

VI.4.2 Design of experiments for CAD and mesh shapes

At this point, the relevance of the convex combination method to generate CAD geometries and associated mesh is assessed with a design of experiments. The automated

geometry generation process defined in VI.3 is applied. The database considered for combination comprises only three shapes, that is why the sampling defined in V.5 can be re-used in this case. Consequently, 68 geometries are generated in the subspace, in order to evaluate the behavior of the geometrical process.

First of all, it appears that all but one geometries are succesfully generated over the defined design space, as depicted in Fig. VI.6. The only shape that returned an error encountered a surface generation issue in the CAD software. For complex geometrical models with hundreds of variables, such errors are common and must be corrected afterwards. However, the great number of successful geometry and mesh generations suggest that using convex combination to manage the design variables introduces smoothness and limits the appearance of this type of errors.

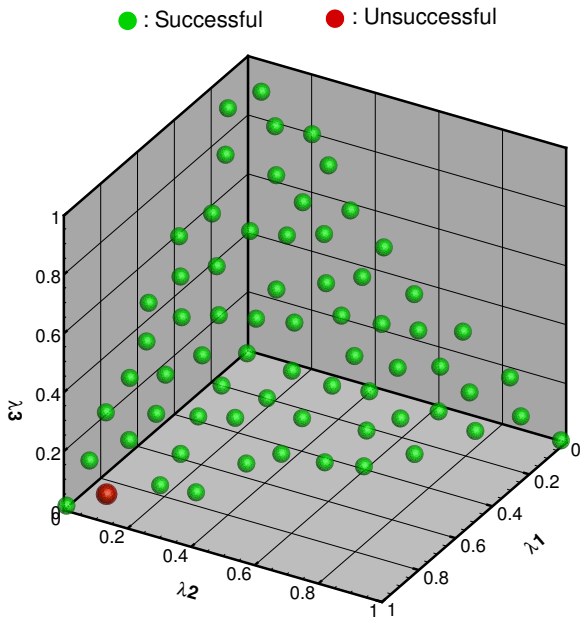

Figure VI.6 – *Overview of the successful geometry generations over the subspace*

Then, the obtained shapes are studied ; as expected, they represent a continuous "morphing" between the geometries of the database. Consequently, depending on the coefficients, they inherit of the "expert" shapes characteristics on the secondary nozzle. Remarkable examples can be observed on Fig. VI.7, that mix the ovalized shape with extended or shortened nozzle length.

In conclusion, the CAD-based geometrical workflow is considered robust enough when controlled by sets of parameters coming from combination. The DOE, with a first shape database focused on secondary nozzle geometry, confirmed that the regularity implied by this approach enables the geometrical generation of most shapes in the subspace.

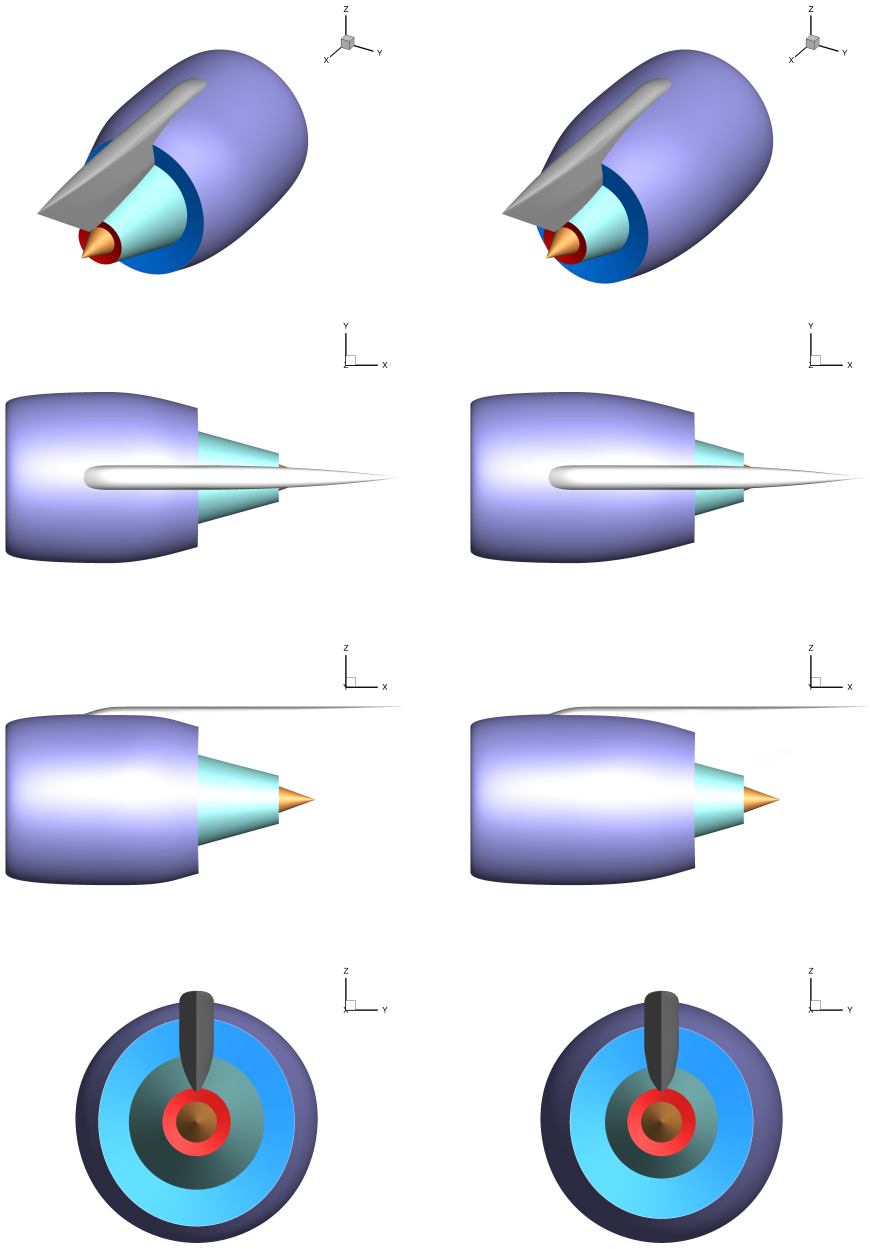

(a) $\Lambda = \{0.389, 0.009, 0.602\}$ (b) $\Lambda = \{0.289, 0.691, 0.021\}$

Figure VI.7 – *Examples of geometries generated with the DOE*

VI.5 Chapter summary

To sum up, a CAD model of a complete IPPS has been developed. This geometric model, based on hundreds of design parameters, is of industrial complexity and enables large modifications for optimization. Using the output CAD geometry, an associated mesh generation process has been recorded and re-played to create the mesh required for aerodynamic flow computations. This complete process has been automated, in order to be operated in a design or optimization workflow. Then, the robustness of the complete geometry generation process has been assessed with convex combination and a DOE. Using a first shape database, it appeared that the sets

of parameters generated with convex combination lead to consistent CAD shapes and meshes for most cases. Therefore, this process can be integrated in a larger workflow comprising CFD simulations and applied for first CAD-based optimizations.

VII

CAD-based optimizations of isolated turbofan nozzles

Contents

The objective of this chapter is to apply the convex combination to a case of industrial turbofan nozzles, on an isolated engine configuration.

The study case is defined from a target aircraft, and an associated engine is developed, corresponding to future configurations. An optimization workflow is developed with an adapted formulation for improving the performance of an isolated nacelle.

First optimizations revealed robustness issues on the geometrical models. They are discussed, and the technical solutions adopted to overcome these difficulties are presented.

Then, optimizations are performed, based on the convex combination approach with a database of three shapes. The performance of a first resulting optimal shape is discussed and interpreted. Based on the coefficients of the optimal combination, the shape database is modified and the process re-launched. Next, the two optimal shapes are compared, in particular with a detailed breakdown of surface force contributions. Finally, a DOE is performed on the subspace defined with the convex combination method, in order to identify its areas of interest and potential local optima.

VII.1 Development of an optimization problem and workflow to improve the performance of turbofan nozzles

VII.1.1 Case setup and aircraft/engine configuration

This study aims at performing shape optimizations on the nozzles and the rear-body cowls of a turbofan engine. In order to be representative of an industrial design process, a target aircraft configuration is defined. The NOVA civil aircraft concept designed at ONERA [89] is considered. Among the different NOVA configurations available, the one with under-wing-mounted engines, depicted in Fig. VII.1, is considered as test case for this study. The initial NOVA UHBR engines are replaced by an IPPS generated with the geometrical process described in VI. The properties of the new engine configuration, presented in Table VII.1, are consistent with the aircraft characteristics.

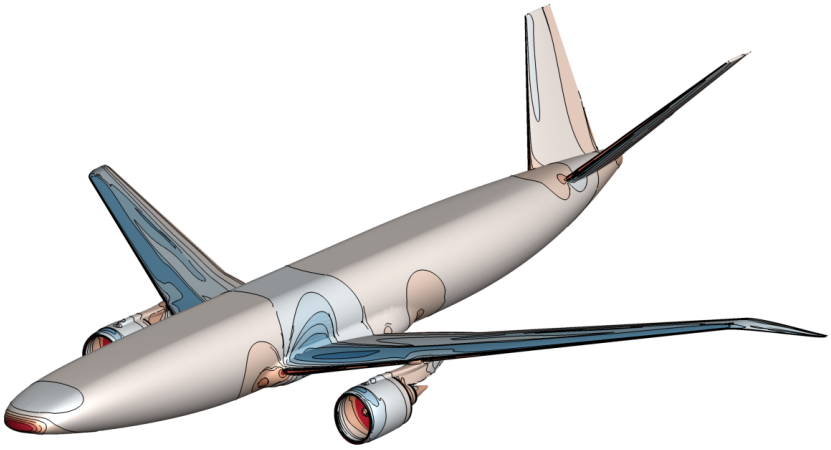

Figure VII.1 – *"Baseline" configuration of the NOVA aircraft ©ONERA*

Table VII.1 – *Flight conditions and turbofan characteristics for the NOVA baseline aircraft configuration*

Cruise flight conditions	
Cruise Mach number	0.82
Cruise altitude	37,000 ft / 11,278 m

Engine characteristics	
Fan diameter	85 in / 2.16 m
Fan Pressure Ratio	1.3
Bypass Ratio	16
Sea Level Static Thrust	23,800 lbf / 105,860 N

For first optimizations with the convex combination method and CAD design tools, the aircraft geometry is not taken into account and an isolated engine configuration is considered. Consequently, the resulting drag on the aircraft without IPPS and pylon (sometimes called "glider" or "airframe") is supposed invariant for drag-thrust balance.

VII.1.2 Operating conditions of the engine

In this work, simulations of the IPPS are performed in cruise flight conditions, at an altitude of 37,000 ft and a Mach number of 0.82. As a first approximation, the angle of attack seen by the engine is chosen at 0°. A methodology is defined in order to determine the operating conditions of the engine and the boundary conditions for aerodynamic simulations.

In practice, the operating point of the engine can only be determined precisely through an iterative coupling process. The engine propulsive cycle gives flow conditions for the aerodynamic computations and the aerodynamic performance allows in return to adjust the operating point of the cycle. Thus, it appears that a thermodynamic representation of the engine is necessary to perform precise aerodynamic simulations of the nozzles.

Consequently, a thermodynamic model of the engine has been developed at Safran Aircraft Engines using the PROOSIS software (property of Empresarios Agrupados [17]). This state-of-the-art model takes into account all engine components and is similar to industrial tools used for turbofan cycle prediction. Moreover, it is sized and adapted to describe the flight phases of the NOVA aircraft configuration [89], in agreement with industrial practices. In the end, it is exported as an executable file. In particular, the model is developed in order to be coupled with aerodynamic simulations. Therefore, it takes post-processed values from aerodynamic computations, geometrical characteristics and a throttle command as inputs and returns quantities to impose on the boundary conditions of the computations.

In cruise, i.e. at constant speed, the aircraft satisfies a mechanical equilibrium that can be written, when projected on the engine axis:

$$F_{IPPS} + D_{airframe} = 0 \tag{VII.1}$$

where F_{IPPS} is the resulting force on the complete power plant comprising the pylon, and $D_{airframe}$ is the drag associated to the airframe. The airframe drag term indicated by Wiart et al. [89] for the NOVA configuration is assumed to be unchanged in the engine reference frame. Thus, the associated non-dimensional drag coefficient in cruise is $CD_{airframe} = 266.2 \cdot 10^{-4}$.

Then, the nacelle reference shape, developed in VI.4.1 and depicted in Fig. VI.4, is used with this engine configuration. Preliminary CFD simulations are performed on this geometry and a first guess of the operating conditions is made. Then, by iterating "manually", the operating conditions of the engine are adjusted until the mechanical equilibrium is verified. The resulting set of operating conditions is presented in Table VII.2.

VII.1.3 Formulation of the optimization problem

This work aims at improving the efficiency of the IPPS, comprising the engine, its nacelle and the pylon. In cruise conditions, this objective can be considered as lowering

Table VII.2 – *Operating conditions of the reference engine in cruise flight*

Inlet plane		**Primary nozzle**		**Secondary nozzle**	
$\left(\frac{p}{p_\infty}\right)_{fan}$	1.248	$\left(\frac{p_i}{p_\infty}\right)_{inj\ prim}$	1.748	$\left(\frac{p_i}{p_\infty}\right)_{inj\ sec}$	2.034
		$\left(\frac{T_i}{T_\infty}\right)_{inj\ prim}$	3.065	$\left(\frac{T_i}{T_\infty}\right)_{inj\ sec}$	1.244

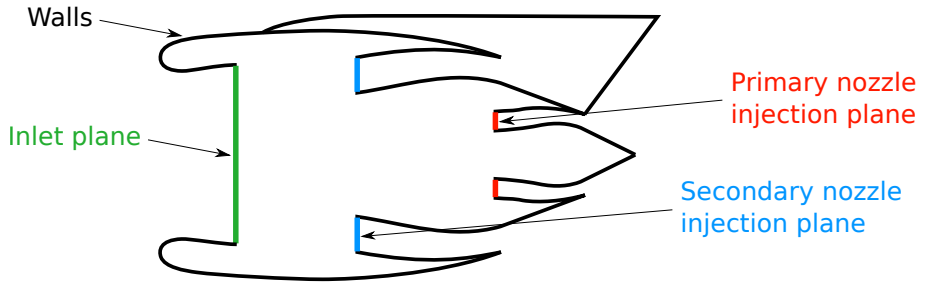

Figure VII.2 – *Schematized view of the boundary conditions for nacelle aerodynamic simulations*

the fuel consumption while delivering thrust for the propulsion of the aircraft. For this first optimization case on an UHBR engine, the nacelle is isolated and no coupling is considered between aerodynamic computations and the thermodynamic propulsive model. In practice, this leads to fixed boundary conditions for CFD simulations. Consequently, an adapted formulation of the optimization problem is defined. Especially, maximizing thrust for given engine operating conditions is expected to improve significantly the engine efficiency.

The resulting force on the power plant is evaluated from aerodynamic computations. This force is obtained by summing the net thrust delivered by the engine, F_{net}, and a drag term $D_{external}$. First, net thrust is computed with a momentum balance in a streamtube extending from an infinite upstream plane up to the engine rear-body. This is done by integrating the forces on the exhaust planes of the engine, the rear cowls and the pylon surface licked by the engine flow, and substracting the inflow momentum in a plane located at the infinite upstream (see the surfaces in orange on Fig VII.3):

$$F_{net} = F_{primary} + F_{secondary} + F_{plug} + F_{cowl} + F_{pylon\,licked} - F_\infty$$

$$\begin{aligned}
\text{with:}\quad F_{primary} &= \int_{S_{primary}} \left[\rho\vec{V}(\vec{V}.\vec{n}) + (p-p_\infty)\vec{n}\right].\vec{x}dS \\
F_{secondary} &= \int_{S_{secondary}} \left[\rho\vec{V}(\vec{V}.\vec{n}) + (p-p_\infty)\vec{n}\right].\vec{x}dS \\
F_{plug} &= \int_{S_{plug}} \left[\overline{\overline{\sigma}}.\vec{n}\right].\vec{x}dS \\
F_{cowl} &= \int_{S_{cowl}} \left[\overline{\overline{\sigma}}.\vec{n}\right].\vec{x}dS \\
F_{pylon\,licked} &= \int_{S_{pylon\,licked}} \left[\overline{\overline{\sigma}}.\vec{n}\right].\vec{x}dS \\
F_\infty &= \int_{S_\infty} \left[\rho\vec{V}(\vec{V}.\vec{n})\right].\vec{x}dS
\end{aligned} \qquad \text{(VII.2)}$$

where $\overline{\overline{\sigma}}$ is the sum of the pressure and viscous stresses $\overline{\overline{\sigma}} = -p\overline{\overline{I}} + \overline{\overline{\tau}}$. Then, the external drag is defined as the integrated forces on the external nacelle cowl and the pylon that is not licked by the engine flow (depicted in blue on Fig VII.3):

$$D_{external} = \int_{S_{external} \cup S_{pylon\ external}} [\overline{\overline{\sigma}}.\vec{n}]\ .\vec{x} dS \tag{VII.3}$$

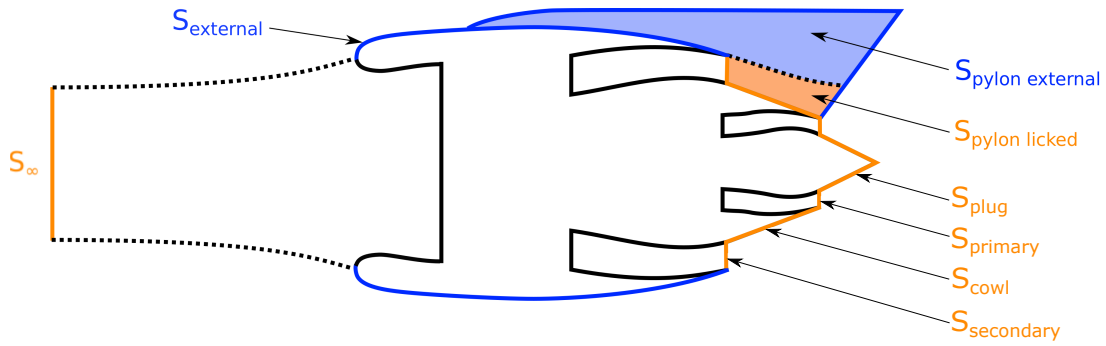

Figure VII.3 – *Schematized view of the integration surfaces contributing to the resulting force on the IPPS*

In parallel, an ideal force F_{ideal} is defined, based on the flow quantities injected in the nozzle planes. This term is computed by supposing that the flow is expanded isentropically until the infinite upstream (or downstream) pressure p_∞. Using the isentropic relation for pressure (Eq. V.2), an ideal Mach number can be determined at the exhaust:

$$M_{ideal} = \left(\frac{2}{\gamma - 1} \left[\left(\frac{p_\infty}{p_{i\ inj}} \right)^{\frac{1-\gamma}{\gamma}} - 1 \right] \right)^{\frac{1}{2}} \tag{VII.4}$$

Then, the isentropic temperature relation (Eq. V.3) allows to define an ideal exhaust temperature T_{ideal}. Thus, the ideal exhaust velocity is:

$$V_{ideal} = M_{ideal} \sqrt{\gamma r T_{ideal}} \tag{VII.5}$$

By applying these relations for both primary and secondary nozzles, and considering the mass flow rate in their injection planes, the ideal force is computed as:

$$F_{ideal} = \dot{m}_{inj\ prim} V_{ideal\ prim} + \dot{m}_{inj\ sec} V_{ideal\ sec} \tag{VII.6}$$

Finally, the objective function J to maximize is defined as:

$$J = \frac{(F_{net} + D_{external})}{F_{ideal}} \tag{VII.7}$$

In this expression, increasing the mass flow rate not only benefits to F_{net}, but also modifies F_{ideal}. Thus, the objective function takes into account the intrinsic dependency of thrust on the mass flow rate. By introducing an ideal term and following the recommendation made in V.8, the shortcomings of previous two-dimensional optimizations are addressed. In addition to the geometrical area constraint presented in VI.1, this definition of J ensures that nozzle efficiency is improved at a given mass flow rate and enables to avoid the definition of an optimization constraint on this quantity.

VII.1.4 Optimization workflow and tools

An optimization workflow that integrates industrial design tools is implemented for this study and displayed on Fig. VII.4. This process includes the geometrical model introduced in VI.1, the mesh generation tools described in VI.2, and aerodynamic computations of the flow.

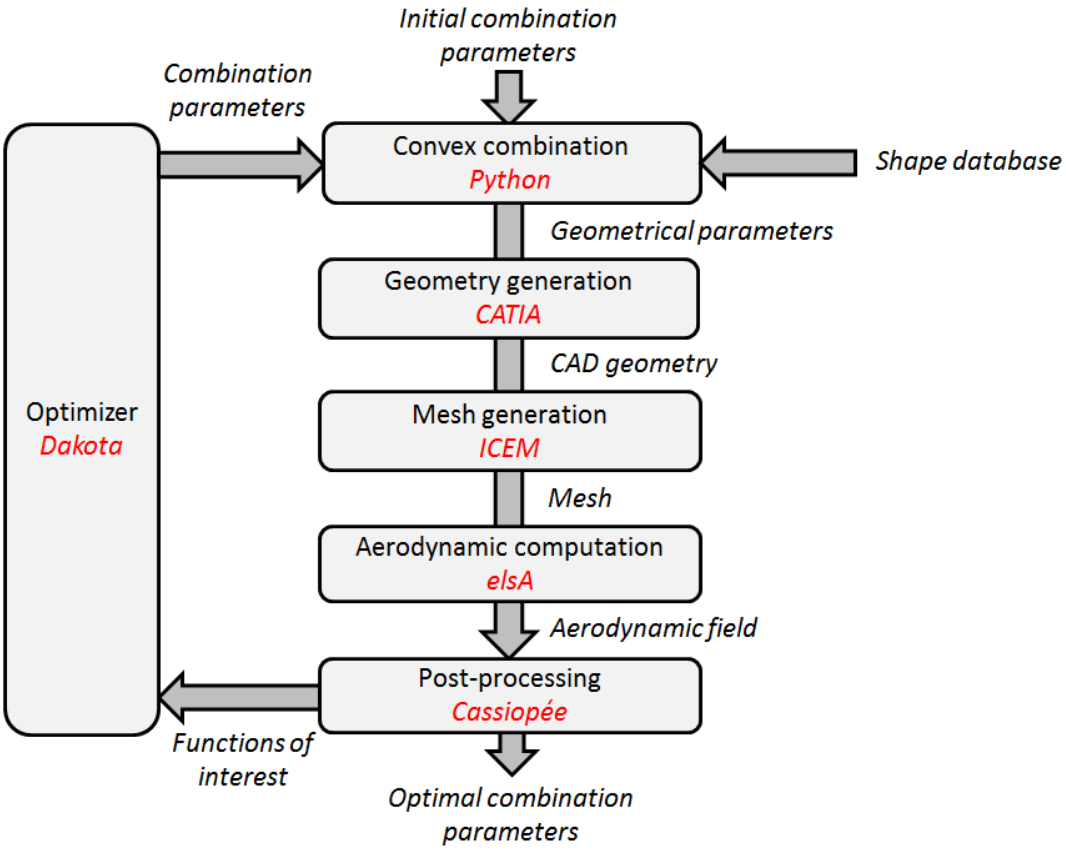

Figure VII.4 – *Optimization workflow based on industrial tools*

Optimizer and algorithm

This work consists in implementing the convex combination approach in an industrial optimization workflow. A dedicated step of the workflow generates the set of CAD parameters α_{geom} from the parameters of the expert configurations and the combination variables $\Lambda = \{\lambda_1, ..., \lambda_n\}$. Still, as design variables are managed by the optimizer, a "convex" constraint is defined on the sum of the design variables:

$$\sum_{i=1}^{n} \lambda_i = 1 \tag{VII.8}$$

This constraint has to be respected in order to be in the convex space. Consequently, the optimization problem considered is constrained.

At this point, it should be precised that although the convex combination method enables both gradient-free and gradient-based optimization processes, the choice is

made to use gradient-based descent methods. Therefore, optimizations are performed with Dakota [1], using DOT's modified method of feasible descent [85] to explore the constrained design space.

CAD and mesh generation

The CAD and the mesh are generated with the process presented and assessed in VI.

Aerodynamic computation

The flow around the nacelle is computed using the elsA solver [10] (property of Airbus-Safran-ONERA). The numerical settings for CFD simulations are presented in Table VII.3. In addition, multigrid methods with one level of coarse grid are used to accelerate the convergence rate.

Table VII.3 – *Numerical parameters for flow computation*

Flow equations	RANS
Turbulence model	Spalart-Allmaras
Spatial scheme	Jameson
Pseudo-time stepping scheme	Backward Euler and LUSSOR implicit phase scalar

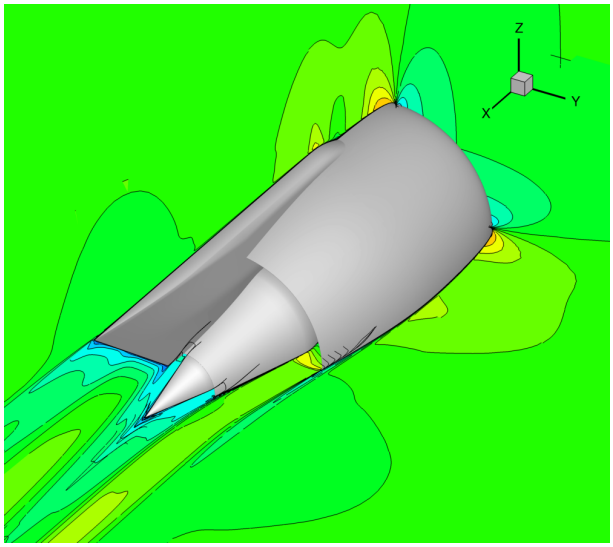

Figure VII.5 – *Mach number field computed around the nacelle displayed in y=0 and z=0 planes*

A post-processing based on Cassiopée [7] computes the quantities of interest from the aerodynamic field.

VII.2 Robustness of the workflow

First optimizations launched with the CAD-based workflow have pointed out some issues preventing the good behavior of the process. The main reasons for the errors were that:

- The CAD model did not manage to generate the geometries associated to some sets of parameters.
- Even if the CAD model was acceptable, the meshing process generated some negative volume cells.

In particular, these errors mostly occurred when the set of design variables required by the optimizer exceeded the value imposed to the convex constraint: $\sum_{i=0}^{n} \lambda_i = 1$. Unfortunately, these steps can be necessary for the descent algorithm.

In order to manage these robustness issues, two main actions have been taken. Firstly, the design variables associated to the inlet and the upstream external cowls have been fixed at a constant value. These design parameters are out of the scope of the present work, because they do not influence the rear-body and nozzles geometry. However, they can be altered if the convex constraint is not respected (i.e. $\sum_{i=0}^{n} \lambda_i \neq 1$). This appears as the source of several errors that happened on the CAD model. Consequently, considering them as non-modifiable in the workflow increases the robustness of the process.

Secondly, it appears that despite the previous improvements, the optimization process sometimes requires sets of parameters that highly exceed the capabilities of any CAD model. This happens in particular when the optimizer moves away from the convex and $|\sum_{i=0}^{n} \lambda_i - 1| >> 0$. In order to address this issue, an error management is implemented in the process. When the design variables lead to a degenerate geometry, a dummy value is set as objective function and the process continues.

To conclude, the adjustments made on the available CAD parameters, in addition to the robustness of the model described in Chapter VI, reduce the probability of getting degenerate geometries. Moreover, an error management has been implemented to avoid a crash of the process when the optimizer exceeds the value of the convex constraint. Together, they enable the good operation of the optimization workflow.

VII.3 Optimizations of turbofan nozzle shapes

The workflow based on CAD-generated nozzle shapes and aerodynamic flow computations is now used with the convex combination approach to perform optimizations.

VII.3.1 Shape database for combination

For this first application, the database generated in VI.4.1 is re-used. Consequently, this optimization will focus on the geometry of the secondary nozzle, and comprise only 3 geometries (vertically ovalized, extended and shortened).

VII.3.2 Optimized nozzle

The optimization process is launched from the barycenter of the convex space, with $\Lambda = \{0.3333, 0.3333, 0.3333\}$. After 2 gradient computations and a total of 41 evaluations, the descent algorithm converges. The resulting optimal shape enables an improvement of 0.9% on the objective function, with respect to the value of the reference nozzle shape (see comparison in Table VII.4). In addition, this shape is better than the three expert shapes in the database.

Table VII.4 – *Performance comparison of the nozzle shapes*

Configuration	Objective function J/J_{ref} [1]
Reference	1.0000
Vertically ovalized secondary nozzle (X_1)	0.9182
Extended secondary nozzle (X_2)	1.0042
Shortened secondary nozzle (X_3)	0.9625
Starting shape	0.9952
Optimal nozzle	1.0090

The coefficients for optimal combination are $\Lambda = \{0.000, 0.757, 0.243\}$. Their values give valuable information to the designer on the configurations of the database. The shape X_1, with the ovalized nozzle, has completely been abandoned to the profit of the shapes that modified the nozzle length. Moreover, the fact that $\lambda_2 > \lambda_3$ indicates a preference for the extended secondary nozzle.

Then, the nozzles shapes can be compared in the $z = 0$ plane, as displayed on Fig. VII.6. On this figure, it appears that the optimal shape has an extended secondary nozzle in comparison with the reference. Moreover, due to the design of the "expert" configurations in the database, this choice of coefficients also has an influence on the inner shape of the nozzle. The secondary duct appears to have a reduced curvature and a less pronounced "S"-shape than on the shortened and the reference geometries.

Next, a look at the Mach fields in the nozzles (Fig. VII.7) enables to have a physical understanding of the optimization result. The plot shows that the maximum Mach number in the optimal nozzle is lower than in the reference shape. This observation confirms that the Mach evolution along the secondary duct plays a role in the improvement of the objective function. By reducing the flow velocity, the optimizer also reduces the friction on the nozzle wall, and increases the efficiency of the engine.

[1] Reminder: in this case and in the following, the objective function J is maximized by the optimizer

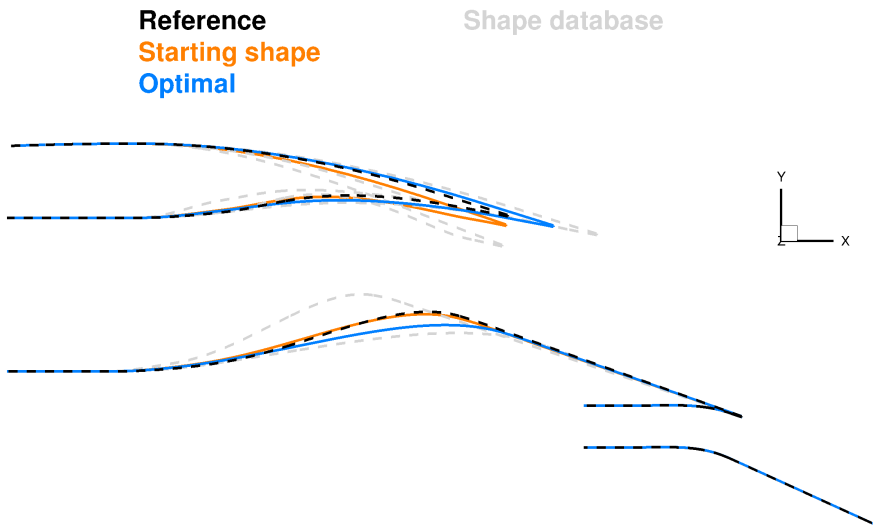

Figure VII.6 – *Comparison of the nozzle geometries, for a slice in the $z = 0$ plane*

Then, the pressure coefficient is defined as:

$$C_p = \frac{p - p_\infty}{\frac{1}{2}\rho_\infty V_\infty^2} \tag{VII.9}$$

C_p is computed on the surface of the nacelle and plotted on Fig. VII.8. It appears that the low pressure coefficient area on the inner wall of the secondary nozzle has been reduced on the optimal shape. This is in good agreement with the velocity reduction that has been observed on the Mach fields. The surface mapping of C_p shows how shape modifications can alter skin pressure distribution, and gives the designer additional information on nozzle configurations.

A detailed breakdown of surface force contributions gives further understanding of the performance improvements that have been made between the optimum and the reference.
The optimal shape increases the net thrust of the IPPS, F_{net}, by 0.24% in comparison with the reference. In particular, the modification of the secondary internal duct shape enables an improvement by 0.52% of the integrated force term in the secondary exhaust plane, $F_{secondary}$. The shorter primary cowl of the optimal nozzle implies a decrease of the cowl area, and results in lower pressure and friction forces. Thus, F_{cowl} is reduced by 12% with respect to the reference. Then, due to the choice of the shapes in the database, primary nozzle and plug geometries are fixed. As a consequence, $F_{primary}$ is unchanged. F_{plug} is slightly influenced by the modifications operated on the secondary nozzle and varies by 0.81%, but has little influence on overall performance. Finally, as the shape and boundary condition of the inlet are unchanged, the upstream term F_∞ is constant. Therefore, it appears that the net thrust increase is only due to the improvement of engine rear-body performance.
However, the drag of the engine configuration, $D_{external}$, is also impacted by shape modifications. The longer secondary cowl retained on the optimal nozzle implies an increase of the external nacelle area, and induces greater resulting pressure and friction forces. On this element, it appears that pressure forces prevail over friction. Due to the shape of the external nacelle cowl, they result in a drag reduction. Thus, $D_{external}$ is reduced by 2.56%.

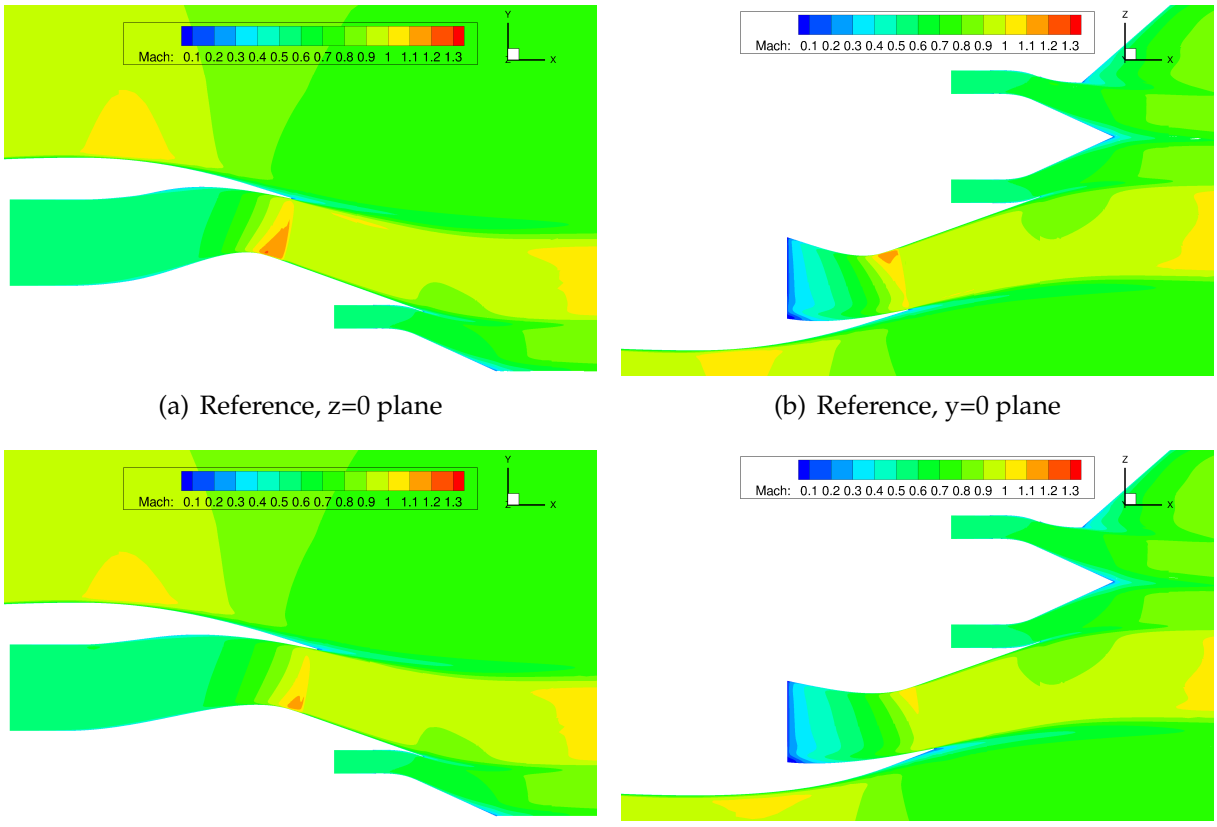

(a) Reference, z=0 plane

(b) Reference, y=0 plane

(c) Optimized, z=0 plane

(d) Optimized, y=0 plane

Figure VII.7 – *Mach field in slices of the reference and optimized nozzle shapes*

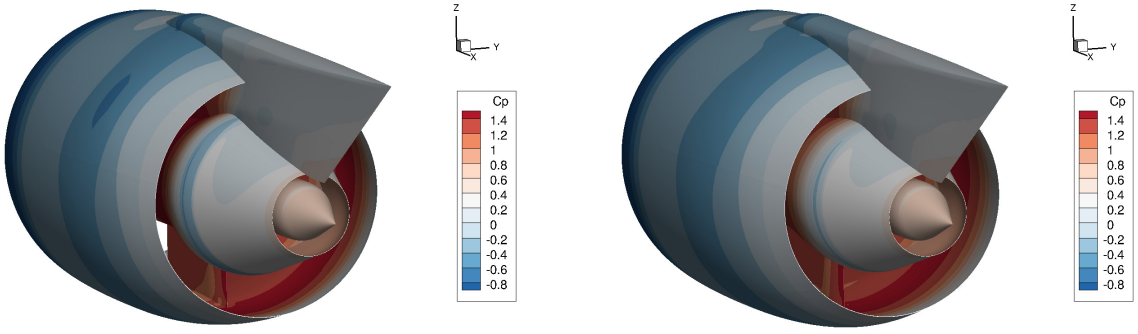

(a)

(b)

Figure VII.8 – *Skin pressure on the reference (a) and optimized (b) nozzle shapes*

In the end, the retained optimal shape has both an increased net thrust and a reduced nacelle drag in comparison with the reference, which lead to a better overall performance.

VII.3.3 Modification of the shape database

The first optimization result on UHBR nozzles showed that the shape with a vertically ovalized secondary nozzle has been abandoned. Therefore, this shape is being replaced

in the database for the next optimization run. A new shape depicted in Fig. VII.9 is introduced as X_1, with a vertically ovalized primary nozzle. This geometry has been generated from the reference and by altering parameters associated to the primary nozzle. Consequently, the addition of this shape in the database introduces the possibility of modifying the primary nozzle when performing convex combination. Moreover, it appears that changes on the primary duct have significant effects on the secondary nozzle, due to the geometrical construction of the CAD model. Finally, the updated database comprises 3 nacelle geometries with:

- vertically ovalized primary nozzle (X_1)
- extended secondary nozzle (X_2)
- shortened secondary nozzle (X_3)

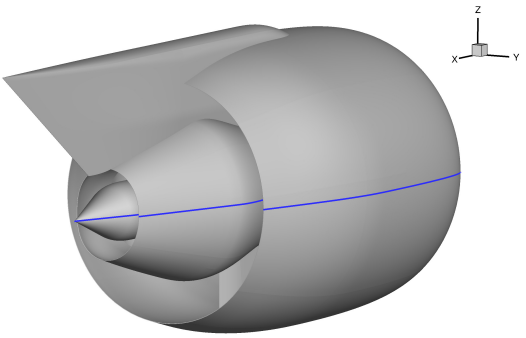

(a)

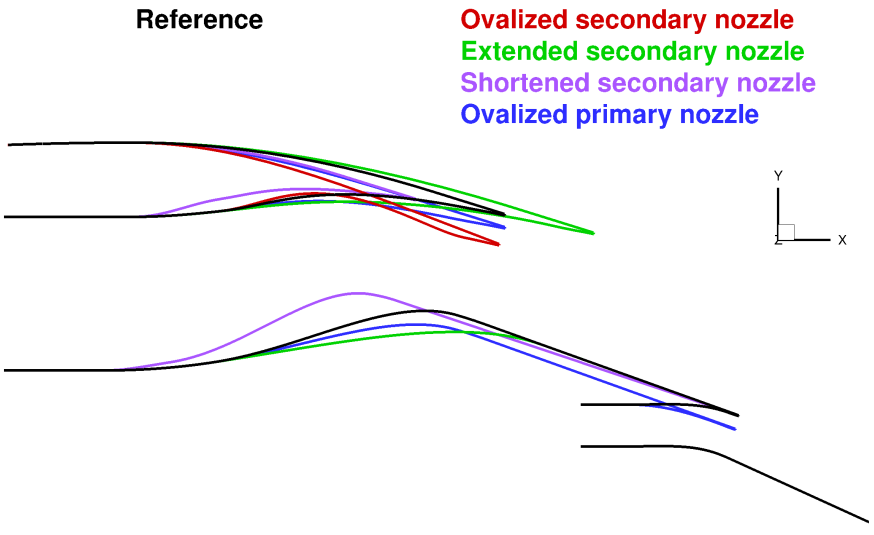

(b)

Figure VII.9 – *Overview of the configuration with vertically ovalized primary nozzle (a) and comparison with other database shapes in a slice (b)*

Again, the optimization is launched from the barycenter of the subspace. The optimizer performs 3 gradient computations during the descent and converges after a total of 25 evaluations.

The optimal shape is obtained for $\Lambda = \{0.311, 0.598, 0.092\}$. The coefficients indicate that the introduced shape X_1, with an ovalized primary nozzle, participates significantly in the final combination. In this case, the starting shape of the optimization happens to have a better performance than the reference (see Table VII.5). However, the new optimal shape returned by the optimizer still achieves an improvement of the objective function J. The optimal performance is similar but slightly lower than the previous optimal shape found in VII.3.2.

Table VII.5 – *Performance comparison of the nozzle shapes of the second optimization*

Configuration	Objective function J/J_{ref}
Reference	1.0000
Vertically ovalized primary nozzle (X_1)	0.9994
Extended secondary nozzle (X_2)	1.0042
Shortened secondary nozzle (X_3)	0.9625
Starting shape	1.0056
Optimal nozzle	1.0087

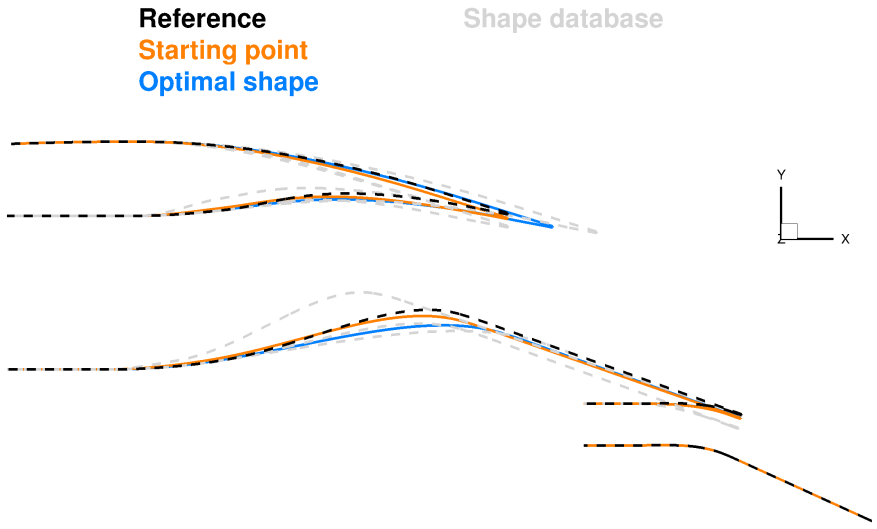

Figure VII.10 – *Comparison of the nozzle geometries, for a slice in the $z = 0$ plane (second optimization)*

When comparing the geometries in a slice, as depicted in Fig.VII.10, it appears that the retained shape has a slightly ovalized primary nozzle and a longer secondary nozzle than the reference. Again, it appears that extending the secondary duct leads to a smoother internal shape, which is due to the definition of the expert configurations for this case.

Then, the Mach fields of reference and optimized nozzle shapes are compared on Fig. VII.11. It appears that the optimizer leads again to a shape with a reduced maximal Mach number in the secondary duct. Moreover, a comparison between the optimized nozzle and the shape obtained in VII.3.2 shows that the Mach fields are similar. Thus, it seems that the aerodynamic effects of primary nozzle ovalization cannot be seen on these visualizations.

Next, skin pressure coefficient (C_p) contours of the optimal and reference shapes are compared and depicted in Fig. VII.12. The main differences are located on the external

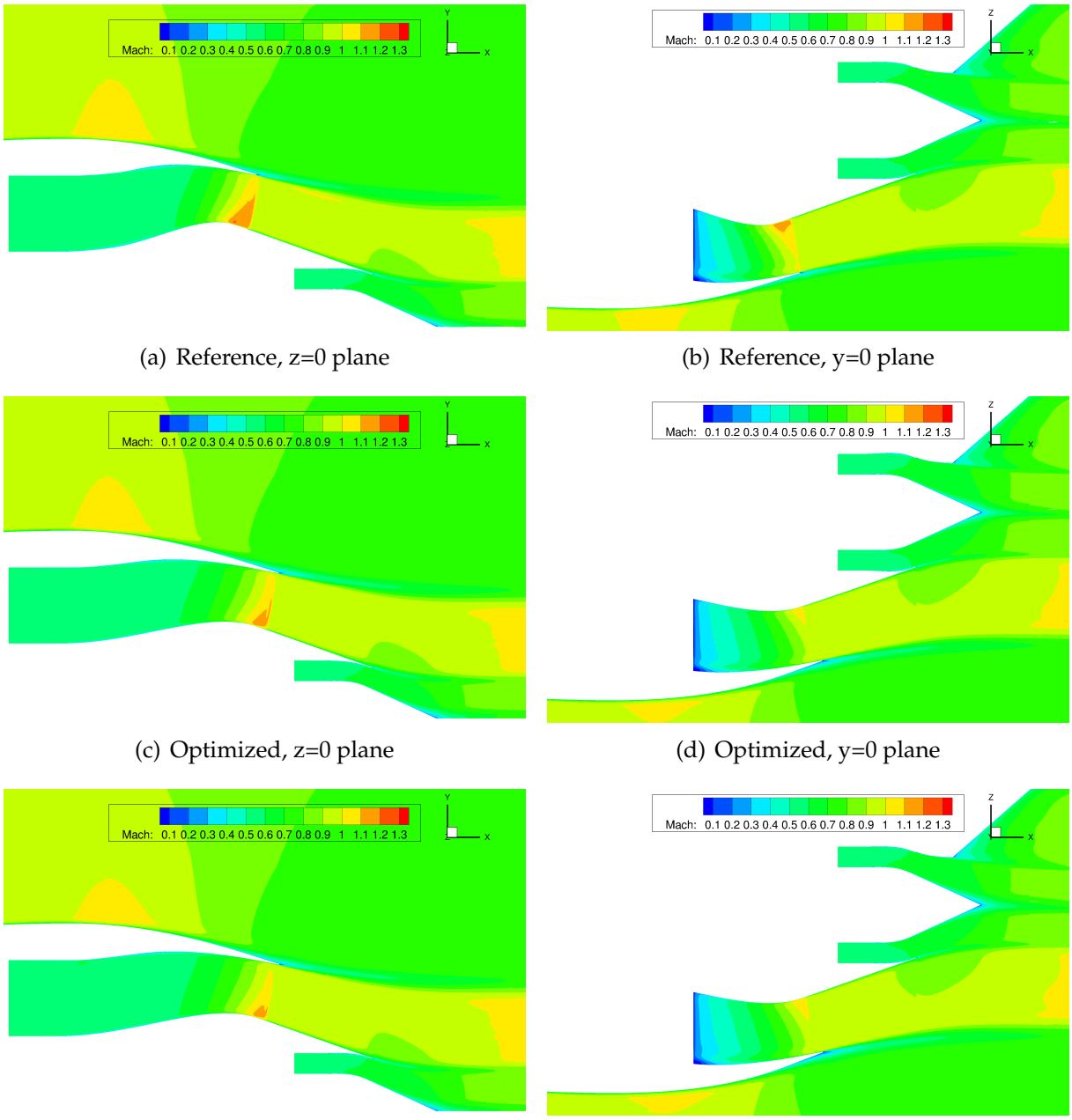

(a) Reference, z=0 plane

(b) Reference, y=0 plane

(c) Optimized, z=0 plane

(d) Optimized, y=0 plane

(e) Optimized, z=0 plane (from VII.3.2)

(f) Optimized, y=0 plane (from VII.3.2)

Figure VII.11 – *Mach field in slices of reference and optimized nozzle shapes*

nacelle cowl, the internal secondary nozzle and the primary cowl, where low-pressure regions are reduced in size and intensity.

The breakdown of surface force contributions on the IPPS shows that the good performance of the optimal shape is of a different nature than for the previous optimum obtained in VII.3.2.
Indeed, the optimal shape does not improve the net thrust F_{net}, that is even slightly reduced by 0.04% with respect to the reference. In detail, it appears that the optimizer has again improved the thrust term in the exhaust plane of the secondary nozzle, $F_{secondary}$, by 0.57%. Nevertheless, the shorter and ovalized primary cowl leads to a decrease of F_{cowl} by 15%, and counterbalances the improvements made at the secondary exhaust.

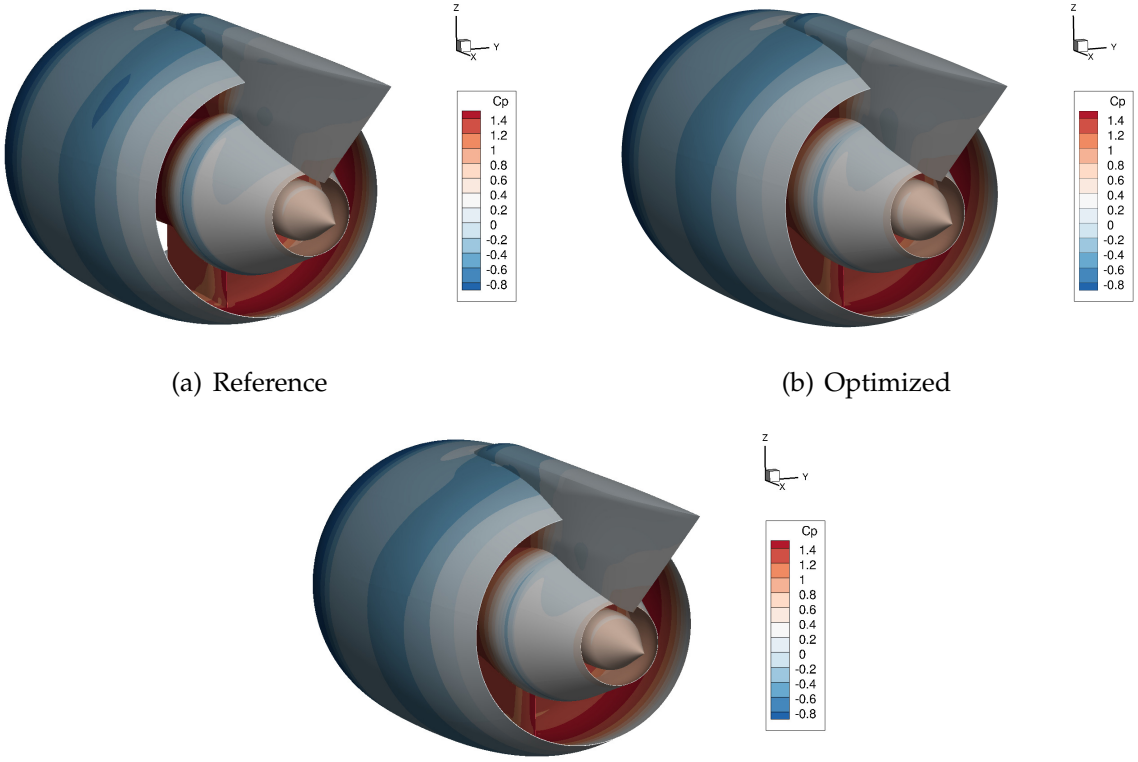

(a) Reference

(b) Optimized

(c) Optimized (from VII.3.2)

Figure VII.12 – *Skin pressure on reference and optimized nozzle shapes*

The primary exhaust and plug terms, $F_{primary}$ and F_{plug} respectively, are slightly modified, with no significant effect on overall performance.
The main improvement of this shape is the reduction of the external nacelle drag $D_{external}$. In comparison with the reference, the external cowl is longer and its area is increased. As explained in VII.3.2, the pressure forces prevail on friction and the nacelle external shape implies a drag reduction of 3.50%.
Therefore, it appears that this optimal nozzle shape allows a strong drag reduction with respect to the reference, while keeping a similar net thrust level.

To sum up, replacing a shape in the database for combination has led the optimizer to a different result. This time, a breakdown of surface force contributions indicates that different physical mechanisms are responsible for the performance improvement. However, the efficiency of this second optimum is not better than the first presented in VII.3.2.
Since the previous optimal shape was defined as a combination of only two expert shapes (X_2 and X_3), it belonged to the border of the subspace. X_2 and X_3 remained unchanged in the current database, that is why the optimum obtained in VII.3.2 still belongs to the combination subspace. Consequently, two optimal nozzles have been found in the current subspace, which suggests the existence of local optima. In order to have a better understanding of the space defined with the convex combination approach and the current database, an investigation with DOE is proposed.

VII.3.4 Design of experiments and response map of the design space

A DOE is performed on the shape database presented in VII.3.3. The sampling of 68 elements, generated for a database of three shapes and used in V.5 with single-flow nozzles, is re-used.

The 68 samples are evaluated with the same workflow as the optimizations and can be observed on Fig. VII.13(a). It appears that six samples returned an error, due to CAD or mesh generation issues. These errors highlight that despite the robustness improvements that have been made, changing the shapes database can lead to new issues. An efficient way to improve the models and avoid such issues remains to generate a sample of geometries, in order to identify them, and to address them one by one.

Then, an interpolation is operated with Kriging on the valid samples. This leads to the response map represented on Fig.VII.13(b). On this map, the trends from the DOE are confirmed and an area of interest appears. The final point of the feasible descent operated in VII.3.3 belongs to this area, as well as the previous optimization result found in VII.3.2. However, the precision of the DOE is too coarse to identify the exact region of optimal performance. When comparing the sample evaluations and the two optima, it appears that the best overall configuration remains the first optimum found in VII.3.2, located on the border of the design space. Moreover, some points evaluated in the DOE have a slightly better performance than the second optimum found in VII.3.3. This observation suggests that the design space should be refined in the area of interest, in order to identify precisely the best combination coefficients. In conclusion, this response map confirms the capability of the feasible descent to converge towards the region of interest of the design space, but also shows the limitation of the descent method when it comes to finding an exact global optimum.

VII.4 Chapter summary

This chapter presents the first optimizations performed on complex UHBR nozzles geometries generated with CAD. First, an optimization problem has been defined to improve the performance of isolated turbofan nozzles at given engine operating conditions. A workflow has been described, that comprises industrial CAD software and meshing tools as well as CFD simulations of the aerodynamic flow and dedicated post-processing. This workflow has been used with convex combination and feasible descent on a first shape database of dimension 3 and resulted in a significant performance improvement of the nozzles of an isolated turbofan. However, one shape has been abandoned by the optimizer for the optimal combination. Consequently, this shape has been replaced in the database, and the optimization process has been relaunched. This resulted in a different optimal configuration, with similar performance to the previous optimum but different improvements. The presence of two optimal shapes with similar performance in the same design space suggested the presence of local optima. Therefore, the design space defined by the latest database has been investigated by a DOE. An interpolated response map has highlighted an area of interest

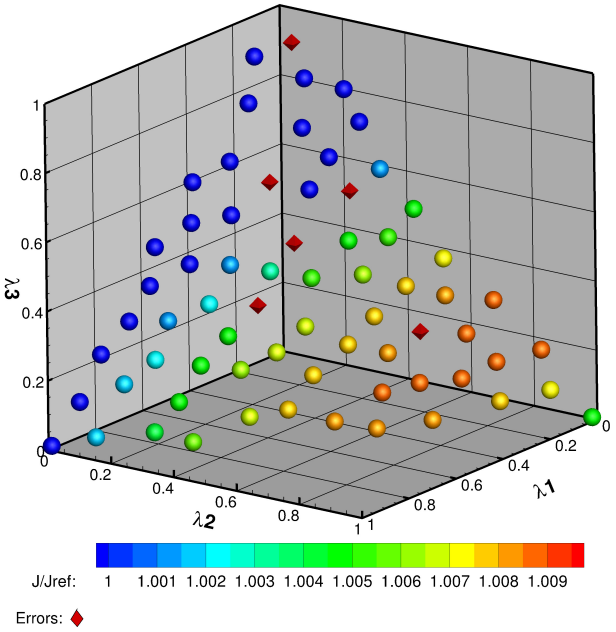

(a)

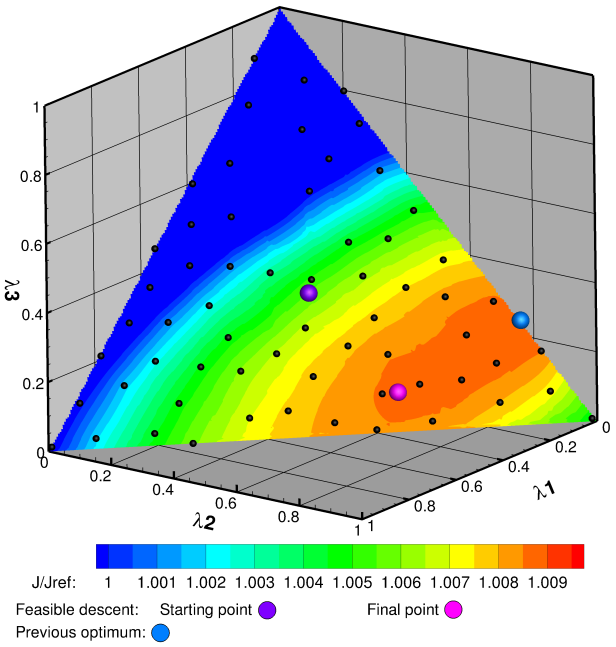

(b)

Figure VII.13 – *Set of points (a) and interpolated response surface (b) obtained with a numerical DOE for UHBR nozzles*

for this problem, in which the two optima are located. These optimization examples have confirmed the possibility of improving the performance of complex nozzles defined with CAD, by using convex combination. However, the optimization problem has been defined considering fixed operating conditions of the engine. At this point, a coupling with a thermodynamical engine model appears necessary in order to assess the impact of nozzle shape modifications on overall IPPS performance.

VIII

Developments towards coupled aeropropulsive nozzle optimizations

Contents

The interests of performing coupled aeropropulsive simulations for nozzle design and optimizations are presented in this chapter, as well as the associated strategies and developments.

First, the phenomenological interactions between nacelle aerodynamics and engine thermodynamics are detailed. Taking these effects into account for simulation requires to consider specific coupling loops.

Then, several coupling strategies are defined, assessed and compared. In particular, their convergence level and rate are evaluated.

Finally, an aeropropulsive simulation of an optimal nozzle obtained in VII is performed, in order to assess the benefit of considering such simulation in the optimization process.

VIII.1 Definition of a coupling strategy to perform coupled aeropropulsive simulations of a thrust-drag balanced aircraft

Nozzles, as mentioned in II.3.1, are responsible for setting the mass flow rate in the turbofan engine. Thus, nozzle performance has an influence on the operating conditions of the other engine components. From a thermodynamic point of view, nozzle design has a significant impact on the operating point of the engine cycle. Reciprocally, aerodynamic nozzle performance depends on the operating conditions of upstream engine components. Thus, a strong interdependency exists in the IPPS between the nozzles operating conditions and the engine cycle operating point. As a result, the joint operating point of these components on the industrial system is a point of "equilibrium" on their respective operating lines. In industrial design phases, this effect is accounted for by converging iteratively nozzle aerodynamic design and the operating conditions of other components.

This study aims at optimizing the performance of the IPPS, by modifying nozzle shapes and considering a fixed turbofan engine cycle. In order to consider their interdependency, simulations have to take into account the effects of nozzle shape modifications on the engine cycle operating point, and conversely. In practice, the goal is to implement coupled aeropropulsive simulations, that operate a coupling between aerodynamic computations and an engine thermodynamic model.

In order to assess the required coupling loops, an initial aerodynamic simulation of the nacelle is considered. This simulation, defined following the methods described in VII.1.4, is assumed to be converged in agreement with the operating point of the engine thermodynamic cycle. Then, a nozzle shape modification is operated and its effects are detailed.

First, a modification of nozzles geometry has an effect on the aerodynamic flow inside the nozzle ducts. Given that total pressure and temperature (p_i, T_i) are imposed at the injection boundary conditions of the nozzles, the mass flow rate and the pressure at the interface can be altered. In this case, the operating point of the engine thermodynamic cycle is no longer suited to nozzle performance and an adjustment is needed. For simulation purpose, a coupling loop can be defined between the aerodynamic simulation and a thermodynamic engine model. Post-processed aerodynamic quantities are transmitted to the thermodynamic model, that returns updated boundary conditions (p_i, T_i) for the aerodynamic simulation. The resulting coupling loop can be represented as depicted in Fig. VIII.1.

When aerodynamic simulations of the engine are performed for a given level of resulting thrust, a second consequence of nozzle shape modifications appears. If the simulation is assumed to have re-converged towards a joint operating point in agreement with the thermodynamic engine cycle, the resulting forces on the IPPS can be altered. In this case, the drag-thrust balance of the aircraft is no longer satisfied. A second coupling loop is defined, located above the previous, that comprises a control setting to adjust the thrust and satisfy the balance. On the aircraft, this control setting

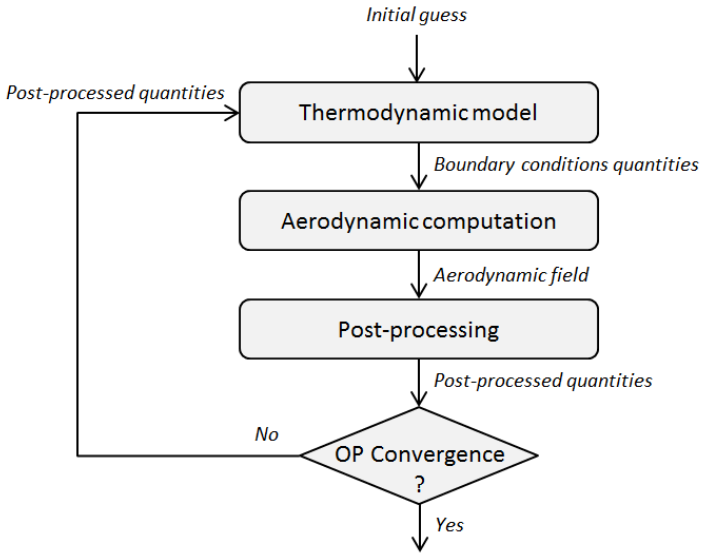

Figure VIII.1 – *Coupling loop for engine operating point (OP) convergence*

is associated with the throttle command. A schematic view of the coupling process including this second loop is presented on Fig. VIII.2.

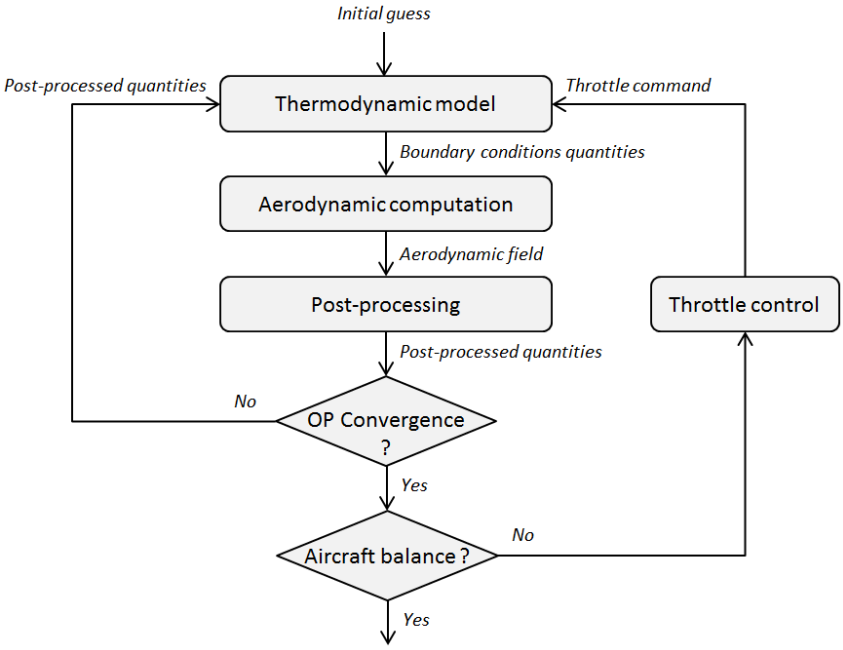

Figure VIII.2 – *Coupling loops for engine operating point (OP) convergence and aircraft balance*

To sum up, two coupling loops have to be defined to achieve coupled aeropropulsive simulations of a thrust-drag balanced IPPS. According to the principle depicted in Fig. VIII.2, the two loops should be converged sequentially. For each throttle command, the operating conditions can be converged and then the drag/thrust balance evaluated. Then, the throttle loop is operated and the operating point should be re-converged. However, this process appears laborious considering that each coupling step involves a CFD computation. The proposition is made to merge these two loops into one, where both the operating conditions of the engine and the throttle command

are updated at each step. The obtained coupling process (Fig. VIII.3) is based on the assumption that both can converge together. This method is retained and the assumption will be verified in the following work.

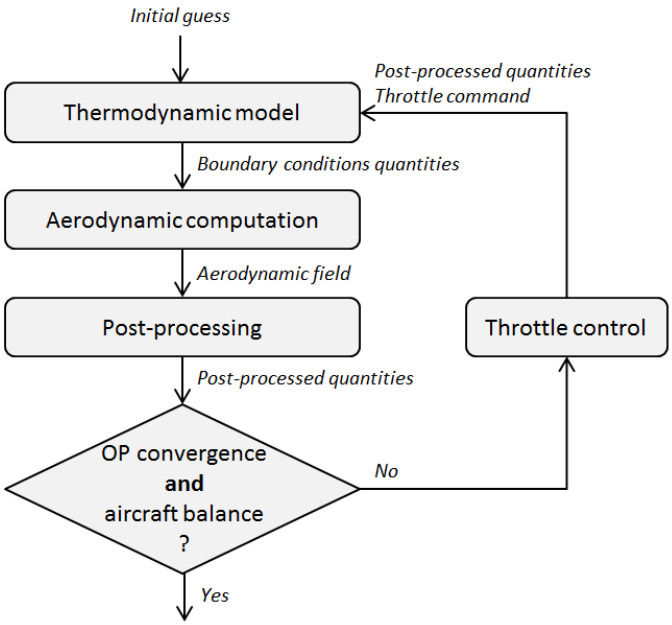

Figure VIII.3 – *Merged loops for engine operating point (OP) convergence and aircraft balance*

The process detailed here can be applied for an isolated nozzle case, as the one studied in Chapter VII. To go further, one can consider aerodynamic simulations of a complete aircraft with under-wing mounted engines. However, in this situation, additional effects must be taken into account. In particular, modifying the shapes of an installed under-wing IPPS impacts engine performance, the resulting forces on the engine, but can also alter the lift and drag of the aircraft (see the literature in III.1). Therefore, a new coupling loop can be defined to control the angle of attack, in order to retrieve the initial lift coefficient and enable complete performance comparison. For instance, this loop is considered in Appendix A for the establishment of adjoint equations. Finally, a loop should also be defined to maintain a constant coefficient of moment and aircraft stability by modifying the horizontal tail plane angle.
These developments represent an interesting perspective of the present study, but have not been implemented in the scope of the thesis work.

VIII.2 Application of different methods for "manually" coupled aeropropulsive simulations

Now, the coupling approach described in VIII.1 is used with aerodynamic simulations on a turbofan engine configuration. For this first application of aeropropulsive coupling, the iterations are operated "manually". At each step, the CFD simulations are fully converged, the post-processed values are provided to the thermodynamic model, the resulting boundary conditions are modified and the computation is relaunched.

The goal of this work is to confirm and assess the convergence of the aeropropulsive coupling. It also enables to compare different coupling approaches and their convergence rate.

The thermodynamic engine model described in VII.1.2 is re-used and integrated in the coupling loops. Consequently, its role is to provide updated quantities to impose on the boundary conditions of the aerodynamic computations, based on post-processed aerodynamic values and the throttle command.

It is assumed that a first aerodynamic computation has been done for a throttle command T_i, with a set of boundary conditions BC_i, and has led to post-processed values of the net thrust $F_{net\,i}$, the external drag $D_{external\,i}$, and of aerodynamic quantities $A_{aero\,i}$.

Concerning the convergence of the engine operating point, the boundary conditions of the aerodynamic computations are updated depending on the previous iteration i. The new set of conditions is obtained with the thermodynamic model (f_{thermo}):

$$BC_{i+1} = f_{thermo}(A_{aero\,i}, T_i) \tag{VIII.1}$$

Then, the throttle command has to be updated to respect the aircraft balance. As this study focuses on the cruise flight condition of the aircraft and considers an isolated engine, the thrust-drag balance to satisfy is obtained by projecting the forces on the engine axis:

$$F_{net} + D_{external} + D_{airframe} = 0 \tag{VIII.2}$$

where F_{net} and $D_{external}$ are computed with aerodynamic post-processing and $D_{airframe}$ is the drag of the airframe, considered constant for isolated engine computations. Moreover, thrust terms are accounted as positive, while drag terms are negative. A residual is defined as:

$$R_i = F_{net\,i} + D_{external\,i} + D_{airframe} \tag{VIII.3}$$

such that the aircraft balance is satisfied when $R = 0$.

Several types of control functions have been implemented and tested "manually" to tackle the coupling of the throttle command. This comparative study aims at demonstrating their convergence and assessing their convergence rate. However, the control functions considered remain simple, and further work would be needed to find an optimized convergence rate.

The first and most intuitive choice has been to implement:

$$T_{i+1} = T_i(1 - \Delta_i), \text{ with } \Delta_i = \frac{R_i}{F_{net\,i}} \tag{VIII.4}$$

This function has been tested on 5 iterations and shows convergence towards thrust-drag balance (see Fig. VIII.4). However, the convergence is slow and significant oscillations appear, that strongly affect the efficiency of the coupling. Therefore, a damping coefficient is introduced to reduce the oscillations, and the second throttle control function is defined as:

$$T_{i+1} = T_i(1 - \Delta_i), \text{ with } \Delta_i = \frac{1}{2} \times \frac{R_i}{F_{net\,i}} \tag{VIII.5}$$

The coefficient has been chosen empirically as 0.5. In this case, the oscillations amplitude reduces rapidly and the convergence is accelerated towards thrust-drag balance.

Finally, a secant method is implemented. After two iterations with the damping coefficient, an estimate of the derivative can be computed and the command is iterated as:

$$T_{i+1} = T_i(1 - \Delta_i), \text{ with } \Delta_i = \begin{cases} \frac{1}{2} \times \frac{R_i}{F_{net\,i}}, & \text{if } i < 1 \\ \frac{T_i - T_{i-1}}{R_i - R_{i-1}} R_i, & \text{otherwise} \end{cases} \tag{VIII.6}$$

The convergence comparison with the two other approaches depicted in Fig. VIII.4 shows that the secant method has the fastest convergence rate at this point. The amplitude of the oscillations reduces rapidly and after 5 iterations the aircraft balance residual R is reduced by an order of magnitude. Consequently, this method is retained for throttle coupling.

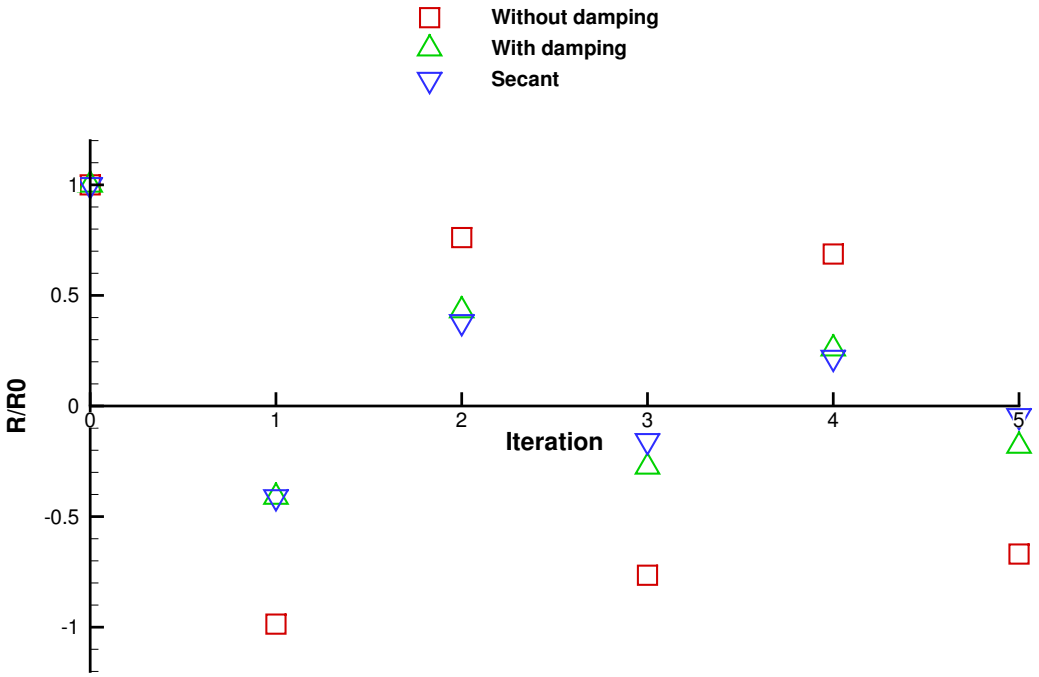

Figure VIII.4 – *Convergence of the residuals for 3 different coupling approaches*

VIII.3 Coupled aeropropulsive simulations of an optimal shape

In order to highlight the benefit of using coupled aeropropulsive simulations in optimization processes, such simulation is performed on the optimal shape obtained in VII.3.2. At fixed operating conditions, this shape allowed a net thrust increase and a drag reduction. However, these operating conditions are inherited from the reference shape, and are not representative of the behavior of a real engine configuration

with modified nozzle shape (due to the interdependency described in VIII.1). A precise evaluation of the associated performance improvement requires an update of the engine operating point.

The coupling is operated "manually", following the procedure described in VIII.2. The process is stopped when thrust-drag balance is satisfied and the aerodynamic boundary conditions are converged. Table VIII.1 presents the evolution of some quantities between reference and optimal nozzle shapes, after aeropropulsive coupling. In this case, the optimal nozzle shape enables a reduction of the external nacelle drag $D_{external}$ by 0.68% with respect to the reference. As a consequence, the net thrust produced by the engine, F_{net}, is reduced by a similar amount. This confirms that after adjusting the operating point to satisfy drag-thrust balance, the shape proposed by the optimizer still allows a lower drag count than the reference, resulting in a decrease of the required net thrust. Nevertheless, the estimated fuel consumption of the engine, $\dot{m}_{fuel}$, is only reduced by 0.025%, which may seem counter-intuitive.

Table VIII.1 – *Performance evolution between optimal and reference nozzle shapes, after aeropropulsive coupling*

Q quantity	$\Delta = \left(\frac{Q_{opt} - Q_{ref}}{Q_{ref}}\right)$
$D_{external}$	-0.677 %
F_{net}	-0.671 %
$\dot{m}_{fuel}$	-0.025 %
$\left(\frac{p_{i\,inj}}{p_{i\,exhaust}}\right)_{sec}$	-0.059 %
$\dot{m}_{inlet}$	+0.201 %

This outcome can be explained by a physical analysis of engine aerodynamics. In particular, the total pressure losses in the secondary nozzle are increased on the optimal shape. Consequently, the nozzle efficiency to convert total pressure into thrust is reduced. In order to counterbalance this efficiency loss, the coupling leads to an increase of the mass flow rate $\dot{m}$ flowing through the engine. However, this has a significant effect on the inflow momentum of the engine F_∞, and induces a greater ram drag in the balance. This drag increase nearly compensates the benefit of nacelle drag reduction. Finally, the engine has to deliver a similar amount of total pressure to obtain a lower net thrust, that is why the fuel consumption is merely reduced at the margin.

This effect could not be captured by the optimization problem defined in VII. The formulation considered fixed boundary conditions for the aerodynamic computation. Only the isentropic pressure and temperature (p_i, T_i) are imposed at the injection boundary conditions of the nozzles. Therefore, geometry modifications of nozzle ducts can alter the mass flow rate at the primary and secondary exhausts of the engine. On the other hand, no modification of the incoming mass flow rate is operated at the inlet of the engine during optimization. Thus, an inconsistency appears between the mass flow rate entering the inlet and the mass flow rate in the nozzles. The coupled aeropropulsive simulation on the optimal shape suggests *a posteriori* that this phenomenon jeopardizes the optimization process. In order to assess a realistic performance, it ap-

pears necessary to take into account the mass flow rate changes and operate a coupling loop associated to aerodynamic simulations. In particular, considering an engine thermodynamic model in the coupling loop solves this issue and enables to minimize directly the fuel consumption.

As a conclusion, the shape returned by the optimization process in VII.3.2 does not have the expected performance when evaluated with coupled aeropropulsive simulations. After analysis, the mass flow rate inconsistency that may appear between the inlet and the nozzles is incriminated. This result highlights the interest of considering an optimization formulation based on a coupling loop. In addition, defining a loop for mass flow rate consistency represents a similar effort to considering a coupling with a full thermodynamic model of the engine. Thus, this justifies the integration of coupled aeropropulsive simulations within the optimization workflow for nozzle shapes.

VIII.4 Chapter Summary

Interactions between engine thermodynamics and nacelle aerodynamics have an impact on the performance prediction of the IPPS. In order to take them into account in design phases, simulations with coupling loops can be implemented. In this chapter, a coupling strategy and the associated methods have been developped and assessed for coupled aeropropulsive simulations. When applied on an optimal nozzle shape, this method highlights the limitations of the previous optimization problem and justifies the use of such simulations within optimization processes. Although the present thesis work did not include the implementation of fully CFD-embedded coupled simulations due to time constraints, the interest of considering such methods has been verified and technical steps have been made towards their implementation.

IX

Conclusions and perspectives

The work presented here aimed at implementing aerodynamic shape optimizations of turbofan engine nozzles in under-wing configuration, using coupled aeropropulsive simulations and industrial design tools. Although the complete problem could not be tackled in this study due to time constraints, several significant steps have been completed towards its implementation.

The first part of this work has been dedicated to investigating methods that allow to carry out optimizations on industrial cases with high number of design variables and non-differentiated design tools such as commercial CAD software. As it appears that these two objectives are contradictory, an original approach has been developed. This method proposes to define a subspace of the design space, by considering *convex combinations* of shapes from a reference database. Then, optimizations can be performed on the subspace by using the combination coefficients as design parameters, thereby reducing drastically the dimensionality of the problem. This enables the use of gradient-free and gradient-based methods in association with an industrial design workflow.
This method has the advantage of generating geometries as combinations of shapes provided by the designer, that is why it reduces the risk of generating industrially unfeasible aerolines. Moreover, it places the designer at the heart of the optimization process. The optimal combination coefficients returned by the process give valuable information for interpretation. Therefore, an innovative design approach is imagined, where a first shape database is proposed by the designer, a fast optimization is run with an overnight return time, and the database is modified depending on optimization results, then the optimization is re-launched, etc... This iterative process is particularly interesting for industrial early design phases.

The application of the method to a two-dimensional nozzle performance improvement has validated the proposed convex combination approach. For inviscid nozzle performance, feasible descent on the full design space established the existence of local optima. In this case, a more efficient shape has been returned by the optimization when

exploring the reduced space defined with convex combination instead. Therefore, this suggests that the proposed approach has avoided getting stuck in local solutions, by driving the exploration based on expert knowledge.
Optimizations performed on the viscous case have found a very performant shape by exploring the full design space. However, this shape does not comply with isentropic nozzle theory and questions the definition of the optimization problem. In this situation, using convex combination has helped at correcting the shortcomings of the problem definition. The reduced design space defined with three nozzle shapes in agreement with nozzle theory has enabled to define an industrially acceptable design subspace. Feasible descent applied on this subspace has returned an optimal shape with a significant performance improvement, although not better than the full-space shape. In addition, the database has been enriched with a fourth shape, which leads to further improvements on the objective function.
Due to the small number of configurations in the database for combination, designs of experiments have been operated on the reduced search space at affordable cost in both inviscid and viscous cases. Then, response surface interpolation has helped to understand the behavior of the optimizer and to highlight the limitations of the considered problem formulation. The dependency of nozzle performance on the mass flow rate is such that the latter should be directly integrated into the objective function rather than being defined as a constraint.

Next, an automated generation process has been defined and tested for turbofan nacelles with separate-flow nozzles and pylon. The CAD model is based on industrial design parameters and has been specially generated to enable large modifications of the rear-body. Moreover, the automation of geometric and mesh generations have allowed their use in an optimization workflow. The complete process has been applied to generate shapes as convex combinations of geometries, and has validated the possibility of driving CAD shapes with combination parameters. Still, some robustness issues have appeared during the testing on this first sampling. This emphasizes that despite preliminary robustness testing, CAD-based geometry generation is a sensitive process that needs to be operated with care, in particular in the scope of an optimization study.

Then, convex combination has been applied for performance optimization of turbofan nozzles on an isolated engine configuration. This first case of optimization with CAD-based geometry generation in the workflow has highlighted some additional robustness issues in the workflow. These difficulties have been solved thanks to CAD parameterization modification and error management.
Next, the optimizations that have been performed led to significant increase of the engine performance at given operating conditions. Moreover, due to the small number of shapes in the database, DOE has been performed and surface response drawn for a higher but still reasonable computational cost.

Finally, the interdependency between nacelle aerodynamics and engine thermodynamics has been accounted for design phases. This coupling is expected to have a critical influence on engine performance predictions when nozzle shapes are modified. A coupling strategy has been proposed to perform coupled aeropropulsive computations, and several coupling methods have been assessed on a first computation. Then, such computations have been converged and coupled "manually" for an optimal shape obtained at given operating conditions. The coupled simulation does not retrieve the

expected performance improvement and highlights the shortcomings of the previous optimization formulation. Although fully-embedded coupled aero-propulsive simulations could not be performed in the scope of the present work, technical steps have been made towards their use for nozzle design. In addition, their integration within nozzle optimization processes appears highly beneficial to obtain realistic performance predictions.

Perspectives

There are several perspectives to this work.

First and foremost, coupling a thermodynamic model with aerodynamic simulations has proven its interest in predicting engine performance. Therefore, the implementation of coupled aeropropulsive simulations should be continued an integrated into optimization workflows. This is expected to lead to more precise performance prediction. In addition, it would highlight the limitations of considering only aerodynamics in nozzle and nacelle shape optimizations.

Then, the final goal of this project can be achieved, namely applying the optimization process to an engine mounted under the wing of an aircraft configuration. Several essential steps towards this case have been developed and validated in this work. Yet, this targeted case requires a mesh of the full wing-body aircraft configuration, the integration of the engine mesh as a chimera overset, and implies heavier flow computations. Moreover, additional coupling loops have to be defined in comparison with the isolated nozzle case, in order to satisfy lift and momentum constraints on the aircraft. Overall, this is likely to result in a more complex and expensive optimization workflow. Still, such process would allow a comparison with isolated nozzles, and possibly demonstrate the interest of considering the aircraft/engine interactions during wing and engine nozzle design.

Next, it appears that the author's efforts have been focused on performing mono-objective optimizations through this study. Although considering an unique objective is easy to implement and necessary for first applications, it is not fully representative of the challenges of nozzle design. Due to operability constraints, the design of engine nacelle is actually a multi-point problem. As a consequence, an extension of this work to multi-point optimization is of great interest. For instance, the performance can be improved on the cruise operating point while satisfying a mass flow constraint for stall margin at take-off.

After that, convex combination has been demonstrated to be an efficient approach to reduce dimensionality and perform optimizations with CAD software. However, to this day, it has mostly been applied with steepest-descent methods. In light of the first applications, that show few regions of interest on the design space defined with convex combination, SBO appears as an efficient alternative. It would enable to overcome the limitations of descent algorithm that tend to get stuck in local optima, without having to pay the cost of global research algorithm. Therefore, their implementation and testing is an other perspective of this work.

Finally, this work has made the choice of not implementing adjoint-based gradient computations on the full design space. Gradient-based optimizations remain the most efficient way to finely improve the performance of a given design. Moreover, the independent cost of gradient estimate enabled by adjoint approach is an unquestionable advantage when it comes to problems with hundreds of design variables. Therefore, adjoint-based optimizations of nozzle performance can be performed as an extension of the present work. In particular, they can be used in combination with the developed convex combination approach, and represent the second step of a two-level optimization strategy. In this context, the approach presented in Appendix A is a good starting point for the development of an adjoint-compliant optimization workflow, provided that the two major bottlenecks identified (i.e. geometrical and post-processing sensitivity computations) are addressed properly.

A

Adjoint-based formulation of the complete problem

This appendix presents the gradient formulation for the shape optimization of a three-dimensional aircraft engine nozzle, mounted under the wing of an aircraft. The computations include an aerodynamic solver and a thermodynamic model of the engine. To compute this gradient, a formulation based on the adjoint approach is developed. The document is a step-by-step implementation of the gradient formulation, that integrates more coupling at each step of the process. Moreover, it comprises analyses of the terms appearing in the gradient formula, and how to obtain them (from an ONERA/Safran perspective).

Nomenclature

Some variables names and definitions may differ from the main document, that is why a nomenclature dedicated to this appendix is proposed:

A	Vector of aerodynamic variables after post-processing (e.g. mass flow rate)
alt	Flight altitude
BC_{eng}	Vector of flow characteristics, considered as boundary conditions for the aerodynamic model (p_s, p_i, T_i in the adapted planes)
CAD	Computer Assisted Design
C_L	Lift coefficient
$C_{Ltarget}$	Target value of the lift coefficient
F_{set}	Thrust setting
F_x	Resulting force on thrust axis
J	Objective function
$\dot{m}_{fuel}$	Fuel mass flow rate
M_∞	Flight Mach number
W	Conservative flow variables
X	Mesh of the fluid domain
α	Angle of attack
α_{geom}	Design parameters
Ω	Design space

A.1 Optimization Problem

A.1.1 Description

The shape optimization problem considered is to minimize the fuel mass flow rate of the engine $\dot{m}_{fuel}$ by acting on the design parameters of the nozzles, denoted α_{geom}. A thermodynamic model of the engine is taken into account. The problem has to respect the following constraints:

- The aerodynamic solver (elsA) and the thermodynamic model of the engine have converged on a set of conditions at their interface.
- The global resulting force on the aircraft is zero: $F_x = 0$.
- The lift of the aircraft is set at a target value: $C_L = C_{Ltarget}$.

A.1.2 Variables and dependencies

The schema in Fig. A.1 summarizes the variables entering each model and their dependencies.

The flight parameters (alt, M_∞) only depend on the flight case considered for the optimization. Consequently, their values are considered unchanged in this study, and will not appear in the derivative calculations.

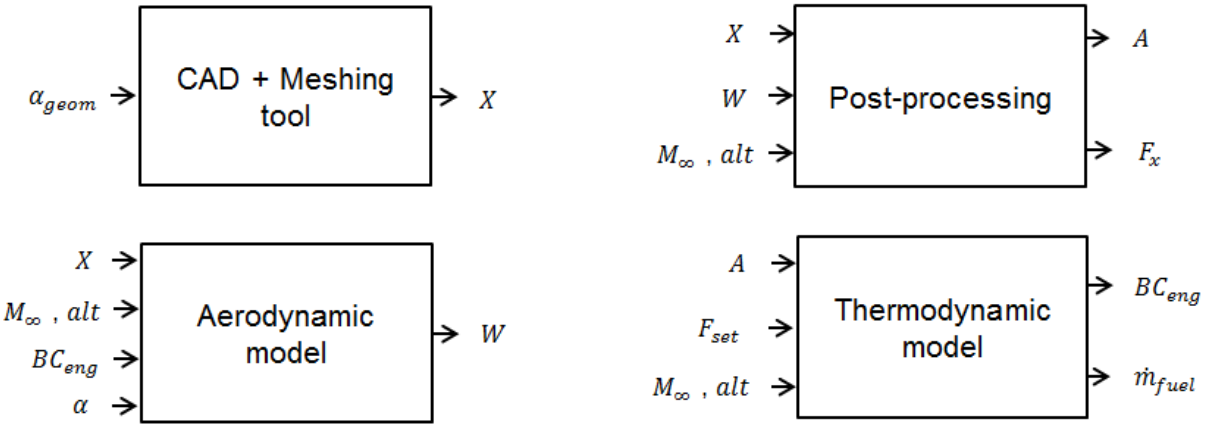

Figure A.1 – *Models and dependencies for the optimization problem*

It must also be noted that the objective function of the optimization is directly the fuel mass flow rate : $J = \dot{m}_{fuel}$ and $J = f(A, F_{set}, (M_\infty, alt))$.

Moreover, the mesh only depends on the geometric design parameters (through CAD and mesh generation): $X(\alpha_{geom})$.

A.1.3 Convergence of the models

Let us consider the equations governing the aerodynamic flow under their residual form, R_a, such that at the convergence:

$$R_a(X, BC_{eng}, W, \alpha) = 0 \tag{A.1}$$

At this point, an assumption is made that for each set of parameters α_{geom} in the design space Ω, a convergence of the aerodynamic computation can be reached : $\forall \alpha_{geom} \in \Omega, R_a = 0$.

Consequently:

$$\frac{dR_a}{d\alpha_{geom}} = 0 \tag{A.2}$$

Similarly, the convergence of the thermodynamic model of the engine can be written as :

$$R_t(BC_{eng}, A, F_{set}) = 0 \tag{A.3}$$

and it is considered that:

$$\frac{dR_t}{d\alpha_{geom}} = 0 \tag{A.4}$$

A.1.4 Coupling between models

For each computation, it is expected to reach an equilibrium between the aerodynamic simulation of the flow around the aircraft and the engine thermodynamic model. This loop is performed by iterating on the variables A and BC_{eng}, as Fig. A.2 shows.

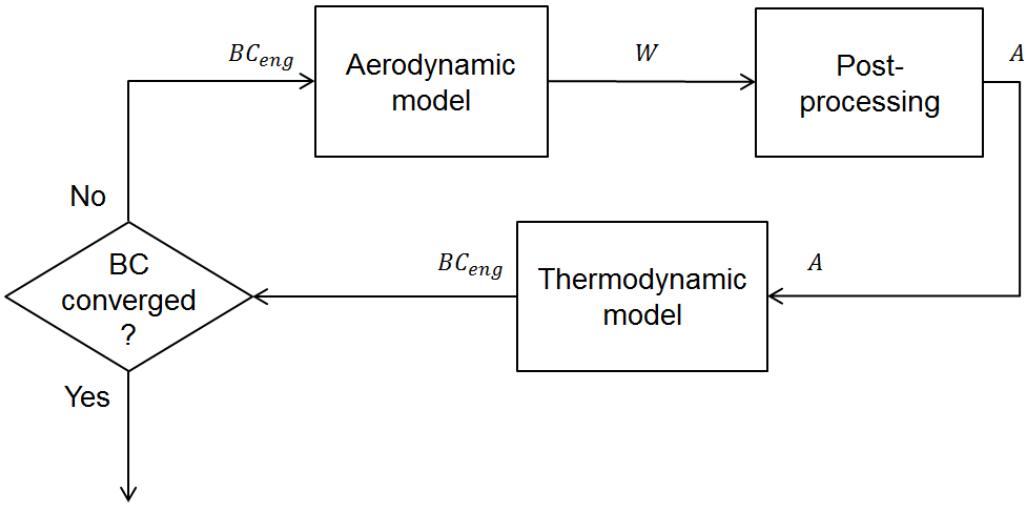

Figure A.2 – *Coupling of the aerodynamic and thermodynamic models*

A.2 Formulation of the gradient of J for frozen F_{set} and α

In this section, the formulation of the gradient will be expressed in the case where only the first coupling between the aerodynamic and thermodynamic models is considered. Thus, in this part, F_{set} and α will not be considered in the derivatives.

A.2.1 Expression of the gradient

The gradient of the objective function can be written, according to its dependencies:

$$\frac{dJ}{d\alpha_{geom}} = \frac{\partial J}{\partial A}\left(\frac{\partial A}{\partial W}\frac{dW}{d\alpha_{geom}} + \frac{\partial A}{\partial X}\frac{dX}{d\alpha_{geom}}\right) \tag{A.5}$$

Differentiating the residual of the aerodynamic equations (Eq. (A.1)) gives:

$$\frac{dR_a}{d\alpha_{geom}} = \frac{\partial R_a}{\partial W}\frac{dW}{d\alpha_{geom}} + \frac{\partial R_a}{\partial BC_{eng}}\frac{dBC_{eng}}{d\alpha_{geom}} + \frac{\partial R_a}{\partial X}\frac{dX}{d\alpha_{geom}} \tag{A.6}$$

A similar approach is used with the residual of the thermodynamic model (Eq. (A.3)). It is reminded that the dependency on F_{set} is not considered in this part. Therefore:

$$\frac{dR_t}{d\alpha_{geom}} = \frac{\partial R_t}{\partial BC_{eng}}\frac{dBC_{eng}}{d\alpha_{geom}} + \frac{\partial R_t}{\partial A}\left(\frac{\partial A}{\partial W}\frac{dW}{d\alpha_{geom}} + \frac{\partial A}{\partial X}\frac{dX}{d\alpha_{geom}}\right) \tag{A.7}$$

Because the derivatives of the residuals are zero quantities (see Eq. (A.2) and (A.4)), they can be multiplied by any couple of non-zero vectors (λ_a, λ_t) and subtracted to Eq. (A.5). This yields:

$$\begin{aligned}\frac{dJ}{d\alpha_{geom}} = &\left(\frac{\partial J}{\partial A}\frac{\partial A}{\partial W} - \lambda_a^T\frac{\partial R_a}{\partial W} - \lambda_t^T\frac{\partial R_t}{\partial A}\frac{\partial A}{\partial W}\right)\frac{dW}{d\alpha_{geom}} \\ &+ \left(\frac{\partial J}{\partial A}\frac{\partial A}{\partial X} - \lambda_a^T\frac{\partial R_a}{dX} - \lambda_t^T\frac{\partial R_t}{\partial A}\frac{\partial A}{\partial X}\right)\frac{dX}{d\alpha_{geom}} \\ &- \left(\lambda_a^T\frac{\partial R_a}{\partial BC_{eng}} + \lambda_t^T\frac{\partial R_t}{\partial BC_{eng}}\right)\frac{dBC_{eng}}{d\alpha_{geom}}\end{aligned} \tag{A.8}$$

In order to eliminate the terms that appear to be the most expensive (in terms of computational time and effort), namely $\frac{dW}{d\alpha_{geom}}$ and $\frac{dBC_{eng}}{d\alpha_{geom}}$, a coupled linear system of two equations is introduced:

$$\begin{cases} \dfrac{\partial J}{\partial A}\dfrac{\partial A}{\partial W} - \lambda_a^T\dfrac{\partial R_a}{dW} - \lambda_t^T\dfrac{\partial R_t}{dA}\dfrac{\partial A}{\partial W} = 0 \\ \lambda_a^T\dfrac{\partial R_a}{\partial BC_{eng}} + \lambda_t^T\dfrac{\partial R_t}{\partial BC_{eng}} = 0 \end{cases} \tag{A.9}$$

The resulting (λ_a, λ_t) are then replaced in the gradient equation that becomes:

$$\frac{dJ}{d\alpha_{geom}} = \left(\frac{\partial J}{\partial A}\frac{\partial A}{\partial X} - \lambda_a^T\frac{\partial R_a}{\partial X} - \lambda_t^T\frac{\partial R_t}{\partial A}\frac{\partial A}{\partial X}\right)\frac{dX}{d\alpha_{geom}} \tag{A.10}$$

A.2.2 Detail of the derivative terms

Several terms appear in the gradient, that must be computed separately in the optimization process. They are detailed in following Table A.1 with a cost evaluation, in order to have a clear perspective of the future work.

Table A.1 – *Summary of the derivative terms for frozen F_{set} and α*

Terms	**Associated tools**	**Method**	**Remark**
$\frac{dX}{d\alpha_{geom}}$	CAD and meshing tools	Finite differences	Time consuming
$\frac{\partial J}{\partial A}$	Thermodynamic model	Finite differences	Low computational cost
$\frac{\partial A}{\partial W}, \frac{\partial A}{\partial X}$	Post-processing tools	Depending on the tools	Hand-made differentiated tools, ...
$\frac{\partial R_t}{\partial A}, \frac{\partial R_t}{\partial BC_{eng}}$	Thermodynamic model	Finite differences	Possibility to compute the residual on a black-box tool?
$\frac{\partial R_a}{\partial W}, \frac{\partial R_a}{\partial BC_{eng}}, \frac{\partial R_a}{\partial X}$	Aerodynamic model (elsA)	Adjoint solver	Computation cost equivalent to CFD

A.3 Formulation of the gradient of J for frozen α

This section will again detail the development of the gradient, but this time the dependencies on F_{set} are taken into account. This new variable is introduced in order to respect the condition of zero-resulting force on the aircraft, which will be discussed in the following section.

A.3.1 Management of the mechanical equilibrium...

To reach an optimal state with a global resulting force on the aircraft equal to zero, several methods can be used. In all cases, it is expected to satisfy this condition using the parameter F_{set}.

The first method possible is to consider the equilibrium as a constraint to be managed by the optimizer. In this case, the gradient of the constraint must be given to the optimizer that would proceed a method of feasible descent.

The second method is to define a second loop, on a higher level than the one described in A.1.4. This would permit to converge with the aerodynamic and thermodynamic models until the mechanical equilibrium is reached. As a consequence, this formulation implies that for each configuration returned to the optimizer the equilibrium is verified.

Both possibilities will be explored in the following parts.

A.3.2 ... As a constraint

The newly introduced parameter F_{set} adds a dependency to the objective function. The gradient of J becomes:

$$\frac{dJ}{d(\alpha_{geom}, F_{set})} = \begin{pmatrix} \dfrac{dJ}{d\alpha_{geom}} \\ \dfrac{dJ}{dF_{set}} \end{pmatrix} \tag{A.11}$$

The first component of this vector can be obtained by the adjoint formulation presented in Section A.2. The second, $\dfrac{dJ}{dF_{set}}$ can be obtained through a finite difference, at the cost of an additional evaluation (or two if a centered scheme is chosen).

Moreover, the optimizer needs the gradient of the constraint with respect to the parameters, which is defined as:

$$\frac{dF_x}{d(\alpha_{geom}, F_{set})} = \begin{pmatrix} \dfrac{dF_x}{d\alpha_{geom}} \\ \dfrac{dF_x}{dF_{set}} \end{pmatrix} \tag{A.12}$$

The first component of this vector can be expressed as:

$$\frac{dF_x}{d\alpha_{geom}} = \frac{\partial F_x}{\partial W}\frac{dW}{d\alpha_{geom}} + \frac{\partial F_x}{\partial X}\frac{dX}{d\alpha_{geom}} \tag{A.13}$$

The same method as in Section A.2 is used to develop Eq.(A.13), introducing two non-zero vectors (μ_a, μ_t):

$$\begin{aligned} \frac{dF_x}{d\alpha_{geom}} = &\left(\frac{\partial F_x}{\partial W} - \mu_a^T\frac{\partial R_a}{\partial W} - \mu_t^T\frac{\partial R_t}{\partial A}\frac{\partial A}{\partial W}\right)\frac{dW}{d\alpha_{geom}} \\ &+ \left(\frac{\partial F_x}{\partial X} - \mu_a^T\frac{\partial R_a}{dX} - \mu_t^T\frac{\partial R_t}{\partial A}\frac{\partial A}{\partial X}\right)\frac{dX}{d\alpha_{geom}} \\ &- \left(\mu_a^T\frac{\partial R_a}{\partial BC_{eng}} + \mu_t^T\frac{\partial R_t}{\partial BC_{eng}}\right)\frac{dBC_{eng}}{d\alpha_{geom}} \end{aligned} \tag{A.14}$$

Again, in order to eliminate the most expensive terms, the following adjoint equations are introduced:

$$\begin{cases} \dfrac{\partial F_x}{\partial W} - \mu_a^T \dfrac{\partial R_a}{\partial W} - \mu_t^T \dfrac{\partial R_t}{\partial A}\dfrac{\partial A}{\partial W} = 0 \\ \mu_a^T \dfrac{\partial R_a}{\partial BC_{eng}} + \mu_t^T \dfrac{\partial R_t}{\partial BC_{eng}} = 0 \end{cases} \tag{A.15}$$

After resolution, (μ_a, μ_t) are injected in Eq. (A.14) and the first component of the gradient of the constraint becomes:

$$\frac{dF_x}{d\alpha_{geom}} = \left(\frac{\partial F_x}{\partial X} - \mu_a^T \frac{\partial R_a}{dX} - \mu_t^T \frac{\partial R_t}{\partial A}\frac{\partial A}{\partial X} \right) \frac{dX}{d\alpha_{geom}} \tag{A.16}$$

The second component of the gradient can be obtained by finite differences,for no additional cost, if we consider that the evaluation to obtain $\dfrac{dJ}{dF_{set}}$ can provide this term too.

To sum up, this method proposes to solve two systems of adjoint equations, associated with the two gradients that must be given to the optimizer. The derivative terms for this formulations are summarized in Table A.2.

Table A.2 – *Summary of the derivative terms when F_{set} is managed as a constraint*

Terms	**Associated tools**	**Method**	**Remark**
$\dfrac{dX}{d\alpha_{geom}}$	CAD and meshing tools	Finite differences	Time consuming
$\dfrac{\partial J}{\partial A}$	Thermodynamic model	Finite differences	Low computational cost
$\dfrac{\partial A}{\partial W}, \dfrac{\partial A}{\partial X}, \dfrac{\partial F_x}{\partial W}, \dfrac{\partial F_x}{\partial X}$	Post-processing tools	Depending on the tools	Hand-made differentiated tools, ...
$\dfrac{\partial R_t}{\partial A}, \dfrac{\partial R_t}{\partial BC_{eng}}$	Thermodynamic model	Finite differences	
$\dfrac{\partial R_a}{\partial W}, \dfrac{\partial R_a}{\partial BC_{eng}}, \dfrac{\partial R_a}{\partial X}$	Aerodynamic model (elsA)	Adjoint solver	Computation cost equivalent to CFD
$\dfrac{dJ}{dF_{set}}, \dfrac{dF_x}{dF_{set}}$	Complete process	Finite differences	Cost of an additional computation with $F'_{set} = F_{set} + h$

A.3.3 ... Through a loop

For this method, the resulting force on the aircraft must be zero at each convergence of the aerodynamic an thermodynamic solvers. The parameter F_{set} is adjusted in order to respect this condition according to a throttle control, that can be interpreted as the action of the pilot of the aircraft. Therefore, it is here considered as a state variable.

Still, this is a parameter of the thermodynamic model as well as A. To include this second coupling, the previous schema can be completed to obtain Fig. A.3

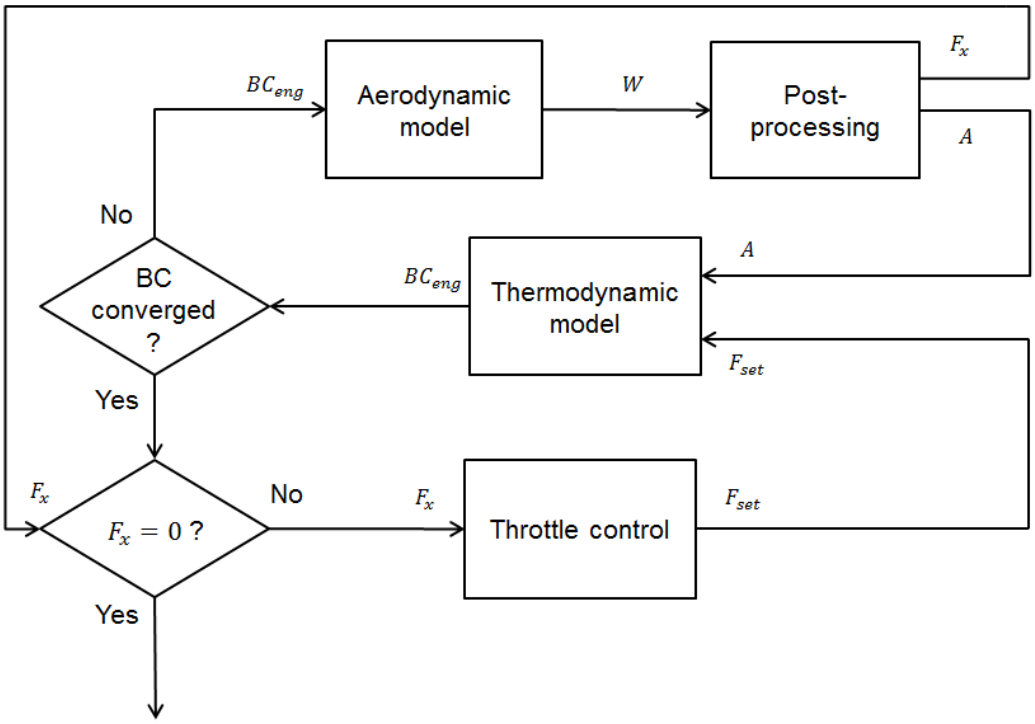

Figure A.3 – *Coupling of the mechanical equilibrium*

A new term appears in the gradient of the objective function:

$$\frac{dJ}{d\alpha_{geom}} = \frac{\partial J}{\partial A}\left(\frac{\partial A}{\partial W}\frac{dW}{d\alpha_{geom}} + \frac{\partial A}{\partial X}\frac{dX}{d\alpha_{geom}}\right) + \frac{\partial J}{\partial F_{set}}\frac{dF_{set}}{d\alpha_{geom}} \tag{A.17}$$

The residual form of the aerodynamic equations (see Eq. (A.1)) does not depend on F_{set}, so its derivative stays unchanged. However, the dependency on F_{set} introduces a new term in the derivative of the thermodynamic residual:

$$\begin{aligned}\frac{dR_t}{d\alpha_{geom}} =& \frac{\partial R_t}{\partial BC_{eng}}\frac{dBC_{eng}}{d\alpha_{geom}} + \frac{\partial R_t}{\partial A}\left(\frac{\partial A}{\partial W}\frac{dW}{d\alpha_{geom}} + \frac{\partial A}{\partial X}\frac{dX}{d\alpha_{geom}}\right) \\ &+ \frac{\partial R_t}{\partial F_{set}}\frac{dF_{set}}{d\alpha_{geom}}\end{aligned} \tag{A.18}$$

Let us take the residual form of the equation governing the throttle control, denoted R_p. At convergence state, one can write:

$$R_p(F_{set}, Fx) = 0 \tag{A.19}$$

Similarly to what has been done with the previous residuals (see Section A.1.3), it is supposed that:

$$\frac{dR_p}{d\alpha_{geom}} = 0 \tag{A.20}$$

This derivative can be expressed as:

$$\frac{dR_p}{d\alpha_{geom}} = \frac{\partial R_p}{\partial F_{set}}\frac{dF_{set}}{d\alpha_{geom}} + \frac{\partial R_p}{\partial F_x}\left(\frac{\partial F_x}{\partial W}\frac{dW}{d\alpha_{geom}} + \frac{\partial F_x}{\partial X}\frac{dX}{d\alpha_{geom}}\right) \tag{A.21}$$

Following the same method as previously and introducing a new non-zero vector λ_p, the derivatives of the residuals are subtracted from the gradient seen in Eq. (A.17):

$$\begin{aligned}\frac{dJ}{d\alpha_{geom}} = &\left(\frac{\partial J}{\partial A}\frac{\partial A}{\partial W} - \lambda_a^T\frac{\partial R_a}{\partial W} - \lambda_t^T\frac{\partial R_t}{\partial A}\frac{\partial A}{\partial W} - \lambda_p^T\frac{\partial R_p}{\partial F_x}\frac{\partial F_x}{\partial W}\right)\frac{dW}{d\alpha_{geom}}\\ &+\left(\frac{\partial J}{\partial A}\frac{\partial A}{\partial X} - \lambda_a^T\frac{\partial R_a}{dX} - \lambda_t^T\frac{\partial R_t}{\partial A}\frac{\partial A}{\partial X} - \lambda_p^T\frac{\partial R_p}{\partial F_x}\frac{\partial F_x}{\partial X}\right)\frac{dX}{d\alpha_{geom}}\\ &-\left(\lambda_a^T\frac{\partial R_a}{\partial BC_{eng}} + \lambda_t^T\frac{\partial R_t}{\partial BC_{eng}}\right)\frac{dBC_{eng}}{d\alpha_{geom}}\\ &+\left(\frac{\partial J}{\partial F_{set}} - \lambda_t^T\frac{\partial R_t}{\partial F_{set}} - \lambda_p^T\frac{\partial R_p}{\partial F_{set}}\right)\frac{dF_{set}}{d\alpha_{geom}}\end{aligned} \tag{A.22}$$

The addition of a new residual implies that there are now three adjoint equations to solve, in order to avoid the most expensive calculations in $\frac{dJ}{d\alpha_{geom}}$:

$$\begin{cases}\dfrac{\partial J}{\partial A}\dfrac{\partial A}{\partial W} - \lambda_a^T\dfrac{\partial R_a}{\partial W} - \lambda_t^T\dfrac{\partial R_t}{\partial A}\dfrac{\partial A}{\partial W} - \lambda_p^T\dfrac{\partial R_p}{\partial F_x}\dfrac{\partial F_x}{\partial W} = 0\\ \lambda_a^T\dfrac{\partial R_a}{\partial BC_{eng}} + \lambda_t^T\dfrac{\partial R_t}{\partial BC_{eng}} = 0\\ \dfrac{\partial J}{\partial F_{set}} - \lambda_t^T\dfrac{\partial R_t}{\partial F_{set}} - \lambda_p^T\dfrac{\partial R_p}{\partial F_{set}} = 0\end{cases} \tag{A.23}$$

After the resolution of this system of coupled linear equations, the solutions $(\lambda_a, \lambda_t, \lambda_p)$ allow the calculation of the gradient, that takes the following form:

$$\frac{dJ}{d\alpha_{geom}} = \left(\frac{\partial J}{\partial A}\frac{\partial A}{\partial X} - \lambda_a^T \frac{\partial R_a}{dX} - \lambda_t^T \frac{\partial R_t}{\partial A}\frac{\partial A}{\partial X} - \lambda_p^T \frac{\partial R_p}{\partial F_x}\frac{\partial F_x}{\partial X} \right) \frac{dX}{d\alpha_{geom}} \tag{A.24}$$

To conclude, this method implies to reach an additional convergence at each optimization step, via throttle control, adding an equation to the adjoint system.

Again, the terms inside the expression of $\frac{dJ}{d\alpha_{geom}}$ are gathered and detailed in TableA.3, with the associated tools and computational cost:

Table A.3 – *Summary of the derivative terms when F_{set} is managed through a loop*

Terms	**Associated tools**	**Method**	**Remark**
$\frac{dX}{d\alpha_{geom}}$	CAD and meshing tools	Finite differences	Time consuming
$\frac{\partial J}{\partial A}, \frac{\partial J}{\partial F_{set}}$	Thermodynamic model	Finite differences	Low computational cost
$\frac{\partial A}{\partial W}, \frac{\partial A}{\partial X}, \frac{\partial F_x}{\partial W}, \frac{\partial F_x}{\partial X}$	Post-processing tools	Depending on the tools	Hand-made differentiated tools, ...
$\frac{\partial R_t}{\partial A}, \frac{\partial R_t}{\partial BC_{eng}}, \frac{\partial R_t}{\partial F_{set}}$	Thermodynamic model	Finite differences	
$\frac{\partial R_a}{\partial W}, \frac{\partial R_a}{\partial BC_{eng}}, \frac{\partial R_a}{\partial X}$	Aerodynamic model (elsA)	Adjoint solver	Computation cost equivalent to CFD
$\frac{\partial R_p}{\partial F_x}, \frac{\partial R_p}{\partial F_{set}}$	Throttle control law	Finite differences or differentiation	Low computational cost

A.4 Formulation of the gradient of J for the complete optimization problem

In this section, the angle of attack of the aircraft is included in the parameters, finalizing this study and giving the complete scope of the optimization problem. Again, the problem is divided into cases, depending on the previous choices made.

A.4.1 Control of the lift coefficient

For the optimization of aircraft in cruise conditions, it is common to conserve the value of the lift coefficient C_L, because it ensures that the result of the process will be comparable to the initial case in terms of flight dynamics. In our study, a degree of freedom α is introduced, namely the angle of attack, to enable the pilot to keep C_L at a constant value $C_{Ltarget}$. Therefore, this new condition can be treated similarly as the condition of zero-resulting force. Two possibilities will be developed in the following sections, that will be:

- Adding a third coupling loop to the optimization problem
- Considering α as a free parameter to be managed by the optimizer

A.4.2 F_x and C_L are managed as constraints

In this section, the assumption is made that the mechanical equilibrium is a constraint for the optimizer, and that the parameter F_{set} is an independant variable of the problem. If the lift coefficient is to be managed as a constraint too, the associated parameter α adds a dependency to the functions J, F_x and to the newly introduced function C_L. The optimizer then needs the sensitivities of the objective function and the constraints with respect to all the parameters, which means:

$$\forall G \in \{J, F_x, C_L\}, \frac{dG}{d(\alpha_{geom}, F_{set}, \alpha)} = \begin{pmatrix} \frac{dG}{d\alpha_{geom}} \\ \frac{dG}{dF_{set}} \\ \frac{dG}{d\alpha} \end{pmatrix} \tag{A.25}$$

The second and third components of these gradients can be obtained through finite differences, at the cost of only one or two additional computation (depending on the scheme chosen).

Still, the sensitivities to α_{geom} are obtained through adjoint equations and need to be written for each differential. As the parameters F_{set} and α do not depend on the variables of the problem, the equations on J and F_x will be the same as in the cases where these parameters were frozen (see Eq. (A.5) and Eq. (A.13)). Introducing two non-zero couples of vectors (λ_a, λ_t) and (μ_a, μ_t) this gives:

$$\begin{aligned}\frac{dJ}{d\alpha_{geom}} = &\left(\frac{\partial J}{\partial A}\frac{\partial A}{\partial W} - \lambda_a^T\frac{\partial R_a}{\partial W} - \lambda_t^T\frac{\partial R_t}{\partial A}\frac{\partial A}{\partial W}\right)\frac{dW}{d\alpha_{geom}} \\ &+ \left(\frac{\partial J}{\partial A}\frac{\partial A}{\partial X} - \lambda_a^T\frac{\partial R_a}{dX} - \lambda_t^T\frac{\partial R_t}{\partial A}\frac{\partial A}{\partial X}\right)\frac{dX}{d\alpha_{geom}} \\ &- \left(\lambda_a^T\frac{\partial R_a}{\partial BC_{eng}} + \lambda_t^T\frac{\partial R_t}{\partial BC_{eng}}\right)\frac{dBC_{eng}}{d\alpha_{geom}}\end{aligned} \tag{A.26}$$

$$\begin{aligned}\frac{dF_x}{d\alpha_{geom}} = &\left(\frac{\partial F_x}{\partial W} - \mu_a^T\frac{\partial R_a}{\partial W} - \mu_t^T\frac{\partial R_t}{\partial A}\frac{\partial A}{\partial W}\right)\frac{dW}{d\alpha_{geom}} \\ &+ \left(\frac{\partial F_x}{\partial X} - \mu_a^T\frac{\partial R_a}{dX} - \mu_t^T\frac{\partial R_t}{\partial A}\frac{\partial A}{\partial X}\right)\frac{dX}{d\alpha_{geom}} \\ &- \left(\mu_a^T\frac{\partial R_a}{\partial BC_{eng}} + \mu_t^T\frac{\partial R_t}{\partial BC_{eng}}\right)\frac{dBC_{eng}}{d\alpha_{geom}}\end{aligned} \tag{A.27}$$

The gradient of C_L with respect to design parameters can be decomposed in:

$$\frac{dC_L}{d\alpha_{geom}} = \frac{\partial C_L}{\partial W}\frac{dW}{d\alpha_{geom}} + \frac{\partial C_L}{\partial X}\frac{dX}{d\alpha_{geom}} \tag{A.28}$$

Introducing a third non-zero couple of vectors $(\gamma_a, \gamma t)$, the gradients of the residuals are subtracted to Eq. (A.28):

$$\begin{aligned}\frac{dC_L}{d\alpha_{geom}} = &\left(\frac{\partial C_L}{\partial W} - \gamma_a^T\frac{\partial R_a}{\partial W} - \gamma_t^T\frac{\partial R_t}{\partial A}\frac{\partial A}{\partial W}\right)\frac{dW}{d\alpha_{geom}} \\ &+ \left(\frac{\partial C_L}{\partial X} - \gamma_a^T\frac{\partial R_a}{dX} - \gamma_t^T\frac{\partial R_t}{\partial A}\frac{\partial A}{\partial X}\right)\frac{dX}{d\alpha_{geom}} \\ &- \left(\gamma_a^T\frac{\partial R_a}{\partial BC_{eng}} + \gamma_t^T\frac{\partial R_t}{\partial BC_{eng}}\right)\frac{dBC_{eng}}{d\alpha_{geom}}\end{aligned} \tag{A.29}$$

As a consequence, to eliminate the undesired terms of these expressions, this method implies to solve three adjoint systems of coupled linear equations:

$$\begin{cases} \dfrac{\partial J}{\partial A}\dfrac{\partial A}{\partial W} - \lambda_a^T\dfrac{\partial R_a}{dW} - \lambda_t^T\dfrac{\partial R_t}{dA}\dfrac{\partial A}{\partial W} = 0 \\ \lambda_a^T\dfrac{\partial R_a}{\partial BC_{eng}} + \lambda_t^T\dfrac{\partial R_t}{\partial BC_{eng}} = 0 \end{cases} \tag{A.30}$$

$$\begin{cases} \dfrac{\partial F_x}{\partial W} - \mu_a^T\dfrac{\partial R_a}{dW} - \mu_t^T\dfrac{\partial R_t}{dA}\dfrac{\partial A}{\partial W} = 0 \\ \mu_a^T\dfrac{\partial R_a}{\partial BC_{eng}} + \mu_t^T\dfrac{\partial R_t}{\partial BC_{eng}} = 0 \end{cases} \tag{A.31}$$

$$\begin{cases} \dfrac{\partial C_L}{\partial W} - \gamma_a^T \dfrac{\partial R_a}{dW} - \gamma_t^T \dfrac{\partial R_t}{dA}\dfrac{\partial A}{\partial W} = 0 \\ \gamma_a^T \dfrac{\partial R_a}{\partial BC_{eng}} + \gamma_t^T \dfrac{\partial R_t}{\partial BC_{eng}} = 0 \end{cases} \tag{A.32}$$

It can be noticed that the second equation of each of these systems are identical. The resulting couples of vectors can then be replaced in the formulas of the sensitivities:

$$\frac{dJ}{d\alpha_{geom}} = \left(\frac{\partial J}{\partial A}\frac{\partial A}{\partial X} - \lambda_a^T \frac{\partial R_a}{dX} - \lambda_t^T \frac{\partial R_t}{\partial A}\frac{\partial A}{\partial X} \right) \frac{dX}{d\alpha_{geom}} \tag{A.33}$$

$$\frac{dF_x}{d\alpha_{geom}} = \left(\frac{\partial F_x}{\partial X} - \mu_a^T \frac{\partial R_a}{dX} - \mu_t^T \frac{\partial R_t}{\partial A}\frac{\partial A}{\partial X} \right) \frac{dX}{d\alpha_{geom}} \tag{A.34}$$

$$\frac{dC_L}{d\alpha_{geom}} = \left(\frac{\partial C_L}{\partial X} - \gamma_a^T \frac{\partial R_a}{dX} - \gamma_t^T \frac{\partial R_t}{\partial A}\frac{\partial A}{\partial X} \right) \frac{dX}{d\alpha_{geom}} \tag{A.35}$$

The terms that have to be computed in this case are detailed in Table A.4.

A.4.3 F_x is controlled through a loop and C_L is managed as a constraint

For this section, it is considered that the mechanical equilibrium is reached through a loop, similarly to the convergence on the boundary conditions between the aerodynamic and thermodynamic models. The respect of a target value of C_L, however, is given as a constraint to the optimizer and the angle of attack of the aircraft is defined as a parameter. As a consequence, the optimizer needs the sensitivities of the objective function and the constraint with respect to all parameters, that are written as follow :

$$\forall G \in \{J, C_L\}, \frac{dG}{d(\alpha_{geom}, \alpha)} = \begin{pmatrix} \dfrac{dG}{d\alpha_{geom}} \\ \dfrac{dG}{d\alpha} \end{pmatrix} \tag{A.36}$$

The first component of these vectors is obtained from the adjoint formulation of two coupling loops and must be detailed in the following equations. The second component results from an additional computation for finite differences.

Because two coupling loops are taken into account, the adjoint equations to solve to obtain the sensitivity of J are the same as in Section A.3.3:

Table A.4 – *Summary of the derivative terms when F_{set} and $alpha$ are managed as constraints*

Terms	**Associated tools**	**Method**	**Remark**
$\frac{dX}{d\alpha_{geom}}$	CAD and meshing tools	Finite differences	Time consuming
$\frac{\partial J}{\partial A}, \frac{\partial J}{\partial F_{set}}$	Thermodynamic model	Finite differences	Low computational cost
$\frac{\partial A}{\partial W}, \frac{\partial A}{\partial X}, \frac{\partial F_x}{\partial W}, \frac{\partial F_x}{\partial X}, \frac{\partial C_L}{\partial W}, \frac{\partial C_L}{\partial X}$	Post-processing tools	Depending on the tools	Hand-made differentiated tools, ...
$\frac{\partial R_t}{\partial A}, \frac{\partial R_t}{\partial BC_{eng}}, \frac{\partial R_t}{\partial F_{set}}$	Thermodynamic model	Finite differences	
$\frac{\partial R_a}{\partial W}, \frac{\partial R_a}{\partial BC_{eng}}, \frac{\partial R_a}{\partial X}$	Aerodynamic model (elsA)	Adjoint solver	Computation cost equivalent to CFD
$\frac{\partial R_p}{\partial F_x}, \frac{\partial R_p}{\partial F_{set}}$	Throttle control law	Finite differences or differentiation	Low computational cost
$\frac{dJ}{dF_{set}}, \frac{dF_x}{dF_{set}}, \frac{dC_L}{dF_{set}}$	Complete process	Finite differences	Cost of an additional computation with $F'_{set} = F_{set} + h$
$\frac{dJ}{d\alpha}, \frac{dF_x}{d\alpha}, \frac{dC_L}{d\alpha}$	Complete process	Finite differences	Cost of an additional computation with $\alpha' = \alpha + h$

$$\begin{cases} \dfrac{\partial J}{\partial A}\dfrac{\partial A}{\partial W} - \lambda_a^T\dfrac{\partial R_a}{\partial W} - \lambda_t^T\dfrac{\partial R_t}{\partial A}\dfrac{\partial A}{\partial W} - \lambda_p^T\dfrac{\partial R_p}{\partial F_x}\dfrac{\partial F_x}{\partial W} = 0 \\ \lambda_a^T\dfrac{\partial R_a}{\partial BC_{eng}} + \lambda_t^T\dfrac{\partial R_t}{\partial BC_{eng}} = 0 \\ \dfrac{\partial J}{\partial F_{set}} - \lambda_t^T\dfrac{\partial R_t}{\partial F_{set}} - \lambda_p^T\dfrac{\partial R_p}{\partial F_{set}} = 0 \end{cases} \tag{A.37}$$

and

$$\frac{dJ}{d\alpha_{geom}} = \left(\frac{\partial J}{\partial A}\frac{\partial A}{\partial X} - \lambda_a^T\frac{\partial R_a}{dX} - \lambda_t^T\frac{\partial R_t}{\partial A}\frac{\partial A}{\partial X} - \lambda_p^T\frac{\partial R_p}{\partial F_x}\frac{\partial F_x}{\partial X}\right)\frac{dX}{d\alpha_{geom}} \tag{A.38}$$

On the other hand, the gradient of the lift coefficient is decomposed as in Eq. (A.28). This time, the residual of the aerodynamic model depends on α (see Eq.(A.1)), but as an independent parameter, it does not appear in the gradient of R_a. After subtraction of the gradients of the three residuals forms (R_a, R_t, R_p) the following expression is obtained:

$$\begin{aligned}\frac{dC_L}{d\alpha_{geom}} = &\left(\frac{\partial C_L}{\partial W} - \gamma_a^T\frac{\partial R_a}{\partial W} - \gamma_t^T\frac{\partial R_t}{\partial A}\frac{\partial A}{\partial W} - \gamma_p^T\frac{\partial R_p}{\partial F_x}\frac{\partial F_x}{\partial W}\right)\frac{dW}{d\alpha_{geom}}\\ &+\left(\frac{\partial C_L}{\partial W} - \gamma_a^T\frac{\partial R_a}{dX} - \gamma_t^T\frac{\partial R_t}{\partial A}\frac{\partial A}{\partial X} - \gamma_p^T\frac{\partial R_p}{\partial F_x}\frac{\partial F_x}{\partial X}\right)\frac{dX}{d\alpha_{geom}}\\ &-\left(\gamma_a^T\frac{\partial R_a}{\partial BC_{eng}} + \gamma_t^T\frac{\partial R_t}{\partial BC_{eng}}\right)\frac{dBC_{eng}}{d\alpha_{geom}}\\ &-\left(\gamma_t^T\frac{\partial R_t}{\partial F_{set}} + \gamma_p^T\frac{\partial R_p}{\partial F_{set}}\right)\frac{dF_{set}}{d\alpha_{geom}}\end{aligned} \tag{A.39}$$

assuming that $(\gamma_a, \gamma_t, \gamma_p)$ are non-zero vectors. This yields a new adjoint sytem to solve, in order to eliminate the undesired terms:

$$\begin{cases}\dfrac{\partial C_L}{\partial W} - \gamma_a^T\dfrac{\partial R_a}{\partial W} - \gamma_t^T\dfrac{\partial R_t}{\partial A}\dfrac{\partial A}{\partial W} - \gamma_p^T\dfrac{\partial R_p}{\partial F_x}\dfrac{\partial F_x}{\partial W} = 0\\ \gamma_a^T\dfrac{\partial R_a}{\partial BC_{eng}} + \gamma_t^T\dfrac{\partial R_t}{\partial BC_{eng}} = 0\\ \gamma_t^T\dfrac{\partial R_t}{\partial F_{set}} - \gamma_p^T\dfrac{\partial R_p}{\partial F_{set}} = 0\end{cases} \tag{A.40}$$

Once this system is solved, the sensitivity of the lift coefficient becomes:

$$\frac{dC_L}{d\alpha_{geom}} = \left(\frac{\partial C_L}{\partial X} - \gamma_a^T\frac{\partial R_a}{dX} - \gamma_t^T\frac{\partial R_t}{\partial A}\frac{\partial A}{\partial X} - \gamma_p^T\frac{\partial R_p}{\partial F_x}\frac{\partial F_x}{\partial X}\right)\frac{dX}{d\alpha_{geom}} \tag{A.41}$$

To sum up, this method implies the resolution of two adjoint systems of three equations, at each gradient iteration of the optimization process. The derivative terms that appear in this case are detailed in Table A.5.

A.4.4 F_x and C_L are controlled through loops

In this final section, the third and last alternative to solve the complete optimization problem is explained. It is assumed that the thrust-drag equilibrium is obtained with throttle control through a loop. A third loop is introduced for the angle of attack control, to maintain C_L at a given value. The resulting problem is illustrated on Fig. A.4.

The gradient of the objective function is :

Table A.5 – *Summary of the derivative terms when F_{set} is managed through a loop and $alpha$ is managed as constraints*

Terms	**Associated tools**	**Method**	**Remark**
$\frac{dX}{d\alpha_{geom}}$	CAD and meshing tools	Finite differences	Time consuming
$\frac{\partial J}{\partial A}, \frac{\partial J}{\partial F_{set}}$	Thermodynamic model	Finite differences	Low computational cost
$\frac{\partial A}{\partial W}, \frac{\partial A}{\partial X}, \frac{\partial F_x}{\partial W}, \frac{\partial F_x}{\partial X}, \frac{\partial C_L}{\partial W}, \frac{\partial C_L}{\partial X}$	Post-processing tools	Depending on the tools	Hand-made differentiated tools, ...
$\frac{\partial R_t}{\partial A}, \frac{\partial R_t}{\partial BC_{eng}}, \frac{\partial R_t}{\partial F_{set}}$	Thermodynamic model	Finite differences	
$\frac{\partial R_a}{\partial W}, \frac{\partial R_a}{\partial BC_{eng}}, \frac{\partial R_a}{\partial X}$	Aerodynamic model (elsA)	Adjoint solver	Computation cost equivalent to CFD
$\frac{\partial R_p}{\partial F_x}, \frac{\partial R_p}{\partial F_{set}}$	Throttle control law	Finite differences or differentiation	Low computational cost
$\frac{dJ}{d\alpha}, \frac{dC_L}{d\alpha}$	Complete process	Finite differences	Cost of an additional computation with $\alpha' = \alpha + h$

$$\frac{dJ}{d\alpha_{geom}} = \frac{\partial J}{\partial A}\left(\frac{\partial A}{\partial W}\frac{dW}{d\alpha_{geom}} + \frac{\partial A}{\partial X}\frac{dX}{d\alpha_{geom}}\right) + \frac{\partial J}{\partial F_{set}}\frac{dF_{set}}{d\alpha_{geom}} \tag{A.42}$$

The equation governing the control of the angle of attack is written under its residual form :

$$R_l(C_L, \alpha) = 0 \tag{A.43}$$

At convergence :

$$\frac{dR_l}{d\alpha_{geom}} = 0 \tag{A.44}$$

As α has been introduced, the dependency of R_a with respect to it must now be taken into account. The residual forms of the equations (introduced in the previous

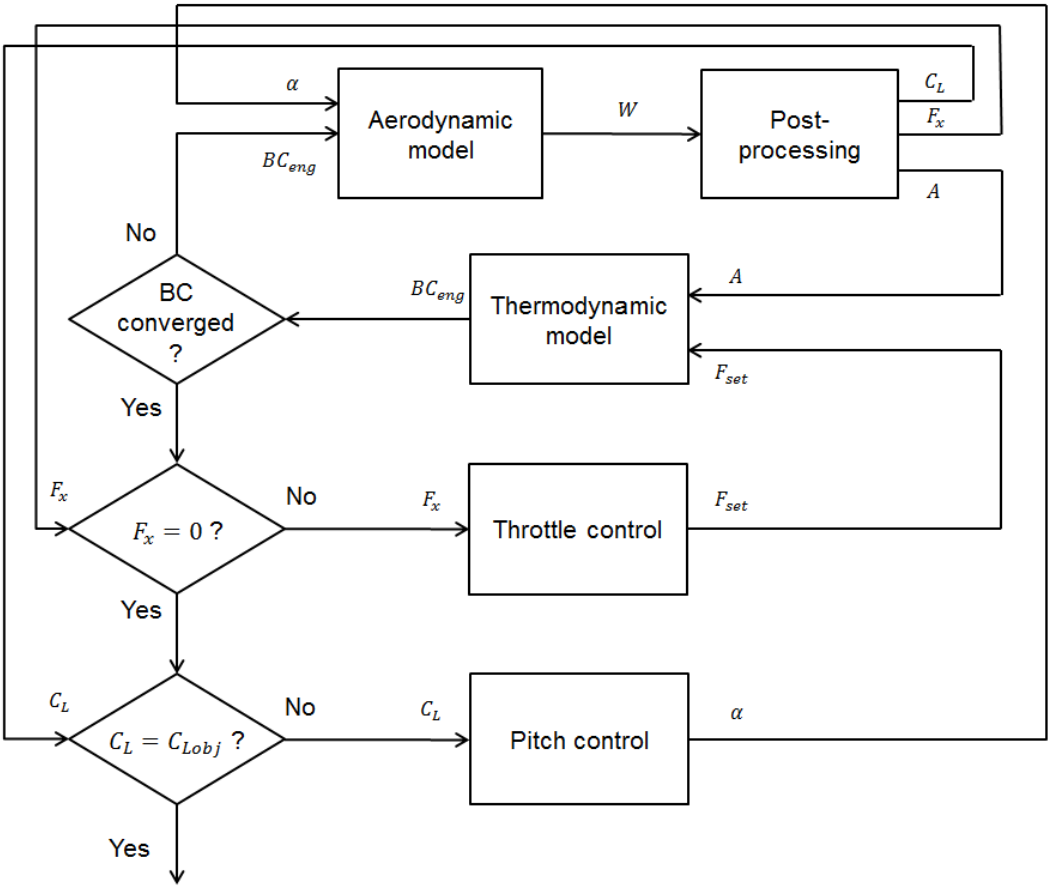

Figure A.4 – *Coupling with throttle and aoa control*

sections) are differentiated with respect to α_{geom} and become :

$$\frac{dR_a}{d\alpha_{geom}} = \frac{\partial R_a}{\partial W}\frac{dW}{d\alpha_{geom}} + \frac{\partial R_a}{\partial BC_{eng}}\frac{dBC_{eng}}{d\alpha_{geom}} + \frac{\partial R_a}{\partial X}\frac{dX}{d\alpha_{geom}} + \frac{\partial R_a}{\partial \alpha}\frac{d\alpha}{d\alpha_{geom}} \tag{A.45}$$

$$\begin{aligned}\frac{dR_t}{d\alpha_{geom}} =& \frac{\partial R_t}{\partial BC_{eng}}\frac{dBC_{eng}}{d\alpha_{geom}} + \frac{\partial R_t}{\partial A}\left(\frac{\partial A}{\partial W}\frac{dW}{d\alpha_{geom}} + \frac{\partial A}{\partial X}\frac{dX}{d\alpha_{geom}}\right) \\ &+ \frac{\partial R_t}{\partial F_{set}}\frac{dF_{set}}{d\alpha_{geom}}\end{aligned} \tag{A.46}$$

$$\frac{dR_p}{d\alpha_{geom}} = \frac{\partial R_p}{\partial F_{set}}\frac{dF_{set}}{d\alpha_{geom}} + \frac{\partial R_p}{\partial F_x}\left(\frac{\partial F_x}{\partial W}\frac{dW}{d\alpha_{geom}} + \frac{\partial F_x}{\partial X}\frac{dX}{d\alpha_{geom}}\right) \tag{A.47}$$

$$\frac{dR_l}{d\alpha_{geom}} == \frac{\partial R_l}{\partial C_L}\frac{dC_L}{d\alpha_{geom}} + \frac{\partial R_l}{\partial \alpha}\left(\frac{\partial \alpha}{\partial W}\frac{dW}{d\alpha_{geom}} + \frac{\partial \alpha}{\partial X}\frac{dX}{d\alpha_{geom}}\right) \tag{A.48}$$

Introducing non zero vectors (λ_a,λ_t,λ_p,λ_l), it is convenient to subtract these null differentials from the expression of the gradient of J:

$$\begin{aligned}\frac{dJ}{d\alpha_{geom}} = &\left(\frac{\partial J}{\partial A}\frac{\partial A}{\partial W} - \lambda_a^T\frac{\partial R_a}{\partial W} - \lambda_t^T\frac{\partial R_t}{\partial A}\frac{\partial A}{\partial W} - \lambda_p^T\frac{\partial R_p}{\partial F_x}\frac{\partial F_x}{\partial W} - \lambda_l^T\frac{\partial R_l}{\partial C_L}\frac{\partial C_L}{\partial W}\right)\frac{dW}{d\alpha_{geom}}\\ &+\left(\frac{\partial J}{\partial A}\frac{\partial A}{\partial X} - \lambda_a^T\frac{\partial R_a}{dX} - \lambda_t^T\frac{\partial R_t}{\partial A}\frac{\partial A}{\partial X} - \lambda_p^T\frac{\partial R_p}{\partial F_x}\frac{\partial F_x}{\partial X} - \lambda_l^T\frac{\partial R_l}{\partial C_L}\frac{\partial C_L}{\partial X}\right)\frac{dX}{d\alpha_{geom}}\\ &-\left(\lambda_a^T\frac{\partial R_a}{\partial BC_{eng}} + \lambda_t^T\frac{\partial R_t}{\partial BC_{eng}}\right)\frac{dBC_{eng}}{d\alpha_{geom}}\\ &+\left(\frac{\partial J}{\partial F_{set}} - \lambda_t^T\frac{\partial R_t}{\partial F_{set}} - \lambda_p^T\frac{\partial R_p}{\partial F_{set}}\right)\frac{dF_{set}}{d\alpha_{geom}}\\ &-\left(\lambda_a^T\frac{\partial R_a}{\partial \alpha} + \lambda_l^T\frac{\partial R_l}{\partial \alpha}\right)\frac{d\alpha}{d\alpha_{geom}}\end{aligned} \tag{A.49}$$

Thanks to the four vectors introduced, it is possible to eliminate the terms of the gradient that are not computable. Therefore, four coupled adjoint equations appear:

$$\begin{cases}\dfrac{\partial J}{\partial A}\dfrac{\partial A}{\partial W} - \lambda_a^T\dfrac{\partial R_a}{\partial W} - \lambda_t^T\dfrac{\partial R_t}{\partial A}\dfrac{\partial A}{\partial W} - \lambda_p^T\dfrac{\partial R_p}{\partial F_x}\dfrac{\partial F_x}{\partial W} - \lambda_l^T\dfrac{\partial R_l}{\partial C_L}\dfrac{\partial C_L}{\partial W} = 0\\ \lambda_a^T\dfrac{\partial R_a}{\partial BC_{eng}} + \lambda_t^T\dfrac{\partial R_t}{\partial BC_{eng}} = 0\\ \dfrac{\partial J}{\partial F_{set}} - \lambda_t^T\dfrac{\partial R_t}{\partial F_{set}} - \lambda_p^T\dfrac{\partial R_p}{\partial F_{set}} = 0\\ \lambda_a^T\dfrac{\partial R_a}{\partial \alpha} + \lambda_l^T\dfrac{\partial R_l}{\partial \alpha} = 0\end{cases} \tag{A.50}$$

With the solutions of this adjoint system, the gradient of the objective function can finally be expressed as follows:

$$\frac{dJ}{d\alpha_{geom}} = \left(\frac{\partial J}{\partial A}\frac{\partial A}{\partial X} - \lambda_a^T\frac{\partial R_a}{dX} - \lambda_t^T\frac{\partial R_t}{\partial A}\frac{\partial A}{\partial X} - \lambda_p^T\frac{\partial R_p}{\partial F_x}\frac{\partial F_x}{\partial X} - \lambda_l^T\frac{\partial R_l}{\partial C_L}\frac{\partial C_L}{\partial X}\right)\frac{dX}{d\alpha_{geom}} \tag{A.51}$$

The computation requires the evaluation of numerous terms, summed up in TableA.6.

A.5 Outcome

This document presents a study establishing the adjoint equations for an optimization problem improving the performance of under-wing mounted turbofan nozzles. The equations are established step-by-step and different options are present in order to

Table A.6 – *Summary of the derivative terms when F_{set} and $alpha$ are managed through coupling loops*

Terms	**Associated tools**	**Method**	**Remark**
$\frac{dX}{d\alpha_{geom}}$	CAD and meshing tools	Finite differences	Time consuming
$\frac{\partial J}{\partial A}, \frac{\partial J}{\partial F_{set}}$	Thermodynamic model	Finite differences	Low computational cost
$\frac{\partial A}{\partial W}, \frac{\partial A}{\partial X}, \frac{\partial F_x}{\partial W}, \frac{\partial F_x}{\partial X}, \frac{\partial C_L}{\partial W}, \frac{\partial C_L}{\partial X}$	Post-processing tools	Depending on the tools	Hand-made differentiated tools, ...
$\frac{\partial R_t}{\partial A}, \frac{\partial R_t}{\partial BC_{eng}}, \frac{\partial R_t}{\partial F_{set}}$	Thermodynamic model	Finite differences	
$\frac{\partial R_a}{\partial W}, \frac{\partial R_a}{\partial BC_{eng}}, \frac{\partial R_a}{\partial X}, \frac{\partial R_a}{\partial \alpha}$	Aerodynamic model (elsA)	Adjoint solver	Computation cost equivalent to CFD
$\frac{\partial R_p}{\partial F_x}, \frac{\partial R_p}{\partial F_{set}}$	Throttle control law	Finite differences or differentiation	Low computational cost
$\frac{\partial R_l}{\partial C_L}, \frac{\partial R_l}{\partial \alpha}$	Angle of attack control law	Finite differences or differentiation	Low computational cost

manage the couplings of this problem. Thanks to this, the derivative terms of this formulation can be discussed. In particular, two terms appear challenging from the author's point of view that concern the geometry generation and the post-processing tools.

First, the mesh sensitivities to design parameters should be computed through finite differences. This represents a time-consuming process, with a rapidly increasing cost for high number of variables. Consequently, such process mitigates the benefit of adjoint-based gradient computations. Moreover, geometry sensitivies must be computed carefully with CAD and mesh "black-box" software, as they can have a discontinuous behavior.

Then, post-processing tools must be defined in agreement with the problem studied. In this case, a dedicated code must be developed to handle speficic nozzle post-processing and enable the coupling with the thermodynamic model. However, integrating such tool in an adjoint process represents an additional challenge, namely the differentiation of the code. As the differentiation by-hand is far from begin trivial, this can become a major bottleneck for the application of the adjoint method.

Last but not least, this document shows that the challenging terms discussed above appear without considering any coupling. They are inherent to the optimization workflow chosen for this case, and must be tackled right before considering any further dependency.

B

List of publications

This appendix presents participations to scientific conferences, publications and communications related to the present thesis work.

Participations to scientific conferences

- S. Bagy, B. Mohammadi, M. Méheut, M. Lallia, and P. Coat. Towards CAD-based shape optimization of aircraft engine nozzles. In *EUROGEN Conference*, 2019.
- S. Bagy, B. Mohammadi, M. Méheut, M. Lallia, and P. Coat. Aerodynamic shape optimization of aircraft engine nozzles based on computer-aided design. In *AIAA Scitech 2020 Forum*, https://doi.org/10.2514/6.2020-2247.

Technical reports

- First and second-year reports

Other communications

- "Ma thèse en 180 secondes"-like pitch, Safran R&T Days, 2019
- Journées des doctorants ONERA, 2018 - 2020
- Journées des doctorants SAFRAN, 2017 - 2019

C

Résumé de la thèse

Contexte

La réduction de l'empreinte écologique du transport aérien est un enjeu majeur pour le secteur aéronautique. Ainsi, les moteurs de type « turbofan » destinés à l'aviation civile suivent une tendance d'accroissement de leur taux de dilution (ou BPR[1]), qui est favorable à la réduction de leur consommation de carburant. En pratique, cette augmentation du BPR s'accompagne généralement d'un agrandissement du diamètre de la soufflante et de la nacelle. Compte tenu des contraintes d'intégration lorsque les moteurs sont installés sous les ailes des aéronefs, cela peut conduire à un renforcement des interactions aérodynamiques entre le système propulsif et la voilure, aussi appelées « effets d'installation ». En particulier, l'arrière-corps des moteurs à double flux séparés, comprenant les tuyères des flux primaire et secondaire, est situé à proximité de l'intrados de la voilure et est par conséquent directement concerné par ces interactions. Les tuyères sont des organes essentiels pour la performance et l'opérabilité du moteur, c'est pourquoi il est pertinent d'améliorer la prise en compte des interactions aérodynamiques entre le moteur et la voilure dès les phases de conception préliminaires de l'arrière-corps.

Objectifs

L'enjeu principal de ce projet a consisté à développer une approche de conception des formes aérodynamiques de tuyères, qui soit capable de mieux tenir compte des interactions aérodynamiques moteur / voilure, voire d'en tirer profit. Dans cette optique, un processus d'optimisation de formes aérodynamiques a été mis en place. Ce proces-

[1] By-Pass Ratio : rapport de débit masse entre le flux froid et le flux chaud du moteur

sus s'appuie sur des simulations CFD[2] tridimensionnelles, afin de décrire l'écoulement complexe ayant lieu autour de la nacelle. Pour permettre la génération de formes complexes d'arrière-corps, des modèles géométriques basés sur des outils CAO[3] sont utilisés. Les modèles paramétrés employés en bureaux d'études industriels comprennent généralement des centaines de variables de dessin. De plus, afin de tenir compte de l'interdépendance entre la performance des tuyères et les cycle thermodynamique du moteur, des calculs aéro-propulsifs couplés ont été mis en place.

Dans la littérature, parmi les travaux appliquant des méthodes d'optimisation pour le dessin des nacelles de moteurs, on remarque une étude menée par Goulos et al.[25]. A l'aide d'optimisations basées sur des modèles de substitution (SBO[4]), ces travaux permettent d'améliorer la force propulsive en modifiant les formes d'arrière-corps de moteurs turbofan double-flux. Néanmoins, cette étude ne considère que des géométries 2D et ne prend pas en compte les effets d'installation.
Une autre étude, menée par Gray et al.[29], s'avère intéressante dans le cadre de nos travaux. Des optimisations y sont mises en oeuvre pour améliorer la performance d'un moteur à ingestion de couche limite, situé sous l'empennage d'un aéronef. En particulier, un modèle thermodynamique de moteur est introduit, qui permet d'effectuer des simulations couplées aéro-propulsives et d'évaluer la performance de l'ensemble. Cependant, cette étude n'utilise pas des outils de dessin adaptés aux usages des bureaux d'études industriels.
Par rapport à ces exemples, la spécificité du travail de thèse est qu'il vise à développer des méthodes de conception aérodynamique de tuyères basées sur des optimisations de formes, tout en s'appuyant sur des modèles de dessin industriel (CAO) à grands nombres de paramètres et des simulations aéro-propulsives couplées.

Démarche et résultats principaux

Dans un premier temps, notre étude a consisté à déterminer une approche adaptée pour mener des optimisations compte tenu des contraintes du sujet. Une étude bibliographique des méthodes d'optimisation existantes a montré que l'utilisation de modèles CAO à grands nombres de paramètres est particulièrement limitante vis à vis du choix de méthodes d'optimisation. Les méthodes d'ordre zéro, ne nécessitant pas de calcul de gradient, nécessitent souvent un grand nombre d'évaluations pour converger. Ce coût augmente rapidement en fonction du nombre de variables de dessin, et rend ces algorithmes inutilisables pour des centaines de paramètres. Par ailleurs, les méthodes du premier ordre évoluent grâce aux gradients des grandeurs d'intérêt. Dans le cas où le gradient est calculé par différences finies, son évaluation a un coût proportionnel au nombre de variables. Pour des centaines de variables de dessin et un processus impliquant des calculs CFD, ce coût devient limitant. Une méthode alternative de calcul du gradient, appelée *méthode adjointe*, est souvent utilisée pour l'optimisation de formes aérodynamiques. Cette méthode permet de calculer le gradient à un coût indépendant du nombre de variables impliquées, mais nécessite d'accéder aux termes

[2]Computational Fluid Dynamics
[3]Conception Assistée par Ordinateur
[4]Surrogate-Based Optimizations

dérivatifs des outils composant le processus. Par conséquent, l'intégration de logiciels CAO non-différentiés, tels que celui utilisé pour notre étude, au sein d'un processus d'optimisation par adjoint mène à de nombreuses difficultés techniques.
Dans cette situation, il apparaît nécessaire de développer dans le cadre de notre projet une méthode afin de concilier l'optimisation et la CAO. C'est pourquoi nous proposons une approche originale et innovante, basée sur une paramétrisation par *combinaison convexe*. Afin de diminuer la dimension du problème, la recherche d'optimum s'effectue dans un espace défini par combinaison de configurations « expert » fournies par le concepteur. Ainsi, le problème est ramené à un nombre de paramètres réduit permettant d'envisager des optimisations par des méthodes avec ou sans gradients, pour un coût de calcul raisonnable. De plus, le savoir-faire du concepteur est intégré au processus d'optimisation, et réduit le risque de générer des formes optimisées non-acceptables / non-industrialisables. En outre, cette méthode est une façon efficace pour mener l'exploration d'un espace de design complexe et son résultat peut servir de point de départ pour des optimisations sur l'espace complet.

L'approche par combinaison convexe a ensuite été appliquée à des cas de complexité croissante. Tout d'abord, une étude a été menée sur une nacelle monoflux, sans corps central et isolée. L'objectif de ce cas a été de valider l'approche par combinaison convexe avec un premier processus d'optimisation basé sur des simulations CFD, tout en restant comparable à la théorie des tuyères. Pour ce cas de démonstration, la CAO n'est pas encore impliquée et une déformation de maillage est utilisée. L'objectif est de maximiser la résultante des efforts sur la nacelle, pour des conditions motrices données. Une optimisation sous contrainte de débit est donc effectuée à l'aide d'une méthode de descente admissible (avec l'optimiseur Dakota [1]) et en calculant les gradients par différences finies. De plus, des optimisations ont été faites sur l'espace de design complet ainsi que sur des sous-espaces définis par combinaison convexe, afin de permettre la comparaison.
D'abord, les simulations sont effectuées en résolvant les équations de fluide non-visqueux (Euler). En proposant trois formes « expert » , il apparaît que l'optimisation effectuée sur l'espace généré par combinaison convexe aboutit à une forme de tuyère plus performante que l'exploration de l'espace de design complet. Ainsi, ce résultat suggère que la prise en compte des formes « expert » permet de générer un sous-espace d'intérêt et aide l'optimiseur à atteindre des formes plus performantes.
Lorsque les équations de fluide visqueux (RANS[5]) sont résolues, on constate que les trois formes proposées pour la combinaison convexe ne permettent pas d'aboutir à un résultat d'optimisation satisfaisant. Par conséquent, une quatrième forme est ajoutée à la base de données, grâce à laquelle l'optimiseur est capable d'améliorer la performance de la forme finale. Ce cas démontre la possibilité d'enrichissement de la combinaison convexe ; il est possible de rajouter des formes à la base de données afin d'augmenter le nombre de degrés de liberté, et potentiellement d'améliorer les résultats d'optimisation.

Pour préparer les optimisations sur un cas de complexité industrielle, un modèle CAO de nacelle de moteur turbofan double-flux a été développé, qui comprend les bifurcations internes et le pylône. Ce modèle CATIA[6] est paramétré grâce à plusieurs

[5]Reynolds Averaged Navier-Stokes
[6]propriété de Dassault Systèmes

centaines de paramètres de dessin, et permet des modifications 3D (non-axisymétriques) de la géométrie. De plus, il intègre des contraintes industrielles, notamment sur les sections de passage des tuyères, afin de respecter les caractéristiques du cycle thermodynamique du moteur.
A partir des formes générées par CAO, un processus de maillage a été défini et enregistré à l'aide d'ICEM CFD[7], afin de pouvoir être « rejoué » lorsque la géométrie de nacelle est modifiée. Ce maillage, défini selon les standards industriels, comprend 15.10^6 cellules, et représente un compromis entre précision et temps de calcul pour les simulations CFD.
Pour permettre l'utilisation des outils géométriques au sein d'un processus d'optimisation, les étapes de génération de la CAO et du maillage ont été automatisées. De plus, la robustesse de l'ensemble vis-à-vis de la méthode de combinaison convexe a été testée et améliorée en effectuant un plan d'expériences sur un espace généré par trois formes « expert » de nacelle.

Grâce aux approches développées précédemment, un cas de nacelle UHBR[8] basé sur le modèle CAO a été étudié et optimisé. Pour ce premier travail d'optimisation, le choix est fait de ne considérer que la nacelle isolée (sans l'avion ou la voilure). L'objectif est alors de maximiser la résultante des efforts sur la nacelle, pour des conditions motrices fixées. Dans ce cas, la chaîne d'optimisation comprend la CAO, des simulations RANS avec elsA[9], ainsi qu'un post-traitement dédié permettant de détailler les contributions des efforts sur l'installation motrice. La combinaison convexe est utilisée avec un base de données composée de trois formes, et permet de trouver un premier optimum sur un premier sous-espace de design. L'interprétation des coefficients de combinaison montre néanmoins que la forme optimale laisse complètement de côté l'une des trois formes « expert ». Ainsi, une seconde optimisation est effectuée en remplaçant la forme non-utilisée par une nouvelle forme, et mène à une seconde configuration optimale distincte, reposant sur des mécanismes de gains de performance aérodynamique différents. Pour conclure cette étude, un plan d'expérience est mené sur l'espace généré par combinaison convexe (avec la seconde base de données), afin d'améliorer la compréhension des deux résultats d'optimisation. Ce travail valide l'utilisation de l'approche par combinaison convexe pour mener des optimisations aérodynamiques de formes définies par CAO.

Suite à l'optimisation d'une nacelle en configuration isolée, les premières étapes du développement de calculs couplés aéro-propulsifs ont été menées. Ces calculs, couplant un modèle thermodynamique avec la simulation CFD, sont un outil nécessaire pour la mise en place d'un cas de nacelle installée sous voilure. En effet, ils permettent de considérer l'interdépendance existant entre l'aérodynamique des tuyères et la thermodynamique du moteur, et d'évaluer le performance de l'installation motrice à l'équilibre poussée / traînée. Une stratégie a été proposée et plusieurs méthodes d'implémentation ont été comparées pour mener le couplage aéropropulsif. Puis, des premières simulations couplées ont pu être effectuées en opérant le couplage « à la main ». Ces travaux, appliqués notamment à une forme optimisée précédemment, ont ainsi démontré l'intérêt du couplage et la nécessité de considérer des simulations

[7] propriété de ANSYS
[8] Ultra High ByPass Ratio
[9] propriété d'Airbus, Safran et l'ONERA

aéropropulsives pour l'optimisation de formes de tuyères.

Conclusions et perspectives

En conclusion, ce travail de thèse a consisté à développer une approche visant à mener des optimisations de formes de tuyères pour des moteurs de type turbofan en configuration installée. Pour pouvoir répondre aux contraintes industrielles de ce sujet, et permettre notamment l'utilisation d'un logiciel CAO au sein du processus d'optimisation, une méthode originale appelée *combinaison convexe* a été introduite puis testée sur des cas de complexité croissante. En raison des nombreux développements effectués autour de l'approche d'optimisation, l'objectif final du projet de thèse, à savoir l'optimisation de tuyères sous voilure, n'a pas pu être mené au cours de ce travail. Néanmoins, les sujets traités dans cette thèse permettront la mise en oeuvre de ces optimisations dans un futur proche.

La suite de ces travaux consistera tout d'abord à continuer la mise en place de simulations aéro-propulsives. Grâce à un couplage automatisé et « embarqué » dans la CFD, de telles simulations pourront être utilisées au cours de processus d'optimisation. En particulier, ces optimisations avec couplage aéro-propulsif pourront être appliquées aux tuyères, et comparées aux travaux à conditions motrices fixées.
Ensuite, des simulations de nacelles installées sous voilure pourront être mises en places. Grâce à cela, le développement d'un processus d'optimisation dédié aux tuyères en configuration installée sera possible.
Enfin, des méthodes d'optimisation alternatives à celles qui ont été utilisées au cours de ces travaux peuvent être envisagées. Pour commencer, il semblerait qu'une approche d'optimisation multi-objectifs serait plus adaptée aux problématiques de conception des tuyères. Puis il serait intéressant d'évaluer des méthodes de type SBO en association avec la combinaison convexe. Elles pourraient permettre une réduction du nombre d'évaluations, en augmentant la probabilité d'obtenir l'optimum global du sous-espace. Il serait également envisageable de définir un processus d'optimisation à plusieurs niveaux. Dans ce cas, la combinaison convexe jouerait le rôle d'une première étape de recherche « exploratoire ». Elle serait suivie d'une seconde optimisation, dont le but serait de raffiner le résultat et de chercher les derniers points de performance à l'aide d'un algorithme d'optimisation du premier ordre, utilisant des gradients calculés par adjoint.

Bibliography

[1] B. M. Adams, W. Bohnhoff, K. Dalbey, J. Eddy, M. Eldred, D. Gay, K. Haskell, P. D. Hough, and L. P. Swiler. Dakota, a multilevel parallel object-oriented framework for design optimization, parameter estimation, uncertainty quantification, and sensitivity analysis: version 5.0 user's manual. *Sandia National Laboratories, Tech. Rep. SAND2010-2183*, 2009. 52, 58, 89, 139

[2] M. Albert and D. Bestle. Aerodynamic design optimization of nacelle and intake. 06 2013. 25, 33

[3] E. Andrés-Pérez, D. González-Juarez, M. Martin, E. Iuliano, D. Cinquegrana, G. Carrier, J. Peter, D. Bailly, O. Amoignon, P. Dvorak, D. Funes, P. Weinerfelt, L. Carro, S. Salcedo, Y. Jin, J. Doherty, and H. Wang. Garteur ad/ag-52: Surrogate-based global optimization methods in preliminary aerodynamic design. In *Evolutionary and Deterministic Methods for Design Optimization and Control With Applications to Industrial and Societal Problems*, pages 195–210. Springer International Publishing, 2019. 34

[4] ANSYS. Icem, 2015. 75

[5] M. Banović, O. Mykhaskiv, S. Auriemma, A. Walther, H. Legrand, and J. D. Müller. Algorithmic differentiation of the Open CASCADE Technology CAD kernel and its coupling with an adjoint CFD solver. *Optimization Methods and Software*, 33(4-6):813–828, 2018. 35

[6] R. Bell and R. Cedar. An inverse method for the aerodynamic design of three-dimensional aircraft engine nacelles. 1991. 24

[7] C. Benoit, S. Peron, and S. Landier. Cassiopee: a cfd pre- and post-processing tool. *Aerospace Science and Technology*, 45:272–283, 2015. 89

[8] H.-G. Beyer and H.-P. Schwefel. Evolution strategies–a comprehensive introduction. *Natural computing*, 1(1):3–52, 2002. 33

[9] C. G. Broyden. The convergence of a class of double-rank minimization algorithms. *IMA Journal of Applied Mathematics*, 6(1):76–90, 1970. 33

[10] L. Cambier, S. Heib, and S. Plot. The ONERA elsA CFD software: input from research and feedback from industry. *Mechanics & Industry*, 14(3):159–174, 2013. 53, 89

[11] S. Candel. *Mécanique des fluides*. Dunod, 1990. 19, 20, 38, 51

[12] G. Carrier, D. Destarac, A. Dumont, M. Méheut, I. Salah El Din, J. Peter, S. Khelil, J. Brezillon, and M. Pestana. Gradient-based aerodynamic optimization with the elsA software. 2014. 32

[13] J. F. Dannenhoffer and R. Haimes. Design sensitivity calculations directly on CAD-based geometry. In *53rd AIAA Aerospace Aerospace Sciences Meeting*, 2015. 35

[14] Dassault Systèmes. Catia v5, 1998. 74

[15] D. Destarac and J. Reneaux. Transport aircraft aerodynamic improvement by numerical optimization. In *ICAS Congress, Septembre*, pages 9–14, 1990. 24

[16] D. Dusa, D. Lahti, and D. Berry. Investigation of subsonic nacelle performance improvement concept. In *18th Joint Propulsion Conference*, page 1042, 1982. 24

[17] Empresarios Agrupados. Proosis, 2012. 85

[18] R. Fletcher. A new approach to variable metric algorithms. *The Computer Journal*, 13(3):317–322, 1970. 33

[19] A. I. Forrester and A. J. Keane. Recent advances in surrogate-based optimization. *Progress in aerospace sciences*, 45(1-3):50–79, 2009. 34

[20] K. Giannakoglou. Design of optimal aerodynamic shapes using stochastic optimization methods and computational intelligence. *Progress in Aerospace Sciences*, 38(1):43–76, 2002. 33

[21] Y. Gisin and D. Marshall. Wing-nacelle assembly multidisciplinary performance optimization. In *45th AIAA Aerospace Sciences Meeting and Exhibit*, page 1463, 2007. 24

[22] D. Goldfarb. A family of variable-metric methods derived by variational means. *Mathematics of Computation*, 24(109):23–26, 1970. 33

[23] I. Goulos, D. MacManus, and C. Sheaf. Civil turbofan engine exhaust aerodynamics: Impact of fan exit flow characteristics. *Aerospace Science and Technology*, 93:105181, 2019. 26, 34

[24] I. Goulos, J. Otter, T. Stankowski, D. MacManus, N. Grech, and C. Sheaf. Aerodynamic Design of Separate-Jet Exhausts for Future Civil Aero-engines—Part II: Design Space Exploration, Surrogate Modeling, and Optimization. *Journal of Engineering for Gas Turbines and Power*, 138(8), 03 2016. 25, 34

[25] I. Goulos, J. Otter, T. Stankowski, D. Macmanus, N. Grech, and C. Sheaf. Design optimisation of separate-jet exhausts for the next generation of civil aero-engines. *The Aeronautical Journal*, 122(1256):1586–1605, 2018. 12, 25, 26, 34, 138

[26] I. Goulos, T. Stankowski, D. MacManus, P. Woodrow, and C. Sheaf. Civil turbofan engine exhaust aerodynamics: Impact of bypass nozzle after-body design. *Aerospace Science and Technology*, 73:85–95, 2018. 26, 34

[27] I. Goulos, T. Stankowski, J. Otter, D. MacManus, N. Grech, and C. Sheaf. Aerodynamic Design of Separate-Jet Exhausts for Future Civil Aero-engines—Part I: Parametric Geometry Definition and Computational Fluid Dynamics Approach. *Journal of Engineering for Gas Turbines and Power*, 138(8), 03 2016. 25

[28] J. Gray, J. Chin, T. Hearn, E. Hendricks, T. Lavelle, and J. R. Martins. Chemical-equilibrium analysis with adjoint derivatives for propulsion cycle analysis. *Journal of Propulsion and Power*, 33(5):1041–1052, 2017. 26

[29] J. S. Gray, G. K. Kenway, C. A. Mader, and J. Martins. Aero-propulsive design optimization of a turboelectric boundary layer ingestion propulsion system. In *2018 Aviation Technology, Integration, and Operations Conference*. 12, 26, 27, 138

[30] J. S. Gray, C. A. Mader, G. K. Kenway, and J. R. Martins. Modeling boundary layer ingestion using a coupled aeropropulsive analysis. *Journal of Aircraft*, pages 1–9, 2017. 26

[31] C. Heath, J. Seidel, and S. K. Rallabhandi. Viscous aerodynamic shape optimization with installed propulsion effects. In *35th AIAA Applied Aerodynamics Conference*, page 3046, 2017. 26

[32] H. Hoheisel. Aerodynamic aspects of engine-aircraft integration of transport aircraft. *Aerospace science and technology*, 1(7):475–487, 1997. 24

[33] J. H. Holland et al. *Adaptation in natural and artificial systems: an introductory analysis with applications to biology, control, and artificial intelligence*. MIT press, 1992. 33

[34] E. Iuliano. Global optimization of benchmark aerodynamic cases using physics-based surrogate models. *Aerospace Science and Technology*, 67:273 – 286, 2017. 34

[35] A. Jameson. Aerodynamic design via control theory. *Journal of Scientific Computing*, 3:233–260, 1988. 32

[36] B. D. Keith, K. Uenishi, and D. A. Dietrich. Cfd-based three-dimensional turbofan exhaust nozzle analysis system. *Journal of Propulsion and Power*, 9(6):840–846, 1993. 21

[37] J. Kennedy and R. Eberhart. Particle swarm optimization. In *Proceedings of ICNN'95-International Conference on Neural Networks*, volume 4, pages 1942–1948. IEEE, 1995. 33

[38] S. Koc, H. J. Kim, and K. Nakahashi. Aerodynamic design of wing-body-nacelle-pylon configuration. In *17th AIAA Computational Fluid Dynamics Conference*, page 4856, 2005. 24

[39] T. Kumano, S. Jeong, S. Obayashi, Y. Ito, K. Hatanaka, and H. Morino. Multidisciplinary design optimization of wing shape with nacelle and pylon. In *ECCOMAS CFD 2006: Proceedings of the European Conference on Computational Fluid Dynamics, Egmond aan Zee, The Netherlands, September 5-8, 2006*. Delft University of Technology; European Community on Computational Methods in Applied Sciences (ECCOMAS), 2006. 24

[40] P.-A. Lambert. *Optimisation de formes en aérodynamique: application à la conception des nacelles de moteurs civils*. PhD thesis, Ecole Centrale Paris, 1995. 25, 32

[41] P. A. Lambert, J. L. Lecordix, and V. Braibant. Constrained optimization of nacelle shapes in euler flow using semianalytical sensitivity analysis. *Structural optimization*, 10:239–246, 1995. 25, 32

[42] R. B. Langtry, M. Kuntz, and F. R. Menter. The aerodynamic effects of vhbr engine installation to the common research model. *Journal of Aircraft*, 2005. 24

[43] S. T. LeDoux, J. C. Vassberg, D. P. Young, S. Fugal, D. Kamenetskiy, W. P. Huffman, R. G. Melvin, and M. F. Smith. Study based on the aiaa aerodynamic design optimization discussion group test cases. *AIAA Journal*, 53(7):1910–1935, 2015. 24

[44] E. E. Lee Jr and O. C. Pendergraft Jr. Installation effects of long-duct pylon-mounted nacelles on a twin-jet transport model with swept supercritical wing. *NASA Technical Paper*, 1985. 24

[45] W. Lin, A. Chen, and E. Tinoco. 3D transonic nacelle and winglet design. In *Flight Simulation Technologies Conference and Exhibit*, 1990. 24

[46] J. L. Lions. *Optimal Control of Systems Governed by Partial Differential Equations*. Springer-Verlag Berlin Heidelberg, 1971. 32

[47] M. Meheut, A. Arntz, and G. Carrier. Aerodynamic shape optimizations of a blended wing body configuration for several wing planforms. In *30th AIAA Applied Aerodynamics Conference*, page 3122, 2012. 32, 53

[48] A. Merle, A. Stueck, and A. Rempke. An adjoint-based aerodynamic shape optimization strategy for trimmed aircraft with active engines. In *35th AIAA Applied Aerodynamics Conference*, 2017. 24

[49] M. Mitchell. *An introduction to genetic algorithms*. MIT press, 1998. 33

[50] F. Moens and J. Dandois. Optimization of passive flow control devices of a slatless high-lift configuration. *Journal of Aircraft*, 53(1):189–201, 2016. 33

[51] F. Moens and C. Wervaecke. Multi-point optimization of shapes and settings of high-lift system by means of evolutionary algorithm and navier-stokes equations. *Engineering Computations*, 2013. 33

[52] B. Mohammadi and O. Pironneau. Shape optimization in fluid mechanics. *Annual Review of Fluid Mechanics*, 36(1):255–279, 2004. 30

[53] B. Mohammadi and O. Pironneau. *Applied shape optimization for fluids*. Oxford university press, 2010. 30

[54] S. Mouton, J. Laurenceau, and G. Carrier. Aerodynamic and structural optimization of powerplant integration under the wing of a transonic transport aircraft. In *Proceedings of 42th AAAF Symposium on Applied Aerodynamics, Nice*, 2007. 24

[55] L. Mueller and T. Verstraete. CAD integrated multipoint adjoint-based optimization of a turbocharger radial turbine. *International Journal of Turbomachinery, Propulsion and Power*, 2(3):14, 2017. 32, 35

[56] M. Méheut, D. Destarac, S. Ben Khelil, G. Carrier, A. Dumont, and J. Peter. Gradient-based single and multi-points aerodynamic optimizations with the elsA software. In *53rd AIAA Aerospace Sciences Meeting*, 2015. 24, 32

[57] M. Méheut, A. Dumont, G. Carrier, and J. Peter. Gradient-based optimization of crm wing-alone and wing-body-tail configurations by rans adjoint technique. In *54th AIAA Aerospace Sciences Meeting*, 2016. 24, 32

[58] M. Méheut, A. Dumont, G. Engel, D. Destarac, D. Baumgärtner, and K.-U. Bletzinger. Aerodynamic shape optimization progress on ADODG benchmark problems using the elsA software. In *35th AIAA Applied Aerodynamics Conference*, 2017. 24, 32

[59] O. Pironneau. *Optimal Shape Design for Elliptic Systems*. Springer-Verlag Berlin Heidelberg, 1984. 32

[60] N. V. Queipo, R. T. Haftka, W. Shyy, T. Goel, R. Vaidyanathan, and P. K. Tucker. Surrogate-based analysis and optimization. *Progress in aerospace sciences*, 41(1):1–28, 2005. 34

[61] L. A. Rastrigin. *Systems of extremal control.* 1974. 31

[62] I. Rechenberg. Evolution strategy: Nature's way of optimization. In H. W. Bergmann, editor, *Optimization: Methods and Applications, Possibilities and Limitations*, pages 106–126. Springer Berlin Heidelberg, 1989. 33

[63] J. Reuther, J. Alonso, M. Rimlinger, and A. Jameson. Aerodynamic shape optimization of supersonic aircraft configurations via an adjoint formulation on distributed memory parallel computers. *Computers & Fluids*, 28(4):675 – 700, 1999. 32

[64] T. T. Robinson, C. G. Armstrong, H. S. Chua, C. Othmer, and T. Grahs. Sensitivity-based optimization of parameterized CAD geometries. In *8th World Congress on Structural and Multidisciplinary Optimization*, 2009. 35

[65] T. T. Robinson, C. G. Armstrong, H. S. Chua, C. Othmer, and T. Grahs. Optimizing parameterized CAD geometries using sensitivities based on adjoint functions. *Computer-Aided Design and Applications*, 9(3):253–268, 2012. 35

[66] C.-C. Rossow, J.-L. Godard, H. Hoheisel, and V. Schmitt. Investigations of propulsion integration interference effects on a transport aircraft configuration. *Journal of Aircraft*, 31(5):1022–1030, 1994. 24, 46, 47

[67] R. Rudnik, C.-C. Rossow, and H. F. v. Geyr. Numerical simulation of engine/airframe integration for high-bypass engines. *Aerospace Science and Technology*, 6(1):31–42, 2002. 24

[68] I. Sanchez Torreguitart, T. Verstraete, and L. Mueller. Optimization of the ls89 axial turbine profile using a CAD and adjoint based approach. *International Journal of Turbomachinery, Propulsion and Power*, 3(3):20, 2018. 32

[69] J. Santiago, M. Claeys-Bruno, and M. Sergent. Construction of space-filling designs using WSP algorithm for high dimensional spaces. *Chemometrics and Intelligent Laboratory Systems*, 113:26–31, 2012. 62

[70] D. Sasaki and K. Nakahashi. Aerodynamic optimization of an over-the-wing-nacelle-mount configuration. *Modelling and Simulation in Engineering*, 2011:11, 2011. 24

[71] D. F. Shanno. Conditioning of quasi-newton methods for function minimization. *Mathematics of Computation*, 24(111):647–656, 1970. 33

[72] S. Skinner and H. Zare-Behtash. State-of-the-art in aerodynamic shape optimisation methods. *Applied Soft Computing*, 62:933–962, 2018. 30

[73] S. Smith, M. Nemec, and S. Krist. Integrated nacelle-wing shape optimization for an ultra-high bypass fanjet installation on a single-aisle transport configuration. In *51st AIAA Aerospace Sciences Meeting including the New Horizons Forum and Aerospace Exposition*, page 543, 2013. 24

[74] W. Song and A. J. Keane. Surrogate-based aerodynamic shape optimization of a civil aircraft engine nacelle. *AIAA journal*, 45(10):2565–2574, 2007. 25, 34

[75] T. Stankowski, D. MacManus, and M. Robinson. The aerodynamic effects of vhbr engine installation to the common research model. *Journal of Aircraft*, 2017. 11, 24, 26

[76] T. P. Stańkowski, D. G. MacManus, C. T. Sheaf, and R. Christie. Aerodynamics of aero-engine installation. *Proceedings of the Institution of Mechanical Engineers, Part G: Journal of Aerospace Engineering*, 230(14):2673–2692, 2016. 24

[77] M. L. Stein. *Interpolation of spatial data: some theory for kriging*. Springer Science & Business Media, 2012. 34, 64

[78] L. Sun, W. Yao, T. Robinson, S. Marques, and C. Armstrong. A framework of gradient-based shape optimization using feature-based CAD parameterization. In *AIAA Scitech 2020 Forum*. 35

[79] F. Tejero, I. Goulos, D. MacManus, and C. Sheaf. Effects of aircraft integration on compact nacelle aerodynamics. In *AIAA Scitech 2020 Forum*. 24, 34

[80] F. Tejero, D. MacManus, and C. Sheaf. Impact of droop and scarf on the aerodynamic performance of compact aero-engine nacelles. In *AIAA Scitech 2020 Forum*. 25

[81] F. Tejero, D. G. MacManus, and C. Sheaf. Surrogate-based aerodynamic optimisation of compact nacelle aero-engines. *Aerospace Science and Technology*, 93:105207, 2019. 25, 34

[82] H. Toubin, I. Salah El Din, and M. Meheut. Multipoint aerodynamic high fidelity shape optimization of an isolated engine nacelle. In *52nd AIAA Aerospace Sciences Meeting, AIAA SciTech*, 2014. 25, 32, 46, 53

[83] P. J. Van Laarhoven and E. H. Aarts. *Simulated annealing: Theory and applications*. Springer, 1987. 34

[84] G. N. Vanderplaats. *Numerical optimization techniques for engineering design: with applications*. McGraw-Hill, 1984. 34

[85] Vanderplaats Research and Development. DOT users manual, version 4.20. 1995. 52, 89

[86] T. Verstraete. Introduction to optimization and multidisciplinary design, September 2018. 30

[87] T. Verstraete, L. Müller, and J.-D. Müller. Adjoint-based design optimisation of an internal cooling channel u-bend for minimised pressure losses. *International Journal of Turbomachinery, Propulsion and Power*, 2(2):10, 2017. 32, 35

[88] C. Wervaecke. Technical report: Hybrid stochastic gradient-based method for aerodynamic shape optimization, 2012. 35

[89] L. Wiart, O. Atinault, R. Grenon, B. Paluch, and D. Hue. Development of NOVA aircraft configurations for large engine integration studies. In *33rd AIAA Applied Aerodynamics Conference*, page 2254, 2015. 84, 85

[90] R. Wilhelm. Inverse design method for designing isolated and wing-mounted engine nacelles. *Journal of Aircraft*, 39(6):989–995, 2002. 24, 25

[91] R. Wilhelm. An inverse design method for engine nacelles and wings. *Aerospace Science and Technology*, 9(1):19–29, 2005. 24, 25

[92] S. Xu, W. Jahn, and J.-D. Müller. CAD-based shape optimisation with CFD using a discrete adjoint. *International Journal for Numerical Methods in Fluids*, 74(3):153–168. 35

[93] G. Yu, J.-D. Müller, D. Jones, and F. Christakopoulos. CAD-based shape optimisation using adjoint sensitivities. *Computers & Fluids*, 46(1):512 – 516, 2011. 10th ICFD Conference Series on Numerical Methods for Fluid Dynamics (ICFD 2010). 35

CONCEPTION ET OPTIMISATION DE TUYERES EN CONFIGURATION INSTALLEE

Lorsque les moteurs aéronautiques sont installés sous les ailes des aéronefs, des interactions aérodynamiques apparaissent entre l'ensemble propulsif et la voilure, qui sont aussi appelées « effets d'installation ». L'augmentation du taux de dilution des turbofan, permettant de réduire leur consommation de carburant, conduit à des diamètres de nacelles plus importants qu'auparavant, et renforce ces phénomènes. En particulier, l'arrière-corps et les tuyères du moteur sont situés à proximité de l'intrados de la voilure et sont fortement impactés par ces interactions aérodynamiques. Afin de mieux prendre en compte les effets d'installation dès les phases préliminaires de conception, cette thèse vise à développer des méthodes pour le dessin des lignes aérodynamiques de tuyères basées sur des optimisations de formes, s'appuyant sur des outils de dessin industriel (CAO) et des simulations aéro-propulsives couplées. Les modèles géométriques industriels utilisent généralement des logiciels commerciaux de CAO, et comprennent des centaines de paramètres de dessin. Cependant, une étude bibliographique montre que les méthodes d'optimisation existantes ne permettent pas de traiter des cas avec un grand nombre de variables tout en incluant des logiciels commerciaux en « boîte noire ». En réponse à cette difficulté, une méthode originale, appelée *combinaison convexe*, est proposée et développée dans ce travail. En se servant du savoir-faire industriel pour définir un sous-espace de l'espace de conception, cette approche innovante permet de réduire la dimension du problème d'optimisation. Ainsi, elle donne accès à la plupart des méthodes d'optimisation pour la recherche d'un optimum sur l'espace réduit. Tout d'abord, cette approche a été appliquée à une nacelle de moteur mono-flux et bidimensionnelle. Sur ce cas simple, sans CAO, la méthode a été testée et validée. De surcroît, explorer l'espace réduit s'est avéré être une stratégie parfois plus performante que l'exploration du domaine de design complet. Puis, un cas de nacelle double-flux de complexité industrielle a été mis en œuvre, avec des géométries CAO. Les optimisations opérées sur cette nacelle isolée (sans présence de l'avion) ont permis de démontrer le bon fonctionnement de la méthode avec des outils industriels de conception. Pour finir, des travaux ont été menés pour développer des calculs aérodynamiques comprenant un couplage avec un modèle thermodynamique de moteur, aussi appelés simulations couplées aéro-propulsives. A terme, de tels calculs pourront être intégrés au sein de la chaîne d'optimisation. Les travaux de thèse ont donc consisté à mettre en place un processus d'optimisation aérodynamique adapté pour le dessin de tuyères de moteurs aéronautiques, tout en prenant en compte les outils de conception et des cas d'application industriels. Bien que l'application à une configuration motrice installée avec couplage aéro-propulsif n'ait pas été effectuée dans le cadre de cette thèse, l'approche développée permettra sa mise en œuvre industrielle dans un futur proche.

Mots-clés : Optimisation, Aérodynamique, Conception Assistée par Ordinateur (CAO)

DESIGN AND OPTIMIZATION OF AIRCRAFT ENGINE NOZZLES IN UNDER-WING CONFIGURATION

When aircraft have under-wing propulsion systems, aerodynamic interactions appear between engines and wings. The trend of increasing turbofans by-pass ratio in order to improve their efficiency leads to greater engine diameters, and therefore strengthens these installation effects. In particular, the engine rear-body and the nozzles are located in the vicinity of the wing pressure side and are directly concerned by these interactions. In order to take these effects into account during early design phases of nozzles aerolines, the present thesis work aims at developing design approaches based on aerodynamic shape optimization methods, with industrial tools (such as CAD) and coupled aeropropulsive simulations. Industrial geometrical models are usually defined with commercial CAD software and comprise hundreds of design parameters. However, a literature review on optimization methods shows the difficulty of considering these software as well as a high number of design variables. Consequently, an original approach called *convex combination* is proposed. This method enables a dimensional reduction for the optimization problem, by using industrial know-how to define a subspace of the design space. Thus, it allows the use of most optimization methods for optimum research on the subspace. At first, this approach is tested and validated on a 2D single-flow nozzle case. On this case without CAD, exploring a subspace appears capable of outperforming full-space research. Then, a case of industrial complexity is defined, with a CAD geometry of turbofan nacelle and dual separate flow nozzles. Optimizations performed on this isolated nacelle (without aircraft) validate the use of the proposed approach with industrial design tools. Finally, some developments towards fully-coupled aeropropulsive simulations are made. In the end, these simulations coupling aerodynamics to a thermodynamic engine model are expected to be integrated in the optimization workflow. The thesis work consisted in developing optimization strategies and workflows adapted to the design of aeronautic turbofan nozzles, while considering industrial use cases and tools. Although the final application case on a complete aircraft with under-wing engines has not been covered in this work, the proposed *convex combination* approach and the associated workflow will allow to carry out this study in the near future.

Keywords: Optimization, Aerodynamics, Computer-Assisted Design (CAD)